

©Copyright 2023

Mengyuan Wang

Optimal Control for Electrically Propelled Aircraft  
and Urban Air Mobility Network

Mengyuan Wang

A dissertation  
submitted in partial fulfillment of the  
requirements for the degree of

Doctor of Philosophy

University of Washington

2023

Reading Committee:

Mehran Mesbahi, Chair

Lillian Ratliff

Amirhossein Taghvaei

Program Authorized to Offer Degree:  
William E. Boeing Department of Aeronautics & Astronautics

University of Washington

## Abstract

Optimal Control for Electrically Propelled Aircraft  
and Urban Air Mobility Network

Mengyuan Wang

Chair of the Supervisory Committee:  
Professor Mehran Mesbahi  
William E. Boeing Department of Aeronautics & Astronautics

This dissertation aims to address fundamental challenges in the field of Urban Air Mobility (UAM) through optimal control strategies. Three key aspects are studied to enhance the performance of UAM. First, a trajectory optimization algorithm for All-Electric Aircraft (AEA) is proposed, along with the corresponding Simulink models, to minimize the operating cost of AEA. The impact of battery dynamics on optimal trajectories is explored by integrating several battery models with distinct fidelity into the corresponding optimal control problems. Second, an energy management system is designed for Hybrid-Electric Aircraft (HEA) to optimize fuel consumption. Numerical results for two HEA models indicate the limited fuel-saving achieved by using the engine to charge the battery during flight. This observation leads to the investigation of two parallel hybrid electric configurations, aiming to answer the question of whether it is worthwhile to charge the battery during flight at all. A finite-dimensional optimization problem is formulated, and numerical results indicate that increasing onboard battery capacity is more fuel-efficient than in-flight charging. Finally, two important topics related to the UAM are investigated: optimal vertiport selection problem and task assignment and vehicle routing problem. For the vertiport selection problem, a mixed-integer programming approach is developed and applied to a hybrid ground-air network to improve the traffic performance. As for the task assignment problem, a centralized approach is adopted to assign a sequence of tasks to each vehicle, maximizing the overall profit. The problem is transformed into an identification of multiple paths in a task network and is solved using a greedy algorithm.

## **DEDICATION**

To my dearest husband Yiren Shen and our beloved little pi.

## TABLE OF CONTENTS

	Page
List of Figures . . . . .	iv
List of Tables . . . . .	vii
Chapter 1: <b>Introduction</b> . . . . .	1
1.1 Statement of contributions . . . . .	3
1.2 Outline of dissertation . . . . .	5
Chapter 2: <b>Preliminaries</b> . . . . .	6
2.1 Aircraft models . . . . .	6
2.1.1 Eviation Alice . . . . .	7
2.1.2 SOUL . . . . .	7
2.1.3 Conceptual HEA model . . . . .	8
2.2 Dynamics . . . . .	12
2.2.1 Flight dynamics . . . . .	12
2.2.2 Battery dynamics . . . . .	13
2.3 Optimal control methods . . . . .	16
2.3.1 The minimum principle . . . . .	17
2.3.2 Singular optimal control problem . . . . .	19
Chapter 3: Trajectory optimization for All-Electric Aircraft . . . . .	20
3.1 Related works . . . . .	21
3.2 Problem formulation . . . . .	23
3.2.1 Objective functions . . . . .	23
3.2.2 Battery dynamics and Simplified flight dynamics . . . . .	24
3.2.3 Optimal control problems . . . . .	26
3.3 Optimal necessary conditions analyses . . . . .	29
3.3.1 Constant altitude cruise phase . . . . .	29
3.3.2 Accelerated climb phase . . . . .	31

3.4	Numerical results . . . . .	32
3.4.1	Constant altitude cruise phase with the ideal battery model . . . . .	32
3.4.2	Constant altitude cruise phase with ECM . . . . .	35
3.4.3	Accelerated climb phase with ideal battery model . . . . .	39
3.4.4	A complete flight phase . . . . .	42
3.5	Simulink model with different battery blocks . . . . .	47
Chapter 4: Power allocation and structures study for Hybrid-Electric Aircraft . . . . .		51
4.1	Related works . . . . .	53
4.2	Power allocation algorithm for HEA . . . . .	55
4.2.1	Power relation in the propulsion system . . . . .	56
4.2.2	States dynamics and operating modes analysis . . . . .	58
4.2.3	Fuel minimization problem . . . . .	60
4.2.4	Numerical results . . . . .	63
4.3	Comparison of two parallel hybrid electric configurations . . . . .	72
4.3.1	Parallel hybrid electric architectures . . . . .	72
4.3.2	Power allocation problem transformation . . . . .	74
4.3.3	Comparison of two parallel configurations . . . . .	80
Chapter 5: Vertiport selection and task assignment for UAM . . . . .		88
5.1	Related works for vertiport selection and traffic equilibria . . . . .	89
5.1.1	Related work . . . . .	89
5.1.2	Hybrid ground-air transportation networks formulation . . . . .	90
5.1.3	Traffic equilibria with node and link capacities . . . . .	95
5.2	Groud-Air hybrid transportation network design . . . . .	97
5.2.1	Mixed-integer linear programming . . . . .	98
5.2.2	Numerical results . . . . .	104
5.3	Related works for task assignment problem . . . . .	106
5.4	Task assignment and vehicle routing for UAM . . . . .	108
5.4.1	Task network formulation . . . . .	108
5.4.2	Mixed integer programming . . . . .	111
5.4.3	Greedy algorithm and sub-modular proof . . . . .	116
5.4.4	Numerical results . . . . .	120
Chapter 6: Conclusions . . . . .		123

Bibliography . . . . .	127
Appendix A: HEA optimization problem transformation . . . . .	140
A.1 Transformation to a finite-dimensional optimization problem . . . . .	140
A.2 Verification of the second-order sufficient condition and sensitivity analysis . . . . .	142
Appendix B: Vertiport selection proof . . . . .	144
B.1 Proof of Proposition 1 . . . . .	144
B.2 Proof of Corollary 1 . . . . .	145
B.3 Proof of Proposition 2 . . . . .	145

## LIST OF FIGURES

Figure Number		Page
1.1	Research topics explored in this dissertation. . . . .	3
2.1	Eviaition Alice. . . . .	8
2.2	Ultralight aircraft SONG. . . . .	10
2.3	Fuel consumption characteristics of the engine: (a) SFC vs output power; (b) fuel flow rate vs output power. . . . .	10
2.4	Open circuit potential of a single battery cell. . . . .	14
2.5	Single Particle Model illustration. . . . .	16
3.1	The numerical results of states with ideal battery model. . . . .	33
3.2	The numerical results of control input and corresponding drag force with ideal battery model. . . . .	34
3.3	The numerical results of optimal states with ECM. . . . .	35
3.4	The numerical results of optimal control input and corresponding drag force with ECM. .	36
3.5	The numerical results of battery states with ECM. . . . .	37
3.6	The impact of initial velocity on the total cost and terminal time. . . . .	37
3.7	Climb phase; (a)Horizontal distance profile; (b)Velocity (only magnitude) profile. . .	39
3.8	Climb phase; (a) Altitude profile; (b) Flight path angle profile. . . . .	40
3.9	Climb phase; (a) SOC of the battery pack profile; (b) The current passing through the battery pack. . . . .	40
3.10	Climb phase; (a) Thrust force profile; (b) Lift coefficient profile. . . . .	41
3.11	Climb phase with an extra constraint; (a) Thrust force profile; (b) Current profile. .	42
3.12	A complete flight phase; (a) Horizontal distance; (b) Velocity (magnitude). . . . .	45
3.13	A complete flight phase; (a) Altitude; (b) Flight path angle. . . . .	46
3.14	A complete flight phase; (a) State of charge; (b) Current. . . . .	46
3.15	A complete flight phase; (a) Thrust; (b) Lift coefficient. . . . .	47
3.16	AEA Simulink Model. . . . .	48
3.17	Comparisons of voltage and cell current for distinct battery models. . . . .	50
4.1	Fuel consumption rate at different output power. . . . .	58

4.2	Case 1–control input and states: (a) the throttle of the engine, (b) the total mass, (c) the SOC of the battery pack. . . . .	65
4.3	Case 1–power allocation and fuel consumption rate: (a) engine output power, (b) battery output power, (c) the corresponding fuel rate (kg/h) under control. . . . .	65
4.4	Case 1 (Not charging the battery pack during flight)–control input and states: (a) the throttle of the engine, (b) the total mass, (c) the SOC of the battery pack. . . . .	66
4.5	Case 1 (Not charging the battery pack during flight)–power allocation and fuel consumption rate: (a) engine output power, (b) battery output power, (c) the corresponding fuel rate (kg/h) under control. . . . .	66
4.6	The time history profiles of control input for the first three cases. . . . .	67
4.7	The time history profiles of SOC for the first three cases. . . . .	67
4.8	The time history profiles of fuel rate for the first three cases. . . . .	68
4.9	The time history profiles for case 3. . . . .	68
4.10	The time history profiles for case 4. . . . .	69
4.11	Climb phase control input and states: (a) the throttle of the engine, (b) the total mass, (c) the SOC of the battery pack. . . . .	70
4.12	Climb phase power allocation and fuel consumption rate: (a) engine output power, (b) battery output power, (c) the corresponding fuel rate (kg/h) under control. . . . .	70
4.13	Connected parallel hybrid architecture. . . . .	74
4.14	Independent parallel hybrid architecture. . . . .	74
4.15	(a) Remaining charge in the battery pack; (b) Total mass of the aircraft. . . . .	79
4.16	(a) Control input; (b) Approximate Specific Fuel Consumption. . . . .	80
4.17	(a) Remaining charge in the battery pack; (b) Approximate Specific Fuel Consumption. . . . .	81
4.18	HEA Simulink model . . . . .	82
4.19	Turbine engine. . . . .	83
4.20	Simulink generated time history for the fuel consumption. . . . .	84
4.21	Fuel consumption with different battery configurations; cases 1 and 2 are connected configurations; cases 3 and 4 are independent configurations. . . . .	86
5.1	An example of a hybrid ground-air transportation network . . . . .	93
5.2	The Anaheim network where the candidate vertiport locations are marked with colored circles. . . . .	104
5.3	The optimal air and ground traffic network loading when vertiport selection budget $\gamma = 8$ . . . . .	106
5.4	Vertiport network example. . . . .	109
5.5	Task network example. . . . .	111
5.6	Vehicle route for the feasible task path $1 \rightarrow 3 \rightarrow 5 \rightarrow 6 \rightarrow 7$ in Fig. 5.5. . . . .	112

5.7	Geographic network with 8 vertiport . . . . .	120
5.8	Paths obtained from greedy algorithm. . . . .	121

## LIST OF TABLES

Table Number	Page
2.1 Eviation Alice technical data, including estimated parameters. . . . .	9
2.2 SOUL technical data. . . . .	9
2.3 Conceptual HEA technical data, including estimated parameters. . . . .	11
2.4 Technical data of an existing NMC cell. . . . .	11
2.5 Technical data of a high energy NMC cell. . . . .	15
3.1 Comparison of the total cost (Ah) and terminal time (minutes) with Kaptsov and Rodrigues's (K/R) results. . . . .	34
3.2 Comparison of total cost and time between two battery models. . . . .	36
3.3 Comparison of cost and time between different battery configurations . . . . .	38
3.4 Comparison of total costs with three distinct battery models. . . . .	49
4.1 Fuel consumption of the climb phase with different battery pack configurations. . . .	84
5.1 Logical constraints for vertiport locations marked in Fig. 5.2 . . . . .	105
5.2 Path assignment results. . . . .	120

## **Nomenclature**

### **Abbreviations**

AAM = Advanced Air Mobility

AEA = All-Electric Aircraft

DOC = direct operating cost

DP = dynamic programming

ECM = empirical circuit model

ESPPRC = elementary shortest path problem with resource constraints

EU = European Union

eVTOL = electric Vertical Takeoff and Landing

FAA = Federal Aviation Administration

HEA = Hybrid-Electric Aircraft

HEP = Hybrid Electric Propulsion

HEVs = Hybrid Electric Vehicles

ICE = internal combustion engine

MILP = mixed integer linear program

NASA = National Aeronautics and Space Administration

ODE = ordinary differential equations

OP = orienteering problem

RAM = Regional Air Mobility

SFC = specific fuel consumption

SOC = state of charge

SPM = single particle model

TOPTW = team orienteering problem with time window

TSP = traveling salesman problem

UAM = Urban Air Mobility

## ACKNOWLEDGMENTS

I cannot think of a better way to start the acknowledgments than by sincerely thanking my mom, Mianmian Wang, and my dad, Jun Wang. The pillars you have positioned beneath my journey with your dedication, sacrifice, and unwavering support are immeasurable. Mom, your nurturing embrace and boundless devotion have shaped me in ways that are difficult to articulate. Your steadfast belief in my potential sustained me through hard times. Dad, your teachings of integrity and goodwill have been a constant source of motivation. Your wisdom has propelled me forward and guided me through challenges. Expressing the depth of my gratitude is a task that words seem inadequate to fulfill. My love for both of you knows no bounds, and I am truly thankful for all that you've bestowed upon me.

I have to also thank my maternal grandmother, Shuiqin Wang, the most lovely and kind person I have ever known. Your diligence, courage, and genuine nature have been a beacon, inspiring me to be a better person. Your life's wisdom, a veritable treasure trove, has enriched my journey. I hope that I have been able to bring a sense of pride to your heart.

To my dearest aunt, Li Wang, thank you for being my faithful friend, for always placing me in top priority, and for encouraging me to pursue my dream when others do not comprehend. Your ambition, self-discipline, and perseverance have inspired me to reach for higher horizons. My uncle, Guojian Li, your patience and generosity have left an indelible mark on my heart. Your presence and support have been a source of strength.

I have to express my gratitude to a few exceptional teachers who have played significant roles throughout my educational journey. Thank you, Ting Wang, for your candid praise that never minced words and for instilling in me boundless courage and confidence during moments of timidity and sensitivity. To my master advisor, Professor Long Zhao, your role in my life extends beyond being an excellent mentor; you are also a treasured friend. Throughout the course of over three years during my master's journey, you have offered me profound guidance and encouragement.

What has truly enhanced my learning experience is your commitment to science and your expansive philosophical perspective on life. The impact of your subtle influence over these three years has solidified my determination to pursue a path in research. To Professor Changyun Zhang, it is a great honor to have you as my co-advisor. To Nan Gao, I want to express my heartfelt appreciation for being an incredible mentor not only for my master's thesis but also for the various challenges life has presented. Your intelligence always amazes me, and your patience and guidance played a pivotal role in the success of my master's journey. Moreover, your presence in my life goes beyond that of a mentor – you've become a big brother to me.

I consider myself incredibly fortunate to have been blessed with numerous cherished friends throughout my life. They celebrate with me during times of joy and provide unwavering support when I need it the most. To my dearest and most loyal friend, Wenqing Huai, for caring and looking out for me despite the great distance across the oceans and for always being straightforward with me, offering both praise and constructive criticism whenever needed. I hold the great honor of being your son, Yi Yang's godmother, and having you in my life fills me with immense gratitude. To Xiaoxuan Wang, as I've often mentioned, the reason why I pursue my PhD journey in Seattle lies with you. We have stood by each other through significant life moments, traversing the paths of high school, college, marriage, and more. You are my beacon of warmth and strength in this cold and rainy city. Your passion for life and your persistent determination have provided me with an enduring source of motivation. To Xiangnan Feng, thank you for being my best friend with whom I can discuss anything and for being my invaluable unpaid personal mathematics tutor. Your companionship and support have been unwavering, especially in our shared journey as PhD candidates, where we navigate challenges and endure together. To Shiyao Lin, thank you for helping and supporting me in my first year of PhD. Your kindness warmed me a lot during those challenging times. Your presence made a significant difference, and I am truly thankful for your assistance. To Zhuo Feng and Ziwei Liu, our shared overseas experiences have warmed my heart deeply. To Ruiqi Liao, thank you for being my best hiking buddy and a loyal friend with whom I can share anything. To Mengyin Wang, thank you for being an amazing roommate and loyal friend to me.

To Suryanarayana Kolluri and Krishna Shah, I have benefited tremendously from working with

both of you. I count it a privilege that I got to collaborate with you on my first PhD project. The wealth of knowledge I've acquired from the two of you has paved the way for my subsequent academic pursuits, encompassing not only a strong foundational understanding but also a dedication to research practices.

To Dan Calderone, thank you for being such an exceptional mentor and collaborator to me. Your guidance and support provided me with my first teaching opportunity, which in turn paved the way for me to become an independent instructor for graduate students. Your insights into linear algebra have genuinely opened up a new world to me. I truly wish that every beginner in the field of control could have the privilege of learning from you.

To Yue Yu, it has been a great pleasure to work with you on our cutting-edge project. Your extensive and profound grasp of mathematical knowledge has left an indelible impression on me, serving as a constant source of inspiration. Moreover, I've gained valuable insights beyond the scope of our project, observing your rigorous approach, dedication to refining expression, and commitment to effective presentation. Your example has driven me towards becoming a more accomplished and dedicated researcher.

To Shahriar Talebi, someone with whom I'm fortunate to be in the same lab. Your exceptional passion and kindness as a fellow PhD student have left an indelible mark on me. Your enthusiasm towards both research and life always astounded me. As I navigate my own PhD journey, your remarkable example serves as a constant inspiration, propelling me forward with determination and purpose.

To Niyousha Rahimi, our shared experiences resonate so deeply that it feels as though I've encountered a soulmate. My only regret is that we didn't have the chance to exchange our joys and sorrows sooner. To Kuang-Ying (Eddie) Ting, your presence as a good friend has been so remarkable that I'll deeply miss our casual conversations and small talk. To Spencer Kraisler, your curiosity and self-discipline never cease to inspire me. To Aditya Deole, the breadth and depth of your knowledge and interest always amaze me. I would also like to express my heartfelt gratitude to Beniamino Pozzan, Josh Holder, Qishi (Jackson) Zhou, Siavash Alemzadeh, Dillon Foight, Soumya Vasisht, Mathias Hudoba de Badyn, Taylor Reynolds, Bijan Barzgaran, Jingjing Bu, Henk van

Waarde for their warm presence, enlightening discussions, and unique qualities that have made this journey unforgettable.

To Camron Call, Raju Mattikalli, and Kamiar Karimi, it is such a privilege for me to collaborate with you. Your immense knowledge and practical experiences provide tremendous insights into my research.

To Lillian Ratliff, I feel so lucky that my first job at UW was to work for you. Your patience and approachability made my first job experience seamless and efficient. Having you as a part of my committee is a true honor. To Kristi Morgansen, thank you for trusting me to teach a graduate course. Your organized lecture notes contributed to a smooth teaching process. As a female scientist and a strong presence in a male-dominated field, you will always be my role model. To Venkat R. Subramanian, my gratitude goes out to you for your mentorship and assistance during our Boeing project. Your guidance has been invaluable.

To Mehran Mesbahi, the best advisor a PhD student can ask for. You are a perfect combination of a rigorous scientist and an artist with boundless creativity. Collaborating on research with you has been an incredibly enriching experience. Not only do you offer sound and foundational suggestions, but you also ignite my imagination with cutting-edge and audacious ideas. A friend of mine, who is leading a startup focused on electric aircraft, once inquired about how I chose this groundbreaking new field for my PhD topic. I shared that it all began when I came across a paper you shared five years ago – that marked the beginning of my PhD journey. Furthermore, you are such a wise and funny person. Your empathetic understanding and warm support during my toughest days are greatly appreciated. I genuinely count myself lucky to be your student and aspire to be a lifelong friend.

To my beloved husband, Yiren Shen, thank you for being my bedrock throughout my degree. Building a life in a foreign land is extremely challenging, let alone when one of the family members is on her way to getting a PhD degree. We have overcome so many obstacles and difficulties. I simply couldn't have achieved this without you by my side. Your unending love and belief in me, even in the face of my flaws, have been my constant anchor. From you, I have learned how to communicate efficiently with those closest to me, how to deal with my depression and anxiety, and how to be

a better person. Your intelligence and self-discipline stand as a shining model that inspires me to strive for excellence. Planning our future together is my enduring source of motivation. Thank you for being my source of encouragement, my pillar of support, and the heart that has made this journey truly worthwhile. So no matter how many times, I still wanna say: I love you, dear. Let this be my last word.

Mengyuan Wang, August 30, 2023.

## Chapter 1

### INTRODUCTION

At first glance, electric aircraft may appear futuristic, although the concept dates back to the late nineteenth century. The first electrically powered airship was developed in 1883. The first manned electric aircraft, designed by Fred Militky, piloted by Heino Brditschka, and powered by Nickel-cadmium batteries, flew for nine minutes on October 21, 1973 [1]. Electrically propelled aircraft are powered by electricity, which can be stored in batteries or fuel cells. This dissertation focuses on electric aircraft powered by batteries.

All-Electric Aircraft (AEA) have numerous advantages over conventional fuel-burning aircraft. The electric motor is significantly more efficient than the conventional gas engine, enabling electric aircraft to produce the same amount of power while consuming much less energy. Moreover, the electric motor generates less noise, allowing for more flexible routing of electric aircraft, whereas conventional aircraft are generally more constrained in terms of both routes and schedules due to noise restrictions in urban areas. Additionally, the absence of bulky fuel tanks and engines allows for more flexible aerodynamic designs, thereby improving flight performance.

Furthermore, the electric aircraft have fewer moving parts, and the electric motor has a lower operating temperature and more predictable wear and tear patterns than the gas engine, resulting in fewer maintenance costs and a safer system. In addition, an all-electric system is able to power auxiliary equipment directly without the need for mechanical or hydraulic transfer systems. This mechanism simplifies the entire system significantly and enhances safety. If we ignore the production procedure of batteries, all-electric aircraft are also considered to be emission-free. Given rising concerns about climate change and sustainability, AEA has the potential to provide a mode of flight that is more efficient, flexible, and environmentally friendly. Developing optimal trajectories for AEA is one of this dissertation's primary contributions.

Despite the significant potential of AEA, there are several drawbacks that demand consideration. Due to the current relatively low battery energy density, AEA has limited range and a heavy weight.

Moreover, the lengthy charging time imposes additional operational restrictions. In addition, infrastructure, regulations, and public acceptance are enormous hindrances to the development of AEA as a viable alternative to conventional aircraft. To overcome these obstacles, designing Hybrid-Electric Aircraft (HEA) has become a viable approach to clean aviation in the coming decades, particularly for longer air travel.

HEA offer several advantages over conventional aircraft, including improved fuel efficiency, reduced emissions, and less noise pollution. In conventional aircraft, all flight phases with varying power requirements are powered by gas engines, resulting in inefficiency since the engines cannot be optimized for each phase. Most commercially available HEA are modified from conventional aircraft by reducing the original gas engines and adding electric paths. By doing so, the electric motors and the engines can drive the aircraft together during the climb phase, and the engine is designed optimally for the cruise phase, which is the most significant phase in fuel consumption. The use of smaller engines also reduces weight, resulting in further fuel efficiency gains. Compared with AEA, HEA offers longer ranges and fewer infrastructure requirements, making it a viable bridge between conventional aircraft and future commercial AEA. The second direction of this dissertation's contribution is to study power allocation algorithms for HEA and parallel hybrid electric configurations.

The development of electrically propelled aircraft is facilitating a broader transformation in aviation, including the emergence of Advanced Air Mobility (AAM) - which aims to develop an aerial transportation system capable of providing efficient, safe, and environmentally friendly transportation in urban and suburban areas using cutting-edge technologies, such as electrically propelled aircraft, automated air transportation management, advanced infrastructure, etc. AAM seeks to deliver a new level of mobility that decreases traffic congestion, travel time, and pollution while enhancing accessibility and safety. AAM is a broader concept that includes Urban Air Mobility (UAM), which transports passengers and cargo within a city, and Regional Air Mobility (RAM) that focuses on intraregional flights [2]. Among numerous research topics about UAM, this dissertation focuses on optimal vertiport selection and task assignment with time-dependent constraints.

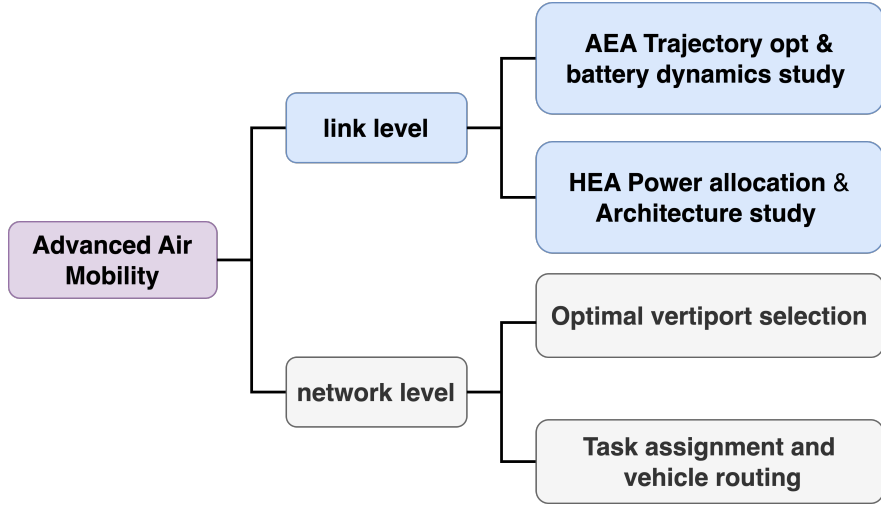


Figure 1.1: Research topics explored in this dissertation.

### 1.1 Statement of contributions

Fig. 1.1 presents a comprehensive overview of this dissertation's contributions, which are divided into two main layers: the link level and the network level. At the link level, our primary objective is to improve the performance of individual aerial vehicles by designing optimal trajectories for AEA, developing power allocation algorithms, and investigating different configurations for HEA. At the network level, we focus on vertiports selection and task assignment for AAM with optimization strategies.

The research on AEA trajectory optimization begins with the investigation of a single phase (the cruise phase) with different battery dynamical models [3]. The operating cost minimization problem is formulated as an optimal control problem. This optimal control problem leads to a singular control structure when the thrust is taken as the control input. The Pontryagin's minimum principle is applied to identify the necessary conditions for optimality, and the theoretical analysis is subsequently verified through numerical results obtained from a commercial solver. This algorithm is then extended to the climb and descent phases [4], leading to a comprehensive examination of trajectory optimization algorithms for AEA. Further analyses are conducted to explore control input profiles with different battery models. The DOC minimization for AEA over a complete integrated flight profile is also examined. A multi-phase optimization problem is formulated and

solved as a single optimal control problem, avoiding introducing discontinuities due to separate optimal control problems for different phases. Finally, a Simulink model is developed to explore the battery performances with battery models with distinct fidelity, and comparisons between optimized flight profiles with three distinct battery models are provided.

In regard to HEA research, we pursue two directions in this dissertation. The first direction focuses on developing the power allocation algorithm when flight profiles are given in advance [5]. An optimal control problem for a small HEA is formulated and solved to distribute power in the propulsion system. Similar to the trajectory optimization approach used for AEA, the minimum principle is applied to identify the necessary conditions for optimality. Numerical analyses reveal that the engine should be operated in its efficient region while utilizing the battery capacity to achieve fuel minimization. However, the fuel savings from this optimal strategy are found to be limited. This algorithm is then applied to a larger conceptual HEA; however, the fuel savings remain minimal, leading to the second direction we have conducted for HEA: whether charging the battery during flight is fuel efficient.

Two parallel hybrid electric architectures are compared in terms of fuel consumption [6]. The connected architecture has a mechanical connection between the engine and the electric motor, allowing in-flight battery charging for improved engine fuel efficiency. The independent architecture does not have a mechanical connection, enabling easy transitions from conventional to hybrid aircraft and from hybrid aircraft to all-electric aircraft. A finite-dimension optimization problem is formulated and applied to a 19-seat conceptual aircraft to compare the fuel usage of these two architectures. The numerical results indicate that in-flight battery charging provides negligible fuel savings for the proposed aircraft model. Increasing onboard battery capacity is more fuel-efficient than in-flight charging. The connected architecture's complexities, challenges in transitioning to all-electric aircraft, and potential battery degradation in harsh flight environments make the independent architecture a more practical choice.

Regarding UAM, we address the vertiport selection problem by introducing a mathematical model to determine the optimal vertiport location and capacity, aiming to minimize traffic congestion within the hybrid ground-air transportation network [7]. Our model is equivalent to a mixed-integer linear program and is illustrated using the Anaheim transportation network.

In this dissertation, task assignment and vehicle routing problems for UAM are solved jointly.

By constructing a task network based on a sequential timing of tasks, we assign a set of tasks with a sequence to a vehicle. The task assignment problem is transformed into identifying multiple paths in a network that maximize the overall profit. By solving the task assignment problem in a centralized way, we are able to answer a number of fundamental questions for UAM.

## **1.2 Outline of dissertation**

This dissertation is organized as follows. Chapter 2 provides background information that serves as a common reference for subsequent chapters. We introduce several aircraft models, battery models, and system dynamics; we also give formal statements of the tools from optimal control theory that will form the theoretical foundation for algorithms developed in this dissertation.

Chapter 3 discusses trajectory optimization algorithms for AEA. Several optimal control problems are formulated for different flight phases with distinct battery models. The minimum principle is applied to these optimal control problems to obtain the necessary conditions for optimality; numerical results from a commercial optimization solver are provided. A Simulink model is developed to verify the proposed algorithms.

In Chapter 4, a power allocation algorithm for a single-seat hybrid-electric aircraft is introduced, accompanied by both theoretical and numerical analyses. Then two parallel hybrid electric propulsion structures—distinguished by the presence or absence of a mechanical connection between the engines and the electric motors—are discussed and compared in terms of fuel consumption.

Chapter 5 first discusses the vertiport selection problem in §5.1 and §5.2; then the task assignment and vehicle routing problem is presented in §5.4.

Chapter 6 provides concluding remarks and a glimpse into future research directions.

## Chapter 2

### PRELIMINARIES

In recent years, aircraft electrification has been a thriving area, and hundreds of projects throughout the world are developing electrically-propelled aircraft. Two existing aircraft models and one conceptual model are examined in this dissertation. The state of the art of electrically propelled aircraft is presented in §2.1, as well as technical data and assumptions for selected aircraft models.

The formulation of optimal control problems relies heavily on system dynamics. Nonlinear longitudinal flight dynamics and several distinct battery dynamics are introduced in §2.2. The algorithms developed in this dissertation depend heavily on optimal control theory (in particular, the Pontryagin's minimum principle). To make this dissertation more self-contained, a review of optimal control theory is given in §2.3.

#### **2.1 Aircraft models**

There are a number of available configurations for AEA in the market. For example, E-fan 1.0 is a prototype two-seat AEA developed by Airbus [8]. The test flight for E-fan 1.0 was conducted in April 2014; this aircraft was built for pilot training and crossed the English Channel in July 2015. Pipistrel ALPHA Electro is a light sport electric aircraft designed for training purposes for flying schools. As such, flight performances for this aircraft are rather targeted, e.g., short take-off distance, powerful 1000+ fpm climb, and endurance of one hour [9]. Taurus G4 is a 4-seat fully electric aircraft designed by Pipistrel, which won the National Aeronautics and Space Administration (NASA) Green Flight Challenge in 2009 [10], which was a competition for quiet, practical, green aircraft. The most distinguishing feature of the Taurus G4 is that it is a twin-fuselage plane. Joby Aviation's S4 air taxi is a 5-seat eVTOL (electric vertical take-off and landing) with a 150-mile max range. The full-scale demonstrator took to the skies in 2017; it received airworthiness approval from the U.S. Air Force in 2020. Eviation Alice is a nine-passenger aircraft [11]; MagniX provides the electric propulsion system for this aircraft. The Eviation Alice successfully completed its first

flight on September 27, 2022; currently, Eviation aims to complete Federal Aviation Administration (FAA) type certification and service entry in 2027. In this dissertation, Eviation Alice has been chosen as our baseline aircraft model for developing energy-optimized flight profiles for AEA.

The most commonly used configurations for HEA are series, parallel, and series-parallel architecture. The Diamond DA-36 E-star is the first series HEA that accomplished its maiden flight in 2011 [12, 13]. This aircraft was developed by Siemens, EADS, and Diamond Aircraft. The Diamond DA-36 E-star is powered by a Siemens 70 kW electric motor and a 30 kW internal combustion engine (ICE). EcoEagle is a parallel HEA developed by Embry-Riddle Aeronautical University. It was built for the Green Flight Challenge [10]. The original Pipistrel Panthera [14] is a lightweight, four-seat, fuel-powered aircraft developed by Pipistrel. In 2013, the project received funds from the European Union (EU) to develop series HEA. The Pipistrel Panthera mockup received a series hybrid electric powertrain, ground testing a 200 kW motor driven by battery only, by a 100 kW generator (powered by fuel) only, and by both combined. Following this achievement, the EU continued to fund Pipistrel to develop series HEA with a project named Mahepa. The flight test is planned for 2020. E-fan X [15] is the series HEA demonstrator developed by Airbus, Siemens, and Rolls-Royce. One of the original four turbofans is replaced by a Siemens 2 MW electric motor. Different from the aforementioned lightweight HEA with ICEs, E-fan X is a mid-scale aircraft mounted with turbofan engines and an electric motor; its maiden flight is planned for 2020.

### 2.1.1 *Eviation Alice*

Eviation Alice [16], shown in Fig. 2.1, is an all-electric, nine-passenger aircraft powered by two electric motors; trajectory optimization for AEA with distinct battery models is studied based on Eviation Alice in this dissertation. Table. 2.1 lists some of the key aircraft parameters; we note that parameters with \* are only estimated for the purpose of subsequent analysis.

### 2.1.2 *SOUL*

In [17], Friedrich and Robertson modified an ultralight single-seat aircraft SONG with a 15kg ICE, shown in Fig. 2.2<sup>1</sup>. A tuned Honda GX160 with an estimated maximum output power of

---

<sup>1</sup>Figure of the aircraft SONG comes from <https://www.songairplane.com/>



Figure 2.1: Eviation Alice.

7.5kW and a customized motor of 12 kW has been chosen as the new powertrain configuration. The developed HEA is referred to as SOUL. Table.2.2 lists some of the key parameters of SOUL.

### 2.1.3 Conceptual HEA model

A conceptual HEA propulsion system model developed by Finger, *et al.* [18] is employed for our subsequent analysis. Finger, *et al.* considered an existing 19-seat commuter aircraft as the baseline and examined two approaches for the HEA preliminary design. The conventional aircraft was re-sized to accommodate the hybrid electric propulsion technology. Key characteristics of one of the configurations used in [18] are shown in Table 2.3. Note that parameters with \* are only estimated values.

In [18], the authors did not specify the engine model, battery model, or electric motor model; instead, the reference weight and some characteristics for these components were provided. In this work, the following models are selected for the propulsion system—with some parameters slightly different from those in [18]:

Table 2.1: Eviation Alice technical data, including estimated parameters.

Parameters	Values
Wing area*	18m <sup>2</sup>
Maximum take-off weight	6350 kg
Battery capacity*	2170 Ah
Battery pack nominal voltage*	360 V
Maximum speed	630 km/h
Total system efficiency*	0.8
Zero-lift drag coefficient*	0.024
Induced drag coefficient*	0.039

Table 2.2: SOUL technical data.

Parameters	Values
Wingspan	11.2m
Length	5.6m
Height	1.9m
Airfoil	UAG 88-143/20
Propulsion	Hybrid
Wing area	10.3m
Airframe weight	78kg
Empty weight	103kg
MTOW	235kg
Fuel tank	25 l
Cruise speed	80-110km/h
Maximum speed	143km/h

1. **Turboprop engine:** the PT6A-135A engine by Pratt & Whitney is selected; the weight of this engine is 153 kg; its maximum output power is 560 kW; and its average specific fuel consumption (SFC) is 356 g/kW/h. In this work, it is assumed that the engine runs at a fixed rotational speed; the SFC and the fuel flow rate can be represented as functions of the output power of the engine, shown in Fig. 2.3.
2. **Electric motor:** the Magni250 by MagniX is selected; it weighs 72 kg; its maximum output power is 280 kW; the total efficiency is assumed as 95%.



Figure 2.2: Ultralight aircraft SONG.

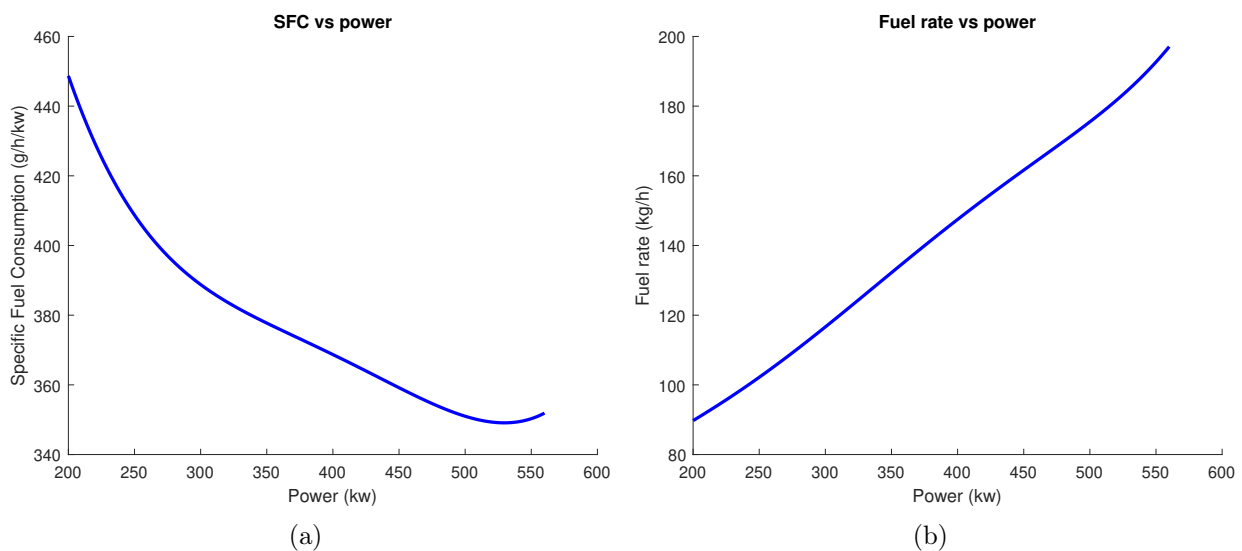


Figure 2.3: Fuel consumption characteristics of the engine: (a) SFC vs output power; (b) fuel flow rate vs output power.

Table 2.3: Conceptual HEA technical data, including estimated parameters.

Parameters	Values
Wing area	32 m <sup>2</sup>
Maximum take-off weight	6385 kg
Cruise altitude	3000 m
Battery capacity*	400 Ah
Battery pack nominal voltage*	540 V
Propeller efficiency*	0.7
Zero-lift drag coefficient*	0.024
Induced drag coefficient*	0.056

3. **Battery cells:** in [18], the authors assumed a futuristic value for the energy density of battery cells that was significantly greater than the current level of battery technology. In this work, an existing battery model from the Korean battery manufacturer Kokam is utilized. The technical data for this battery is listed in Table. ???. For the battery pack configuration, it is

Table 2.4: Technical data of an existing NMC cell.

Model	Capacity	Weight	Energy Density
SLPB140460330	200 Ah	3.96 kg	189 Wh/kg

assumed that all battery cells operate identically and that the parallel and series connections of the battery pack do not affect the output voltage and the state of charge of each cell. In addition, it is assumed that the battery cell has no internal state dynamics, resulting in a constant output voltage of 3.6 V. For this conceptual aircraft, it is assumed that the battery pack has two parallel paths and 150 cells connected in series in each path. This configuration has an output voltage of 540 V and a total capacity of 400 Ah. The battery pack weighs 600 kg, which is greater than the value in [18]. Other battery pack configurations are also examined in Section 4.3.

## 2.2 Dynamics

The system dynamics is expressed as ordinary differential equations (ODE); these ODEs play a crucial role when formulating optimal control problems. In this dissertation, flight dynamics and battery dynamics are considered to design energy management algorithms for electrically propelled aircraft.

### 2.2.1 Flight dynamics

The full flight dynamics of an aircraft is rather involved. In this dissertation, we only focus on the longer period (Phugoid) mode in the longitudinal direction, and the nonlinear dynamics is given by,

$$\dot{y} = v \cos \gamma, \quad (2.1a)$$

$$\dot{h} = v \sin \gamma, \quad (2.1b)$$

$$\dot{v} = \frac{1}{m}(T \cos \alpha - D - W \sin \gamma), \quad (2.1c)$$

$$\dot{\gamma} = \frac{1}{mv}(T \sin \alpha + L - W \cos \gamma), \quad (2.1d)$$

where  $y$  is the horizontal position;  $v$  is the velocity of the aircraft;  $\gamma$  is the flight path angle;  $h$  is the flight altitude;  $m$  is the total mass of the aircraft;  $T$  is the thrust force, which is the control input in this paper;  $D$  is the drag force;  $W$  is the total weight of the aircraft;  $L$  is the lift force, and  $\alpha$  is the angle of attack. The lift and drag forces are computed by

$$L = \frac{1}{2}\rho S C_L v^2, \quad (2.2a)$$

$$D = \frac{1}{2}\rho S C_D v^2, \quad (2.2b)$$

where  $\rho$  is the air density;  $S$  is the wing area;  $C_L$  is the lift coefficient, and  $C_D$  is the drag coefficient, given by

$$C_D = C_{D,0} + K C_L^2, \quad (2.3)$$

where  $C_{D,0}$  is called zero-lift drag coefficient, and  $K$  is called the induced drag coefficient. These two coefficients vary with the aircraft model and are usually provided by the manufacturer.

### 2.2.2 Battery dynamics

Three models with distinct fidelity for Lithium-ion batteries are examined to be incorporated into the operation of AEA. The first is the “ideal” model with a constant voltage; the second one is the so-called empirical circuit model (ECM) [19], in which the voltage is a nonlinear function of the state of charge (SOC) of the battery pack; the third is the single particle model (SPM), a physics-based model consisting of a set of partial differential equations and differential algebraic equations [20]. In the sequel, it is assumed that all battery cells in the battery pack operate in an identical manner, and the parallel and series configurations for the battery pack have a negligible effect on the voltage and the SOC of each cell.

#### *Ideal battery model*

In this model, it is assumed that the output voltage of the battery cell is constant. That is, the voltage does not depend on the SOC, ambient temperature, or the current passing through the battery. In addition, it is assumed that the internal resistance of the battery is zero. This battery model can be expressed as,

$$U_{\text{cell}} = U_{\text{nom}}, \quad \frac{d\theta_{\text{cell}}}{dt} = -\frac{I_{\text{cell}}(t)}{Q_{\text{cell}}}, \quad (2.4)$$

where  $U_{\text{nom}}$  is the nominal battery cell voltage, often provided by the manufacturer;  $\theta_{\text{cell}}$  is the SOC of the battery cell;  $I_{\text{cell}}$  is the current passing through the battery cell;  $Q_{\text{cell}}$  is the total charge of the battery cell. For Eviation Alice, we assume that the nominal voltage of the battery cell is 3.6V. The voltage and capacity of the battery pack are related as,

$$U = U_{\text{cell}} * n_{\text{series}}, \quad Q = Q_{\text{cell}} * n_{\text{parallel}}. \quad (2.5)$$

Note that the above relations hold for all battery models. For Eviation Alice, it is assumed that the battery pack has 31 parallel paths and 100 cells connected in series in each path; hence, the nominal voltage of the battery pack is 360V. The cell capacity is 70Ah (see in Table.2.5); hence the

capacity of the battery pack is 2170Ah. The impact of the battery configuration (different voltages) on AEA's performance will be examined in the sequel.

### *Empirical Circuit Model (ECM)*

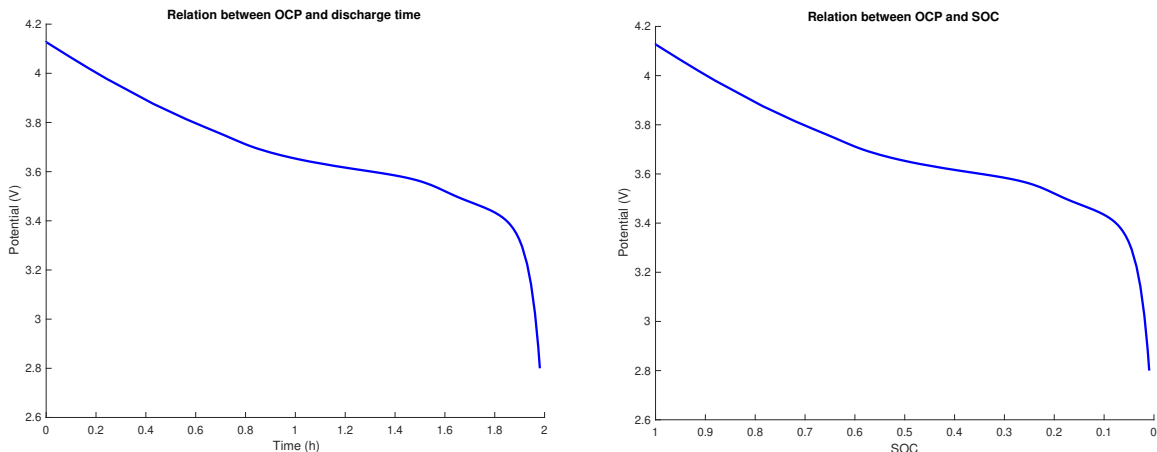
ECM is usually obtained by fitting the experimental open circuit potential data into a high-order polynomial; it provides the relation between the voltage and the SOC of the battery. This model is defined by,

$$\frac{d\theta_{\text{cell}}}{dt} = -\frac{I_{\text{cell}}(t)}{Q_{\text{cell}}} \quad (2.6a)$$

$$U_{\text{oc},\text{cell}}(\theta_{\text{cell}}) = \sum_{k=0}^8 a_k \theta_{\text{cell}}^k \quad (2.6b)$$

$$U_{\text{cell}} = U_{\text{oc},\text{cell}}(\theta) - R_{\text{cell}} I_{\text{cell}}(t), \quad (2.6c)$$

where  $U_{\text{oc},\text{cell}}$  is the open circuit potential of the battery cell, which is a function of the SOC;  $a_k (k = 0, \dots, 8)$  are the coefficients of the polynomial for  $U_{\text{oc}}$ , and  $R_{\text{cell}}$  is the internal resistance of the battery cell.



(a) Relation between open circuit potential and time. (b) Relation between open circuit potential and SOC.

Figure 2.4: Open circuit potential of a single battery cell.

The battery weight for Eviation Alice is 3600 kg, with battery cells provided by a Korean company, Kokam. The energy density of the battery cell that Kokam offered to Eviation is approximately 260 Wh/kg. This battery cell is customized for Eviation, and its technical data is not publicly available. In this dissertation, we adopt a similar battery specification. The technical data of the battery cells considered are given in Table 2.5.<sup>2</sup>

Table 2.5: Technical data of a high energy NMC cell.

Model	Capacity	Internal Resistance	Weight	Energy Density
SLPB120216216G2	70Ah	0.7mΩ	1.15 kg	225Wh/kg

Fig. 2.4 is obtained from simulation experiments when discharge rate = 0.5C. Note that after discharging for 100 minutes or when the state of charge is below 0.1, the voltage drops rapidly.

#### *Single Particle Model (SPM)*

Fig. 2.5 is the overall schematic of the simulation process of the SPM. The current density  $i_{app}$  is given as an input to the battery model for the specific time period or until the battery reaches the specified cut-off voltages. The lithium-ion cell can be charged/discharged multiple times based on the rocking chair concept. Fig. 3.1(b) depicts the single sandwich computational domain of the physics-based battery model. The model consists of (i) positive electrode (cathode), (ii) separator and (iii) negative electrode (anode). The entire cell is filled with electrolyte. When an external load is applied, the electrolyte helps lithium-ion to migrate from one region to another through a separator (a thin membrane), preventing direct contact between the electrodes. Simultaneously, the electrons are transferred through the current collectors and the external circuit. The current collectors are on both positive and negative ends. Typically, aluminum is used as a current collector for the positive electrode and copper for the negative electrode. When the battery is charging, Li<sup>+</sup> ions de-intercalate from the positive electrode and intercalate into the negative electrode. Conversely, Li<sup>+</sup> ions intercalate into the positive electrode through the electrolyte during discharging. During charge/discharge, Li<sup>+</sup> ions go back and forth between the negative electrode and the positive

---

<sup>2</sup><https://kokam.com/cell>

electrode, enabling the conversion of energy between chemical energy and electrical energy and the storage of electrochemical energy within the battery. Fig. 3.1(c) is the schematic depicting the op-

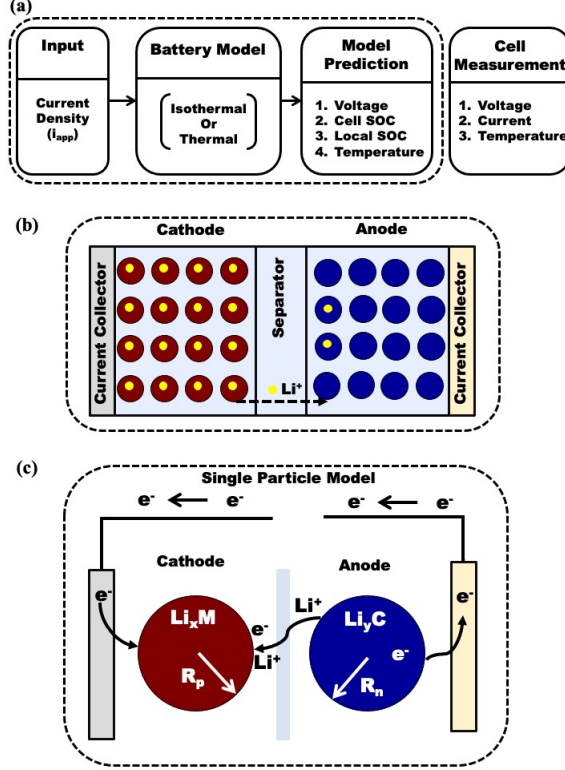


Figure 2.5: Single Particle Model illustration.

eration of SPM. The individual electrode is volume-averaged across the thickness and is assumed to be represented by a single particle of the active material. The electrolyte dynamics will be ignored in this work in order to reduce model complexity and increase computational efficiency for real-time simulations.

### 2.3 Optimal control methods

Pontryagin's Minimum Principle is a classical method used to derive the necessary conditions for the global optimal solution. In some literature, it is referred to as the maximum principle, and it was developed by Pontryagin and his students during the 1960s. The proof and further discussions

can be found in the original work of Pontryagin [21], one of the best resources on this subject. In this section, we briefly introduce the theorem in §2.3.1; and one of the special cases in optimal control problems: the singular optimal control problem in §2.3.2.

### 2.3.1 The minimum principle

Consider a dynamical system [22] of the form,

$$\dot{\mathbf{x}}(t) = f(t, \mathbf{x}(t), \mathbf{u}(t)), \quad \mathbf{x}(t_0) = \mathbf{x}_0, \quad t \in [t_0, t_f], \quad (2.7)$$

where  $\mathbf{x} : \mathbb{R} \rightarrow \mathcal{X} \subset \mathbb{R}^n$  is the *state* with  $n$  dimensions;  $\mathbf{u} : \mathbb{R} \rightarrow \mathcal{U} \subset \mathbb{R}^m$  is the *control*; both  $\mathbf{x}$  and  $\mathbf{u}$  are function of time;  $t_0, t_f \in \mathbb{R}_+$  are the initial and final time, respectively. The  $\mathcal{X}, \mathcal{U}$  represent the sets of admissible state and control, respectively. The function  $f : \mathbb{R} \times \mathbb{R}^n \times \mathbb{R}^m \rightarrow \mathbb{R}^n$  is referred to as the dynamics of the system. The following assumptions hold.

**Assumption 1.** *The function  $\mathbf{u}$  is piecewise continuous with respect to time; the set  $\mathcal{U}$  is compact.*

**Assumption 2.** *The function  $f$  is continuous in  $t$  and  $\mathbf{u}$  and  $\mathcal{C}^1$  in  $\mathbf{x}$ ; the Jacobian  $\nabla_{\mathbf{x}}f \in \mathbb{R}^x \times \mathbb{R}^x$  exists and is continuous in  $t$  and  $\mathbf{u}$ .*

We want to minimize the following cost functional,

$$J(\mathbf{u}) = \int_{t_0}^{t_f} L(t, \mathbf{x}(t), \mathbf{u}(t)) dt + K(t_f, \mathbf{x}_f), \quad (2.8)$$

where  $L : \mathbb{R} \times \mathbb{R}^n \times \mathbb{R}^m \rightarrow \mathbb{R}$  is the running cost;  $K : \mathbb{R} \times \mathbb{R}^n \rightarrow \mathbb{R}$  is the terminal cost;  $x_f$  is the final (terminal) state, which is a free parameter in most cases in this dissertation. The optimal control problem is formulated as

$$\min_{\mathbf{u}, t_f} J(\mathbf{u}) \quad (2.9a)$$

$$s.t. \quad \dot{\mathbf{x}}(t) = f(t, \mathbf{x}(t), \mathbf{u}(t)), \quad (2.9b)$$

$$\mathbf{x}(t_0) = \mathbf{x}_0, \quad t \in [t_0, t_f], \quad (2.9c)$$

$$\mathbf{x} \in \mathcal{X}, \quad \mathbf{u} \in \mathcal{U}. \quad (2.9d)$$

The minimum principle provides the necessary optimality conditions for **Problem (2.9)**. First, we define the Hamiltonian function for this problem as,

$$H(t, \mathbf{x}(t), \mathbf{u}(t), \boldsymbol{\lambda}(t)) = L(t, \mathbf{x}(t), \mathbf{u}(t)) + \boldsymbol{\lambda}(t) f(t, \mathbf{x}(t), \mathbf{u}(t)), \quad (2.10)$$

where  $\boldsymbol{\lambda}(t) : \mathbb{R} \rightarrow \mathbb{R}^n$  represents the so-called co-states.

Let  $\mathbf{u}^* : [t_0, t_f^*] \rightarrow \mathcal{U}$  be an optimal control and let  $\mathbf{x}^* : [t_0, t_f^*] \rightarrow \mathbb{R}^n$  be the corresponding optimal states trajectory. Then the minimum principle asserts that there exists a function  $\boldsymbol{\lambda}^* : [t_0, t_f] \rightarrow \mathbb{R}^n$  having the following properties [22]:

1.  $\mathbf{x}^*$  and  $\boldsymbol{\lambda}^*$  satisfy the canonical equations

$$\dot{\mathbf{x}}^* = H_{\lambda}(t, \mathbf{x}^*, \mathbf{u}^*, \boldsymbol{\lambda}^*), \quad (2.11a)$$

$$\dot{\boldsymbol{\lambda}}^* = -H_x(t, \mathbf{x}^*, \mathbf{u}^*, \boldsymbol{\lambda}^*), \quad (2.11b)$$

where  $H_{\lambda}$  denotes the partial derivative of  $H$  with respect to  $\boldsymbol{\lambda}$ ;  $H_x$  denotes the partial derivative of  $H$  with respect to  $\mathbf{x}$ ; we note that both  $\dot{\mathbf{x}}$  and  $\dot{\boldsymbol{\lambda}}$  are time derivatives of the corresponding variables with respect to time  $t$ .

2. The Hamiltonian must be minimized over the set of all admissible controls

$$H[t, \mathbf{x}^*(t), \mathbf{u}^*(t), \boldsymbol{\lambda}^*(t)] \leq H[t, \mathbf{x}^*(t), \mathbf{u}(t), \boldsymbol{\lambda}^*(t)]. \quad (2.12)$$

3. For the free-end time problem,  $H[t, \mathbf{x}^*(t), \mathbf{u}^*(t), \boldsymbol{\lambda}^*(t)] = 0$  for all  $t \in [t_0, t_f]$ ; when the terminal time is fixed, the Hamiltonian is a constant.

The minimum principle provides necessary conditions for global optimality; these conditions, in conjunction with specific initial and final conditions, characterize the solution to the underlying optimal control problem.

### 2.3.2 Singular optimal control problem

In some applications, the Hamiltonian is a linear function of the control input (here and henceforth, we only consider the situation when the control input is a bounded scalar variable) and can be expressed as

$$H(t, \mathbf{x}(t), \mathbf{u}(t), \boldsymbol{\lambda}(t)) = \bar{H}(t, \mathbf{x}(t), \boldsymbol{\lambda}(t)) + S(t, \mathbf{x}(t), \boldsymbol{\lambda}(t))u. \quad (2.13)$$

According to the minimum principle, the optimal control minimizes the Hamiltonian; hence, the following structure for the optimal control input is obtained,

$$u^*(t) = \begin{cases} u_{max} & S < 0 \\ u_{min} & S > 0 \\ ? & S = 0 \end{cases} \quad (2.14)$$

That is, on some time intervals, we allow  $S = 0$ , and the Hamiltonian is independent of the control input. The optimal control on this interval is called “singular”, and the corresponding segment for the optimal states trajectory is referred to as a singular arc.

Let us denote the control on the singular interval as  $u_s$ . In order to determine the value of  $u_s$ , it is usually sufficient to solve the following set of equations:

$$H = 0; \quad S = 0; \quad \dot{S} = 0, \quad (2.15)$$

where  $H = 0$  is given by the minimum principle;  $S = 0$  and  $\dot{S} = 0$  are specified by the assumption that on some interval  $S = 0$  for all  $t$  on that interval.

## Chapter 3

### **TRAJECTORY OPTIMIZATION FOR ALL-ELECTRIC AIRCRAFT**

Trajectory optimization involves designing a trajectory for a vehicle that optimizes a certain performance while satisfying a set of constraints. This is usually accomplished by solving an open-loop optimal control problem with constraints, enabling the determination of the optimal trajectory offline. Efficient and optimized trajectory planning plays a crucial role in enhancing the performance and efficiency of aircraft operations. Subsequently, the navigation system guides the aircraft to follow the designated trajectory.

The objective function of optimal control problems for aircraft trajectory optimization varies depending on the specific application. In the case of conventional aircraft, fuel consumption minimization often serves as the objective function due to its direct impact on operating costs and environmental sustainability. Trajectory optimization algorithms also consider the impact of various factors, such as altitude, speed profiles, and flight routes, on the total performance.

Similarly, for AEA, battery charge minimization can serve as a potential objective function since the battery pack is the sole power resource for the aircraft. Trajectory optimization directly affects range capabilities, which is a main challenge for AEA due to their very limited storage capacities resulting from current battery technologies. Kaptsov and Rodrigues [23, 24] defined the direct operating cost (DOC) for an AEA as a combination of time-related cost and battery charge cost.

Both flight dynamics and fuel consumption rates are crucial constraints in the formulation of the optimal control problem in trajectory optimization for a conventional aircraft. In the case of AEA, battery dynamics replaces fuel consumption rates and plays a significant role in the aircraft's operation. The electrical energy of the battery is generated by an electrochemical reaction between two metals of different affinities, which is highly sensitive to operating and environmental conditions. Accurately modeling battery dynamics can often be challenging.

Furthermore, the battery management system is essential for ensuring a safe and efficient flight. It must guarantee an effective and accurate estimation of the battery's state of charge, operating

conditions, and thermal management. On the other hand, the flight profile also affects the battery's operating conditions, thereby further affecting the battery's lifespan. For example, a fast flight speed may require high current draws from the battery pack, leading to high temperatures. Overheating will degrade battery performance and shorten its life. Conversely, extremely low temperatures, typical operating conditions for aircraft, can reduce the battery's efficiency and available power.

In summary, it is necessary to integrate battery dynamics and flight dynamics when formulating and solving the energy management problem for AEA. This integration allows for a comprehensive understanding of the complex relationship between battery performance, flight operations, and energy management strategies. Three battery models with distinct fidelity are introduced in §2.2. The ideal battery model and the empirical circuit model are integrated with flight dynamics to formulate the optimal control problem in this chapter; the single particle model is too complicated to be incorporated into the optimal control problem; hence, it is only examined in the Simulink environment.

This chapter is organized as follows. First, a comprehensive literature review on aircraft energy-efficient operation is provided in §3.1. Then, we introduce key elements for formulating optimal control problems as well as several example problems for different flight phases in §3.2. The optimal necessary conditions are discussed in §3.3. Numerical results and analyses are provided in §3.4. In §3.5, we present the Simulink environment and the validations of proposed algorithms.

### **3.1 Related works**

Aircraft energy-efficient operation can generally be approached as an optimal control problem, where the goal is to find the best trajectory that optimizes specific objective functions. An excellent survey of numerical methods for trajectory optimization was written by Betts [25], and several more recent articles also surveyed this field [26, 27, 28]. Betts [25] classified the techniques into indirect and direct methods. Indirect methods involve explicitly solving the optimality conditions derived via the calculus of variations, whereas direct methods do not require an analytic expression for the necessary conditions. In contrast, direct methods transform the optimal control problem into a nonlinear programming problem [29, 30, 31, 32] that can be effectively solved by a variety of well-developed algorithms. In this dissertation, the focus is on the indirect method, wherein the minimum principle is applied to the energy management problem for AEA.

Both Pargett *et al.* [33] and Franco *et al.* [34], for example, presented analyses of the singular optimal flight control problems and how to address them using the minimum principle. These works then utilized the results from optimality conditions to optimize energy consumption and derive optimal trajectories for the cruise phase for the Boeing 747-400 and Boeing 767-300ER, respectively. Villarroel *et al.* [35] defined the to-be-minimized cost index in detail and combined the minimum principle and the Hamilton-Jacobi-Bellman equation to obtain a sub-optimal solution for the true airspeed of the cruise phase in a state feedback form. Rivas *et al.* [36] considered the influence of air compressibility on the drag force and applied the indirect method to solve a range maximization problem. Cots *et al.* [37] studied the aircraft minimum time-to-climb problem with the singular perturbation method. Diaz-Mercado *et al.* [38] developed a nominal trajectory from the analyses of the necessary for optimality, then implemented a feedforward-feedback control scheme to make the aircraft robust under uncertainty and disturbances. Bonami *et al.* [39] formulated aircraft trajectory optimization as a mixed-integer nonlinear programming and solved it using Gauss-Lobatto direct collocation method. The aircraft is required to follow a route of waypoints, which are determined by integer variables.

For an AEA, the total charge drawn from the battery pack is typically of prime importance in energy management. Analogous to a conventional aircraft, one could construct and solve optimal control problems centered around battery utilization in order to design the energy management system for an AEA. Kaptsov and Rodrigues initiated formalizing the characterization of optimal speed for an electric aircraft via optimal control [24]. The objective function, in this case, was chosen to minimize the so-called Direct Operating Cost (DOC), which includes the time-related cost and the cost of depleting the battery charge. By applying PMP, the authors then obtained an analytical expression for the optimal cruise speed. In their subsequent work [23], Kaptsov and Rodrigues considered the internal resistance of the battery pack and obtained a different curve from the one presented in [24]. Barufaldi *et al.* [40] conducted research on optimal energy consumption for climb phases. The climb phase is quite energy-consuming and demanding on the propulsion system. As such, it becomes crucial to study algorithms that improve climb energy performance. Barufaldi analyzed the steady climb mode by formulating an energy minimization problem that can be solved by a parameter optimization method. This study also examined the linearized accelerated climb optimal control problem and applied the PMP for its solution. Falck *et al.* [41] characterizes

optimal trajectories for the NASA X57, which is a distributed electric testbed aircraft, using a Legendre-Gauss-Lobatto collocation control approach. This work also takes the thermal constraints into consideration in designing the optimal trajectory. Settele *et al.* [42] analyzed the impact of the Peukert effect on optimal control of AEA. Peukert's law indicates the approximate change in battery capacity at different discharge rates. They compared the optimal trajectory with different battery models, one with and one without considering the Peukert effect, and studied the impact of Peukert effect on the range of AEA. Paek *et al.* [43, 44] considered Li-ion battery degradation and studied the impact of several degradation scenarios on the long-term performance of AEA.

### 3.2 Problem formulation

An optimal control problem consists of a mathematical model of the system being controlled - represented by a set of ODEs, an objective function that describes the desired behavior of the system, and a set of constraints - for both control inputs and states that the system must satisfy. This section introduces these crucial elements for formulating control problems and presents several representative optimal control problems for the trajectory optimization of AEA investigated in this dissertation.

#### 3.2.1 Objective functions

In [35], the DOC of the cruise phase for a conventional aircraft is defined as

$$C_{\text{fuel}} = \int_{t_0}^{t_f} (C_t + C_f f) dt,$$

where  $C_t$  represents time-related costs, which contain hourly maintenance costs, flight crew salaries, and leasing costs;  $C_f$  represents the cost of fuel;  $f$  is the aircraft's fuel flow rate, usually in pounds per second;  $t_0$  is the initial time, and  $t_f$  is the final time. The trade-off between  $C_t$  and  $C_f$  is reflected by a cost index  $CI$ , computed as

$$CI_{\text{fuel}} = \frac{C_t}{C_f},$$

a large  $CI_{\text{fuel}}$  corresponds to a strong weight on the cost of travel time compared to the amount of fuel consumed. Following this definition, [23] provides the corresponding DOC for an AEA, given as

$$C = \int_{t_0}^{t_f} (C_t + C_q I) dt, \quad (3.1)$$

where  $C_q$  represents the cost of the battery charge, and the unit of  $C_q$  is U.S. dollars per Coulomb. Similarly, there is a trade-off effect between the time-related cost and the battery charge cost, represented by the cost index  $CI$ ,

$$CI = \frac{C_t}{C_q}, \quad (3.2)$$

where a large  $CI$  corresponds to a strong weight on the cost of travel time compared to the amount of the battery charge consumed. On the other hand, the consumed energy cost is usually more significant than the time-related cost for the climb phase since the flight time is short and the power consumed is large; as such, CI should be a very small value for the climb phase; when  $CI = 0$ , we have an energy minimization problem. The objective function of DOC minimization now becomes

$$J^* = \min \int_{t_0}^{t_f} (CI + I) dt, \quad (3.3)$$

where  $CI$  varies for different flight phases.

The other objective function considered in this dissertation is to maximize the cruise range, represented by

$$J = \max -y(t_f), \quad (3.4)$$

where  $y$  is the horizontal distance.

### 3.2.2 Battery dynamics and Simplified flight dynamics

When formulating the optimal control problem, the SOC of the battery pack ( $\theta$ ) is a crucial consideration, and its dynamic is given as

$$\dot{\theta} = -\frac{I}{Q}, \quad (3.5)$$

where  $\theta$  is the SOC of the battery pack;  $I$  is the current passing through the battery pack;  $Q$  is the battery pack's total charge. This equation holds for all battery models discussed in §2.2.

This dissertation considers distinct flight phases and provides the corresponding simplified flight dynamics to each phase.

#### *Constant altitude cruise phase*

For the constant altitude cruise phase, the following two assumptions are made:

**Assumption 3.** *During the cruise phase, the aircraft flies from one point to another at a constant altitude, the flight path angle  $\gamma = 0$  during flight, which leads to  $\dot{\gamma} = 0$  and  $\dot{h} = 0$ .*

**Assumption 4.** *The value of the angle of attack is constant and small, resulting in the following approximations  $\cos \alpha \approx 1$  and  $\sin \alpha \approx 0$ .*

With these two assumptions, the dynamic model simplifies to

$$\dot{y} = v, \quad (3.6a)$$

$$\dot{v} = \frac{1}{m}(T - D), \quad (3.6b)$$

$$L = W, \quad (3.6c)$$

where  $y$  is the horizontal position;  $v$  is the velocity;  $m$  is the total mass of the aircraft, which is a constant value for AEA;  $T$  is the thrust force;  $D$  is the drag force;  $L$  is the lift force;  $W$  is the total weight of the aircraft. The drag force and lift force are computed by Eq.(2.2).

The total weight of an AEA is a constant value; hence, during the constant altitude cruise phase, the lift force is also a constant value, which leads to a constant lift coefficient  $C_L$ .

#### *Accelerated climb phase*

The accelerated climb phase is assumed to follow **Assumption 4**. Additionally, during the climb phase, the lift coefficient is considered as a control input. The dynamics for the climb phase is given

by the following equations,

$$\dot{y} = v \cos \gamma, \quad (3.7a)$$

$$\dot{h} = v \sin \gamma, \quad (3.7b)$$

$$\dot{v} = \frac{T - D - W \sin \gamma}{m}, \quad (3.7c)$$

$$\dot{\gamma} = \frac{L - W \cos \gamma}{mv}, \quad (3.7d)$$

where  $\gamma$  is the flight path angle;  $h$  is the altitude. In this dissertation, we also assume that the descent phase follows the same dynamics as the climb phase.

### 3.2.3 Optimal control problems

We present the optimal control problem for the cruise phase and the climb phase, respectively.

#### *Constant altitude cruise with the ideal battery model*

Before we formulate the control problem, we need to connect the flight dynamics and the battery dynamics through the power relation in the propulsion system. For the aircraft flying at speed  $v$ , the required net power  $P_{\text{req}}$  is

$$P_{\text{req}} = T v = \eta P_{\text{bat}}, \quad (3.8)$$

where  $\eta$  is the total system efficiency, assumed to be a constant value in this dissertation;  $P_{\text{bat}}$  is the output power of the battery pack, and it can be computed as,

$$P_{\text{bat}} = -U \dot{Q} = UI, \quad (3.9)$$

where  $U$  is the voltage of the battery pack, and it is a constant value in the ideal battery model; combining Eq.(3.8) and Eq.(3.9), we obtain the following relation,

$$I = \frac{T v}{\eta U}. \quad (3.10)$$

The thrust force magnitude is constrained by

$$T_{\min} \leq T \leq T_{\max}, \quad (3.11)$$

where  $0 \leq T_{\min} \leq T_{\max}$  defines the permissible range for the thrust force, usually provided by the aircraft manufacturer. The boundary conditions in this scenario enforce a given horizontal position at both initial and final times, but the final time is not fixed:

$$y(0) = 0, \quad y(t_f) = y_d. \quad (3.12)$$

Given the objective function, dynamics, constraints, and boundary conditions, the DOC minimization problem with the ideal battery model is then stated as,

**Problem 1.** *Find the piecewise continuous control function  $T(t)$  and final time  $t_f \in \mathbb{R}$  that solves the following problem:*

$$J^* = \min_{T, t_f} \int_0^{t_f} (CI + \frac{Tv}{\eta U}) dt \quad (3.13a)$$

$$s.t. \quad \dot{y} = v, \quad (3.13b)$$

$$\dot{v} = \frac{T - D}{m}, \quad (3.13c)$$

$$T_{\min} \leq T \leq T_{\max}, \quad (3.13d)$$

$$0 \leq v(t) \leq v_{\max}, \quad y(0) = 0, \quad y(t_f) = y_d. \quad (3.13e)$$

If the constant battery pack voltage  $U$  is replaced with Eq.(2.6), we obtain the DOC minimization problem with the ECM, and  $\theta$  is added as one of the states.

**Problem 2.** *Find the piecewise continuous control function  $T(t)$  and final time  $t_f \in \mathbb{R}$  that solves*

the following problem:

$$J^* = \min_{T, t_f} \int_0^{t_f} (CI + \frac{Tv}{\eta U}) dt \quad (3.14a)$$

$$\text{s.t. } \dot{y} = v, \quad (3.14b)$$

$$\dot{v} = \frac{T - D}{m}, \quad (3.14c)$$

$$\dot{\theta} = -\frac{I}{Q}, \quad (3.14d)$$

$$0 \leq v(t) \leq v_{max}, \quad \theta_{min} \leq \theta(t) \leq \theta_{max}, \quad (3.14e)$$

$$y(0) = 0, \quad y(t_f) = x_d, \quad (3.14f)$$

where the current passing through the battery pack can be expressed as  $I = \frac{U - \sqrt{U^2 - 4RP_{bat}}}{2R}$ , and  $R$  is the internal resistance of the battery pack.

#### Accelerated climb with the ideal battery model

In the case of the accelerated climb phase, the power relation remains consistent with that of the constant altitude cruise phase. The objective function continues to be the minimization of the DOC. When  $CI = 0$ , we have the energy minimization problem. During the climb phase, in addition to the thrust force, we introduce the lift coefficient as the second control input to balance the lift force and the weight.

In addition to Eq.(3.11), the other constraint for the control input is given by

$$C_{L\min} \leq C_L \leq C_{L\max}, \quad (3.15)$$

where  $0 \leq C_{L\min} \leq C_{L\max}$  defines the permissible range for the lift coefficient, usually estimated by flight conditions. The boundary conditions, in this case, are given initial and final altitude. The final time continues to be unknown:

$$h(0) = h_i, \quad h(t_f) = h_d. \quad (3.16)$$

With the provided elements, the DOC minimization problem for the accelerated climb phase is then

stated as,

**Problem 3.** Find the piecewise continuous control functions  $T(t)$  and  $CL(t)$  and final time  $t_f \in \mathbb{R}$  that solves the following problem:

$$J^* = \min_{T, CL, t_f} \int_{t_0}^{t_f} (CI + I) dt \quad (3.17a)$$

$$\text{s.t. } \dot{\mathbf{x}} = f(t, \mathbf{x}, \mathbf{u}), \quad (3.17b)$$

$$\mathbf{x} \in \mathcal{X}, \quad (3.17c)$$

$$\mathbf{u} \in \mathcal{U}, \quad (3.17d)$$

with state  $\mathbf{x} = [y \ h \ v \ \gamma \ \theta]^\top$  and control  $\mathbf{u} = [T \ CL]^\top$ ;  $f$  is given by Eq.(3.5) and Eqs.(3.7);  $\mathcal{X}$  and  $\mathcal{U}$  designate state and control constraint sets, respectively.

### 3.3 Optimal necessary conditions analyses

We have formulated several optimal control problems for DOC minimization; the next step involves analyzing the optimal necessary conditions for these problems using the minimum principle.

#### 3.3.1 Constant altitude cruise phase

The Hamiltonian function of Problem 1 is given as,

$$H(t, \mathbf{x}(t), \mathbf{u}(t), \boldsymbol{\lambda}(t)) = CI + \frac{Tv}{\eta U} + \lambda_y v + \lambda_v \left( \frac{T - D}{m} \right), \quad (3.18)$$

where  $\lambda_y$  and  $\lambda_v$  are the co-states corresponding to  $y$  and  $v$ , respectively, and their dynamics with respect to time are given by the minimum principle as,

$$\dot{\lambda}_y(t) = -\frac{\partial H}{\partial y} = 0, \quad (3.19)$$

$$\dot{\lambda}_v(t) = -\frac{\partial H}{\partial v} = -\left[ \frac{T}{\eta U} + \lambda_y - \frac{\lambda_v}{m} D_v \right], \quad (3.20)$$

where  $D_v$  is the partial derivative of the drag force  $D$  with respect to the velocity  $v$ , which can be computed by the following equation,

$$D_v = \rho S C_D v = \rho S (C_{D,0} + K C_L^2) v = \rho S C_{D,0} v + \frac{4K W^2}{\rho S v^3}. \quad (3.21)$$

This Hamiltonian function can be rewritten as,

$$H = (CI + \lambda_y v - \lambda_v \frac{D}{m}) + \left( \frac{v}{\eta U} + \frac{\lambda_v}{m} \right) T = \bar{H} + ST.$$

Obviously, the Hamiltonian is a linear function of the control input  $T$ , and the thrust force is bounded by the maximum value that the propulsion system can provide and a minimum value to maintain the lift force. As such, we obtain a singular optimal control problem as described in §2.3.1.

According to the singular optimal control problem analyses in §2.3.1, Problem 1 has the following control structure,

$$T^* = \begin{cases} T_{max} & S < 0, \\ T_s & S = 0, \\ T_{min} & S > 0. \end{cases} \quad (3.22)$$

By substituting Eq.(3.22) into Eqs.(2.15), the following equations are obtained,

$$\bar{H} = CI + \lambda_y v - \lambda_v \frac{D}{m} = 0, \quad (3.23a)$$

$$S = \frac{v}{\eta U} + \frac{\lambda_v}{m} = 0, \quad (3.23b)$$

$$\dot{S} = -\frac{D}{m\eta U} - \frac{\lambda_y}{m} + \frac{\lambda_v}{m^2} D_v = 0. \quad (3.23c)$$

From Eqs.(3.23), we can deduce that the velocity  $v$  on the singular arc satisfies the following equation

$$D_v \cdot v^2 = CI \cdot \eta \cdot U. \quad (3.24)$$

The optimal velocity on the singular arc is determined by the cost index, the total efficiency of the propulsion system, and the voltage of the battery pack. In the case of the constant altitude cruise phase, all the elements on the right-hand side of the equation are constant. Therefore, we can

conclude that the velocity on this singular arc should remain constant. Consequently, the thrust force should be equal to the drag force, leading to the determination of the optimal control  $T_s$  on the singular arc.

### 3.3.2 Accelerated climb phase

The Hamiltonian function of Problem 3 is given as the form,

$$H(t, \mathbf{x}(t), \mathbf{u}(t), \boldsymbol{\lambda}(t)) = CI + I + \lambda_y \cdot \dot{y} + \lambda_h \cdot \dot{h} + \lambda_v \cdot \dot{v} + \lambda_\gamma \cdot \dot{\gamma} + \lambda_\theta \cdot \dot{\theta}, \quad (3.25)$$

where  $\lambda_y$ ,  $\lambda_h$ ,  $\lambda_v$ ,  $\lambda_\gamma$ , and  $\lambda_\theta$  are the co-states corresponding to state  $\mathbf{x} = [y \ h \ v \ \gamma \ \theta]^\top$ , respectively; and their dynamics are given as,

$$\begin{aligned} \dot{\lambda}_y(t) &= -\frac{\partial H}{\partial y}, & \dot{\lambda}_h(t) &= -\frac{\partial H}{\partial h}, & \dot{\lambda}_v(t) &= -\frac{\partial H}{\partial v}, \\ \dot{\lambda}_\gamma(t) &= -\frac{\partial H}{\partial \gamma}, & \dot{\lambda}_\theta(t) &= -\frac{\partial H}{\partial \theta}. \end{aligned} \quad (3.26)$$

We now substitute the dynamics of the states in the problem Eqs. (3.17) into the Hamiltonian Eq. (3.25), which, after rearrangement, assumes the form,

$$\begin{aligned} H &= CI + \lambda_y v \cos \gamma + \lambda_h v \sin \gamma - \frac{1}{2m} \lambda_v \rho S v^2 C_{D,0} - \lambda_v g \sin \gamma - \frac{1}{v} \lambda_\gamma g \cos \gamma \\ &\quad + \left( \frac{v}{\eta U} + \frac{\lambda_v}{m} - \frac{\lambda_\theta v}{Q \eta U} \right) T - \frac{1}{2m} \lambda_v \rho S v^2 K C_L^2 + \frac{1}{2mv} \lambda_\gamma \rho S v^2 C_L, \end{aligned} \quad (3.27)$$

the Hamiltonian is a linear function of the thrust force  $T$  and a quadratic function of the lift coefficient  $C_L$ . Furthermore, these two control inputs are independent of each other; hence the optimal control law for  $T$  follows the structure in Eq. (2.14). The optimal control law for  $C_L$  is derived by taking the first-order derivative of  $H$  with respect to  $C_L$ . Thereby,

$$-\lambda_v K v C_L + \frac{1}{2} \lambda_\gamma = 0, \quad (3.28)$$

is the necessary optimality condition for  $C_L$ .

### 3.4 Numerical results

This section presents the numerical results obtained from a commercial solver Tomlab [45] for optimal control problems formulated in §3.2. Tomlab contains an optimal control problem solver; this solver guarantees that the output solution satisfies the minimum principle (necessary conditions for optimality). The aims are to verify the theoretical necessary conditions and to provide further analyses for different flight conditions.

#### 3.4.1 Constant altitude cruise phase with the ideal battery model

We first examine the optimal trajectory with the ideal battery model for the constant altitude cruise phase. The aircraft model chosen for our investigation is the Eviation Alice, and the optimal control problem is given in Problem 1. The nominal voltage of the battery pack is assumed to be a constant value of 360V. The constraints for states and control input are estimated as

$$0 \leq y \leq 800 \text{ km}, \quad (3.29a)$$

$$70 \text{ m/s} \leq v \leq 175 \text{ m/s}, \quad (3.29b)$$

$$3kN \leq T \leq 7.5kN, \quad (3.29c)$$

$$0 \leq C_L \leq 1.17. \quad (3.29d)$$

The following flight conditions are considered:  $h = 3$  km,  $y(0) = 0$ ,  $y(t_f) = 200$  km. The initial mass is set to equal the maximum take-off mass of Eviation Alice, which is 6350 kg. Numerical results obtained from Tomlab are presented in Fig. 3.1 and Fig. 3.2. In this case, the initial velocity is not specified, and the optimal solution indicates that the initial velocity should be set as the maximum value. From Fig. 3.2a, it can be observed that the optimal control structure exhibits a min-singular-min structure with two switches, and the junction points are located around 5.5 minutes and 29 minutes.

The optimal necessary condition for the velocity on the singular arc is Eq.(3.24):  $D_v \cdot v^2 = CI \cdot \eta \cdot U$ ; in this numerical case,  $CI = 50$ , the efficiency of the propulsion system is set as  $\eta = 0.7$ .

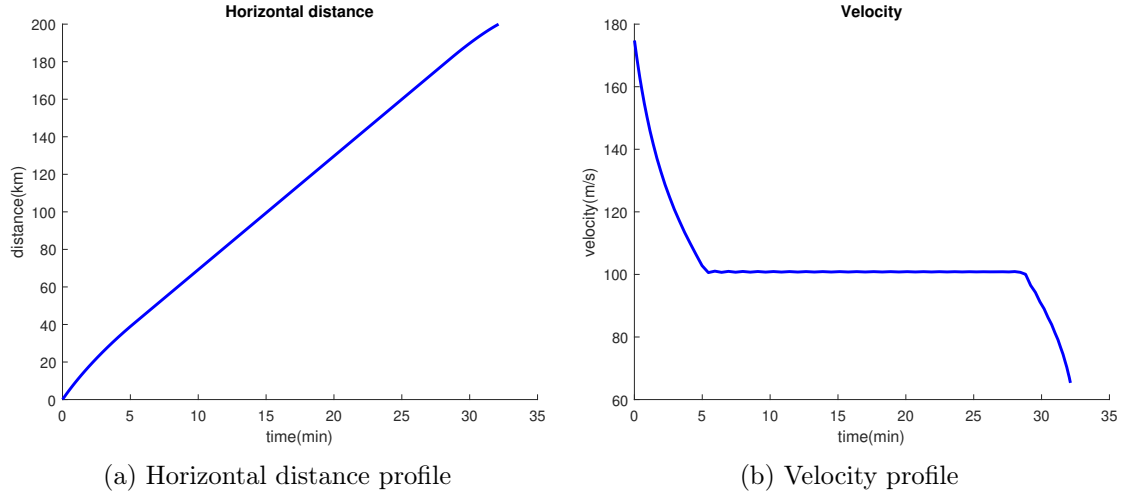


Figure 3.1: The numerical results of states with ideal battery model.

Combining Eq.(3.24) and Eq.(3.21), we obtain the following relation,

$$\rho S C_{D,0} v^3 + \frac{4K W^2}{\rho S v} = CI\eta U, \quad (3.30)$$

by substituting all parameters and numerical results, the velocity obtained from Tomlab satisfies Eq.(3.30).

### *Comparison with Kaptsov and Rodrigues's results*

In Kaptsov’s work [24], the focus was on optimal control for an electric aircraft under the assumption of constant altitude and constant velocity, and of that, the battery model did not have any dynamics. However, this constant velocity assumption limited the ability to introduce additional states to the system, making it challenging to consider battery dynamics and other perturbations in line with previous works in the literature. In this paper, we have adopted a different control input while retaining the same objective function. Consequently, we can observe variations in the total cost and terminal time, as shown in Table 3.1, when compared to Kaptsov’s results.

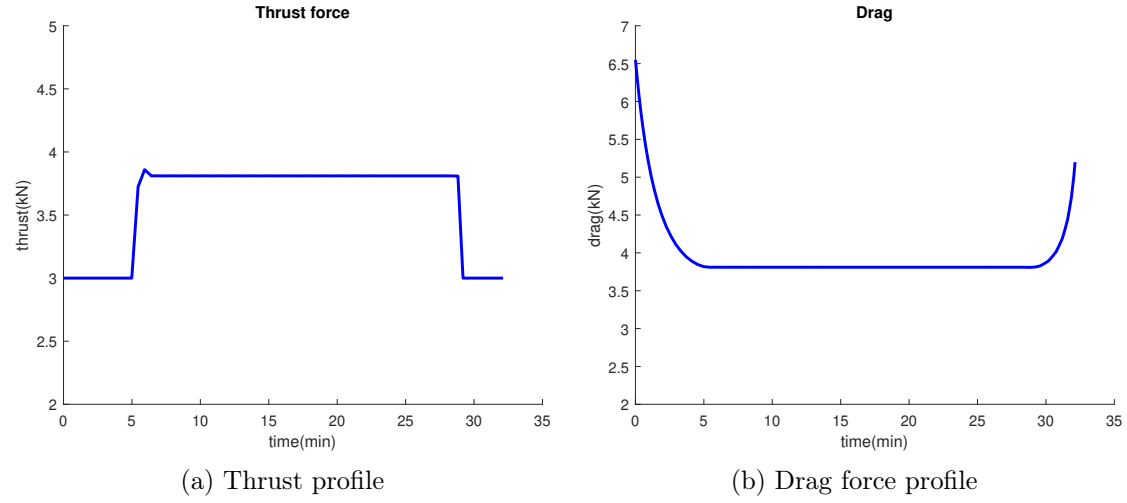


Figure 3.2: The numerical results of control input and corresponding drag force with ideal battery model.

Table 3.1: Comparison of the total cost (Ah) and terminal time (minutes) with Kaptsov and Rodrigues's (K/R) results.

Cost index value	50	100	150	200	250	300
Total cost with K/R	762.45	790.13	817.55	844.73	871.66	898.37
Total cost in this paper	716.11	742.98	769.67	796.19	822.53	848.71
Final time with K/R	33.37	33.05	32.75	32.47	32.18	31.91
Final time in this paper	32.35	32.14	31.92	31.72	31.51	31.32

This table demonstrates an improvement of approximately 50 Ah in the total cost with the method proposed in this paper, accompanied by a slightly shorter terminal time to conclude the flight. As indicated in Fig. 3.1b, the optimal solution involves setting the initial speed to its maximum value. However, this may incur higher energy costs due to the acceleration required to reach the maximum speed. By setting the initial velocity to  $v(t_0) = 130$  m/s, equivalent to Alice's official cruise speed, the total cost increases 814 Ah ( $CI = 200$ ). Compared with the result in Table 3.1, there is an improvement of approximately 30 Ah compared to Kaptsov's result.

Taking the thrust force as control input not only improves the energy efficiency of the flight but also facilitates means of incorporating the dynamics of the battery pack into the optimal control

problem. This approach represents a more comprehensive and practical method for optimizing electric aircraft flights.

### 3.4.2 Constant altitude cruise phase with ECM

Since  $U_{oc,cell}$  is an eighth-order polynomial of  $SOC$ , see Eq.(2.6b), making it difficult to obtain the analytical solution for the problem Eqs.(2), we only provide the numerical results for this problem. Fig. 3.3 to Fig. 3.5 present the numerical solution obtained from Tomlab. It is observed that the optimal control structure shares similarities with the optimal control problem using the ideal battery model. However, due to the utilization of different battery models, there are variations in junction times, final times, and total costs. As a result, the numerical approach provides valuable insights into the performance and behavior of the electric aircraft under consideration with the ECM battery model. The flight and boundary conditions remain consistent with those described in §3.4.1. The

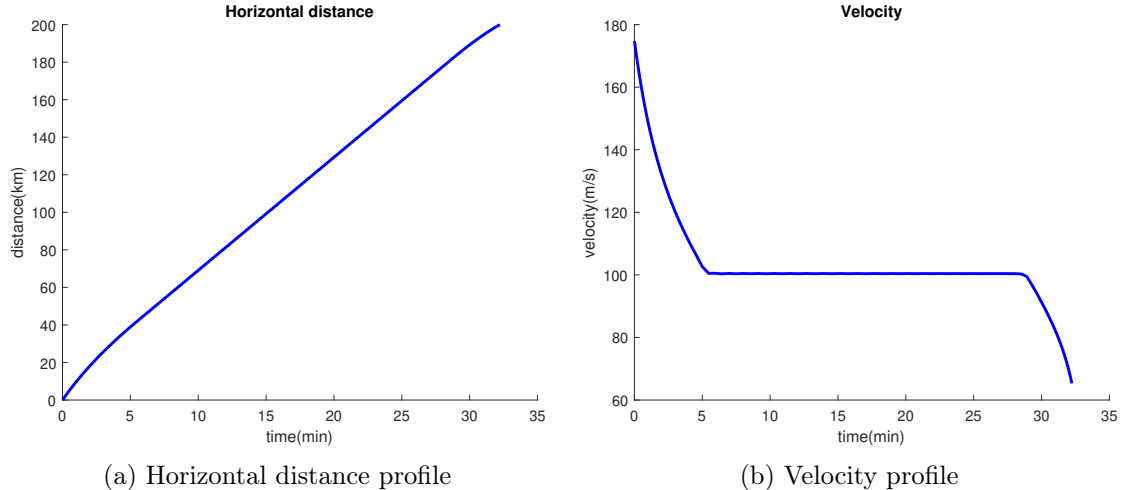


Figure 3.3: The numerical results of optimal states with ECM.

comparison of total cost and terminal time is presented in Table 3.2.

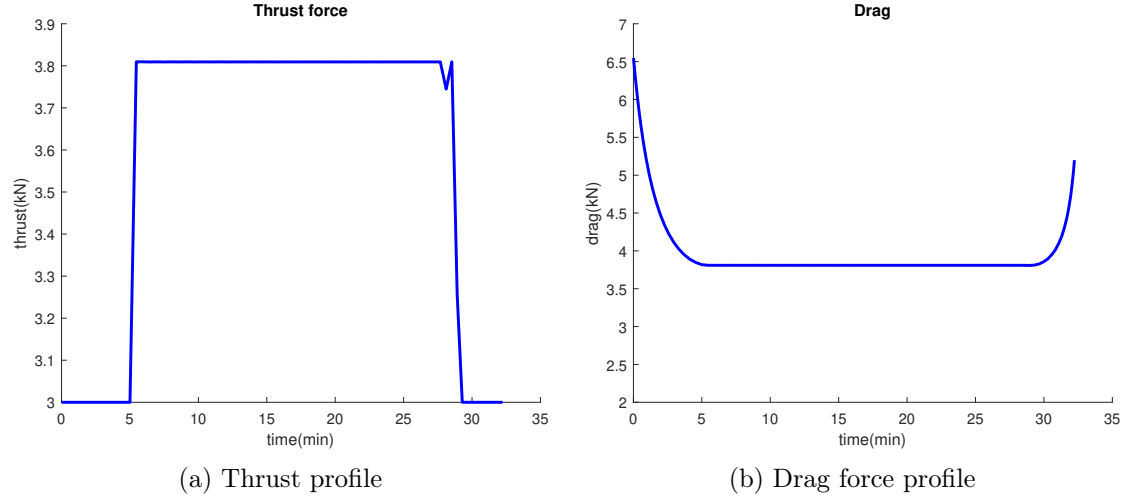


Figure 3.4: The numerical results of optimal control input and corresponding drag force with ECM.

Table 3.2: Comparison of total cost and time between two battery models.

	Total cost ( $A \cdot h$ )	Terminal time (min)
Ideal battery model	742.98	32.14
ECM	708.96	32.40

The cost minimized in this section consists of two components: the total charge drawn from the battery pack and the time-related cost. As different battery models produce varying output voltages, the total costs obtained from the two battery models differ while the power required to fly the aircraft remains the same. Since the ECM offers higher fidelity than the ideal battery model, it can be inferred that the total cost estimate with ECM is more accurate and realistic.

By adopting thrust as the control input in the optimal control problem formulation, the trajectory optimization procedure becomes adaptive, allowing the incorporation of various disturbances into consideration. For example, this formulation can be applied to the complete flight profile of an electric aircraft and accommodate uncertainties like wind and other meteorological factors. The adaptive nature of this control approach enhances the aircraft's ability to adapt to changing conditions and disturbances, thereby improving its overall performance and robustness.

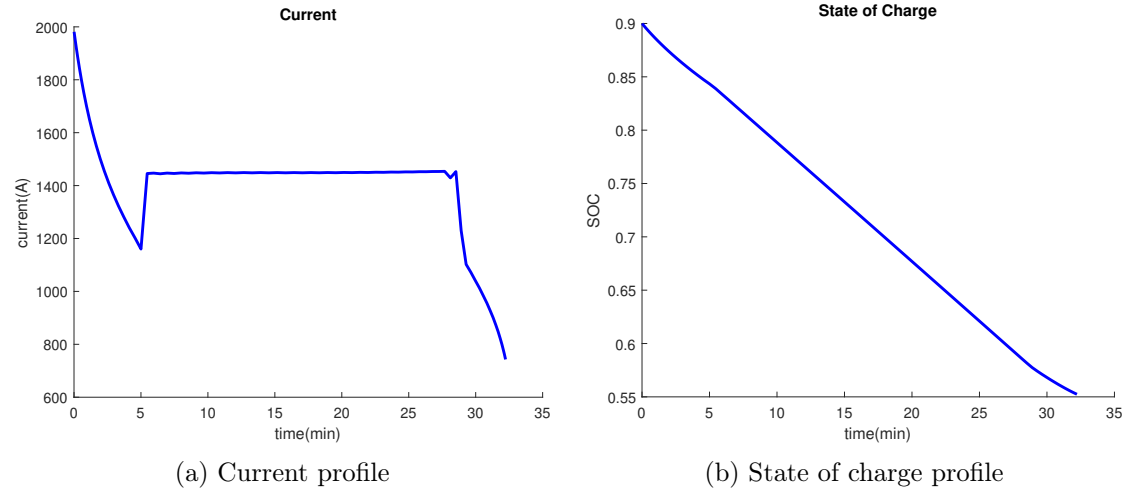


Figure 3.5: The numerical results of battery states with ECM.

### *Impact of initial velocity*

In the previous examples, the initial velocity is not specified. However, the initial velocity plays a significant role in determining the optimal flight trajectory and, consequently, affects the total cost and terminal time in the examples discussed. From Fig. 3.6, it is observed that a higher initial

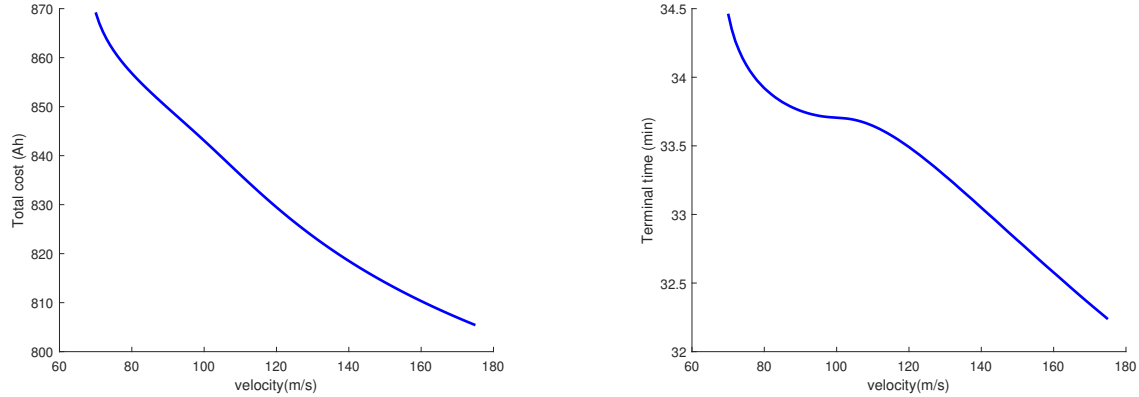


Figure 3.6: The impact of initial velocity on the total cost and terminal time.

velocity leads to less cost and a shorter duration for the cruise phase. As such, when we start from the maximum value of the velocity, we could have the least incurred cost and flight time.

However, when the initial velocity is set to the maximum value, it allows the aircraft to reach the desired cruise speed faster, but this may come at the cost of higher energy consumption due to the required acceleration. Ultimately, the selection of the initial velocity should be carefully considered in conjunction with other parameters and objectives to achieve the most appropriate and optimal flight plan for the given electric aircraft mission.

#### *Impact of the battery pack configuration*

The Eq.(3.24) indicates that the optimal velocity on the singular arc depends on the cost index, total system efficiency, and the voltage of the battery pack. To further investigate, we will now delve into the implications of different battery configurations on the overall cost.

In the previous numerical examples, the voltage of the battery pack was assumed to be  $360V$ , and the configuration followed 31 parallel paths with 100 cells connected in series in each path (referred to as case 2). Now we consider two additional cases with the same number of battery cells in the pack:

1. case 1: This configuration consists of 39 parallel paths with 80 cells in each path (20 more cells than the original configuration), resulting in a nominal voltage of  $288V$ ;
2. case 3: This configuration consists of 25 parallel paths with 124 cells in each path; the nominal voltage is  $446.4V$ ;

We then solve the corresponding optimal control problem with ECM and compare the total cost and the terminal time. The flight distance is set as  $200km$ , the initial velocity as  $130km/s$ , and the cost index is set as 100; for the maximum range problem, the total mass we take is the maximum take-off weight. The comparative results are given in Table 3.3:

Table 3.3: Comparison of cost and time between different battery configurations

	case 1	case2	case 3
Total cost (Ah)	1025.58	826.92	675.30
Terminal time (min)	33.56	33.43	33.30
Maximum range (km)	335.43	335.23	336.38

As the nominal voltage increases in the battery pack (as observed in case 3 with a voltage of  $446.4V$ ), the total incurred cost for the flight reduces without compromising the maximum range. This insight provides a clear direction for the desired configuration of the battery pack.

### 3.4.3 Accelerated climb phase with ideal battery model

For the accelerated climb phase of Eviation Alice, the nominal voltage of the battery pack is assumed to be 360V. Constraints for control inputs and for the states  $y$  and  $v$  are the same as for the cruise phase; for other states, they are given as,

$$0 \leq h \leq 3500 \text{ m}, \quad -6 \leq \gamma \leq 6 \text{ deg}, \quad 0.1 \leq \theta \leq 1. \quad (3.31)$$

The initial values for the states are set as follows:  $y(t_0) = 0, h(t_0) = 0, v(t_0) = 80 \text{ m/s}, \gamma(t_0) = 0 \text{ deg}$ , and  $\theta(t_0) = 1$ . The terminal condition for the altitude is specified as  $h(t_f) = 3 \text{ km}$ . Moreover, no terminal conditions are set for the other states. The numerical results obtained from Tomlab for the Problem 3 are presented in Fig. 3.7 to Fig. 3.10.

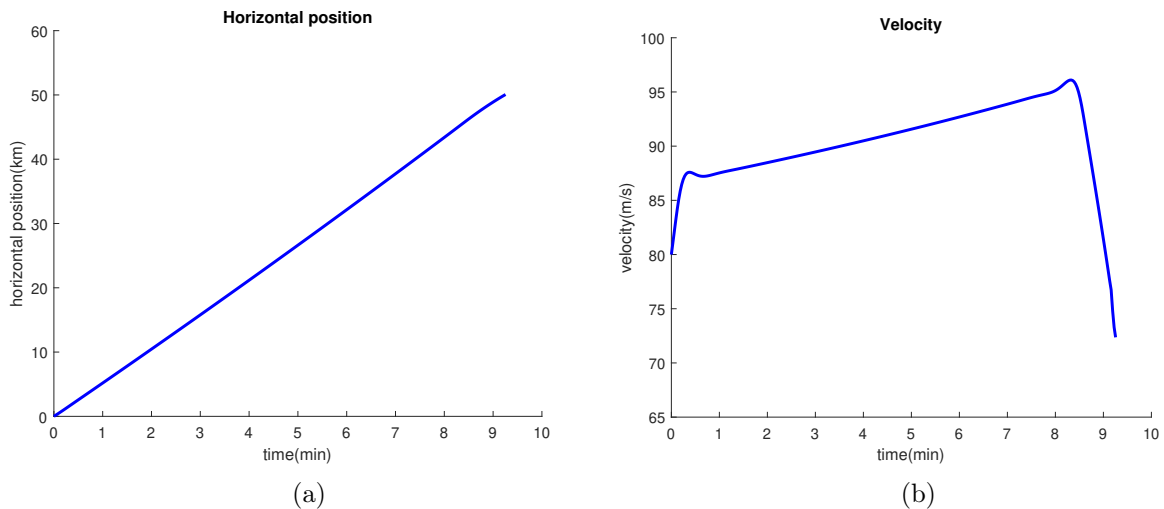


Figure 3.7: Climb phase; (a)Horizontal distance profile; (b)Velocity (only magnitude) profile.

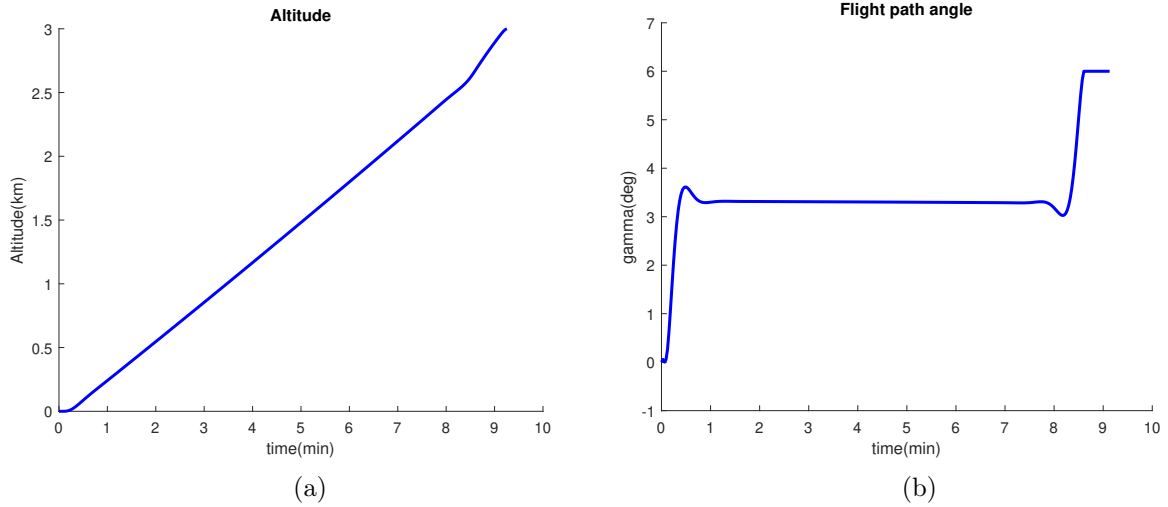


Figure 3.8: Climb phase; (a) Altitude profile; (b) Flight path angle profile.

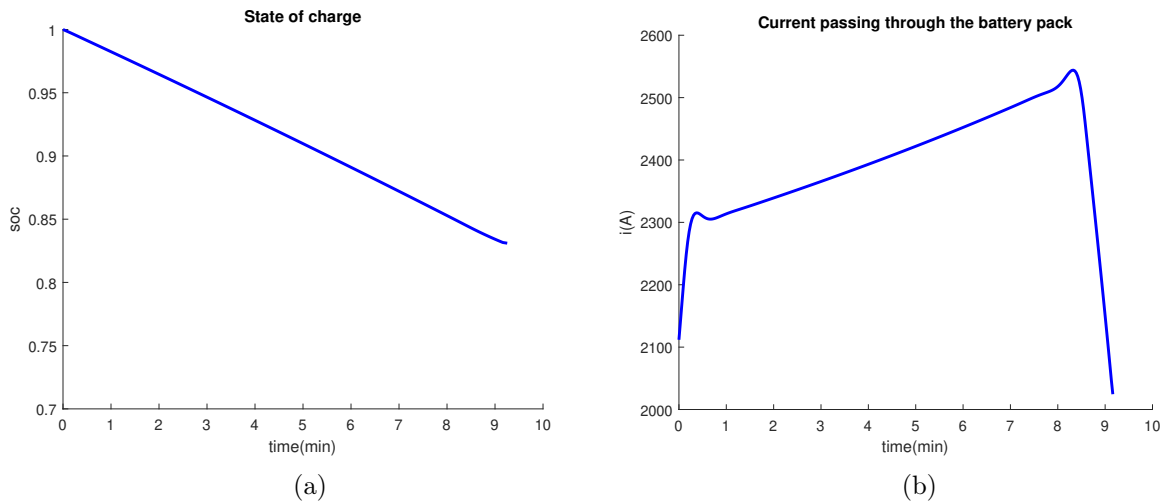


Figure 3.9: Climb phase; (a) SOC of the battery pack profile; (b) The current passing through the battery pack.

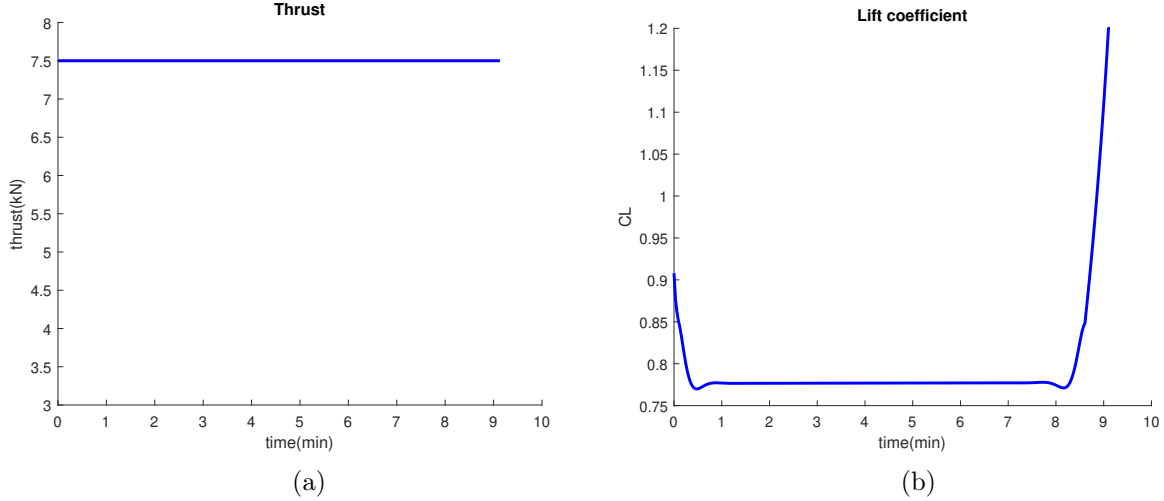


Figure 3.10: Climb phase; (a) Thrust force profile; (b) Lift coefficient profile.

Fig. 3.10 indicates that during the climb phase, the optimal control solution involves adopting maximum thrust force while allowing variations in the lift coefficient. The corresponding total cost is 368Ah, and the terminal time is 555s. The co-states obtained from Tomlab satisfy the necessary condition for optimality, as given in Eq.(3.28).

Fig. 3.7b and Fig. 3.9b depict a steep change in the velocity profile and the current profile during the flight. Such abrupt variations may lead to passengers' discomfort and have an adverse effect on the battery pack. To mitigate this issue and prevent sudden fluctuations in the current profile, we introduce one more constraint on the states, namely,  $-0.1 \leq \dot{v} \leq 0.1$ .

The corresponding velocity profile and current profile, subject to this constraint, are shown in Fig. 3.11. After implementing this constraint, the total cost and the terminal time are 375Ah and 576s, respectively. The total cost exhibits only a slight change, while the climb interval extends by 21s. This constraint proves to be effective in achieving a smoother velocity and current profile, minimizing the discomfort experienced by passengers and reducing the adverse impact on the battery pack.

We now replace the ideal battery model in Problem 3 with ECM to investigate the impact of different battery models on the total cost and the terminal time. It is noteworthy that the states and control inputs obtained with ECM are essentially the same as those obtained with the ideal

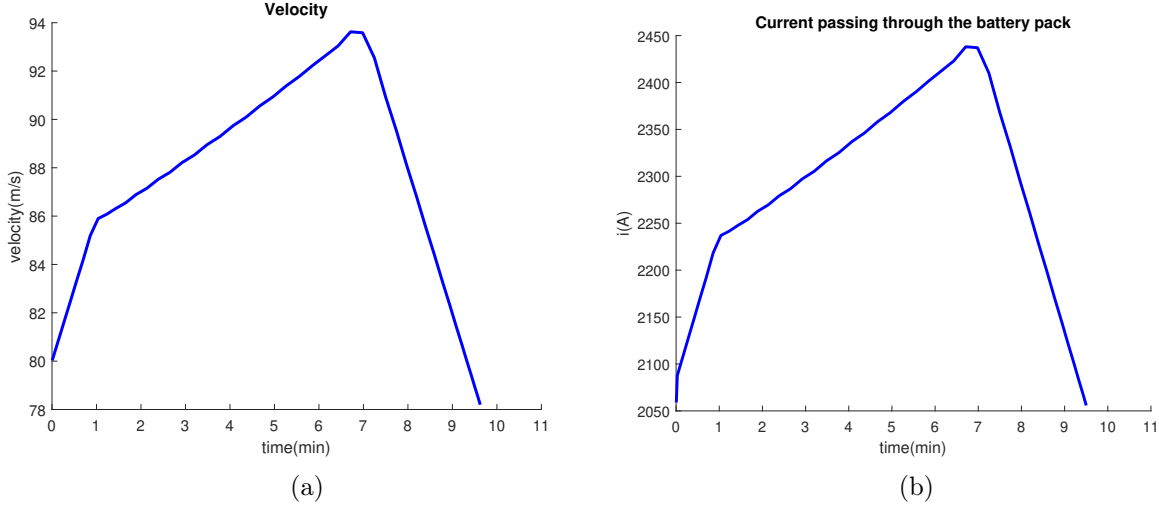


Figure 3.11: Climb phase with an extra constraint; (a) Thrust force profile; (b) Current profile.

battery model. However, the total cost for the ECM case is 339Ah, which is lower than the cost obtained from ideal battery model due to a higher voltage profile associated with ECM.

To verify the optimality of this algorithm, the fuel consumption for the climb phase with constant velocity and constant flight path angle is computed. We sweep the velocity from 70 m/s to 90 m/s, and  $\gamma$  from 0 to 6 deg to find the minimum cost; the results show that with  $v = 89$  m/s and  $\gamma = 3.4$  deg, the total climb cost is 374 Ah, and the terminal time is 574 s. Compared to the proposed algorithm, this constant climb has slightly more operating costs and longer flight time. In addition, increasing the velocity to  $v = 89$  m/s also requires additional time and battery charge. Note that in order to maintain the constant velocity and flight path angle, the thrust force and the lift coefficient are changing at all times. In the proposed algorithm, the thrust force and the lift coefficient are constant for most of the flight.

#### 3.4.4 A complete flight phase

In previous examples, we have solved the AEA energy management using the optimal control formalism in order to minimize DOC during the climb and the cruise phases, respectively. Both problems are free-end optimal control problems, meaning that the final time for the trajectory is not specified. In addition, neither terminal conditions on the aircraft speed nor on the state of charge

of the battery pack have been addressed.

In this section, a multi-phase energy management problem is formalized and then solved as a single optimal control problem. Note that in each phase of the trajectory, objective functions and dynamics may vary. As a result, the complete aircraft flight trajectory has characteristics of a *controlled switched dynamical system*. In this work, we focus on the climb, cruise, and descent phases of the flight and leave take-off and landing phases for our future work.

The integrated optimal control problem is constructed as,

**Problem 4.**

$$J^* = \min_{T, C_L} \int_{t_0}^{t_1} (CI_1 + I(t))dt + \int_{t_1}^{t_2} (CI_2 + I(t))dt + \int_{t_2}^{t_3} (CI_3 + I(t))dt \quad (3.32a)$$

$$\text{s.t. } \dot{x}_k = f_k(x_k, u_k, t), \quad k = 1, 2, 3 \quad (3.32b)$$

$$x_k \in \mathcal{X}_k, \quad (3.32c)$$

$$u_k \in \mathcal{U}_k, \quad (3.32d)$$

with state  $x_k = [y \ h \ v \ \gamma \ \theta]^\top$  and control  $u_k = [T \ C_L]^\top$ ;  $\mathcal{X}_k$  and  $\mathcal{U}_k$  designate state and control constraint sets for each phase, respectively.

For the climb and the descent phase, box constraints for all states and the lift force are the same as Eqs.(3.31) and Eq.(4.22); the thrust constraint during the descent phase is  $0.3 \leq T \leq 7.5$  kN. For the cruise phase, both the altitude and the flight path angle are constant, namely,  $h \equiv 3000$  m and  $\gamma \equiv 0$  deg; other constraints for the states and the control inputs are the same as the climb phase.

The dynamics in each phase is given as follows:

**Cruise phase (k=2):**

$$\dot{v} = \frac{T - D}{m} \quad (3.33a)$$

$$\dot{y} = v \quad (3.33b)$$

$$\dot{\theta} = -\frac{I}{Q} = -\frac{U_{oc} - \sqrt{U_{oc}^2 - 4P_{bat}R}}{2RQ} \quad (3.33c)$$

$$L = W, \quad h = 3000\text{m} \quad (3.33d)$$

Climb and descent phases ( $k=1,3$ ):

$$\dot{v} = \frac{T - D - W \sin \gamma}{m} \quad (3.34a)$$

$$\dot{\gamma} = \frac{L - W \cos \gamma}{mv} \quad (3.34b)$$

$$\dot{h} = v \sin \gamma \quad (3.34c)$$

$$\dot{y} = v \cos \gamma \quad (3.34d)$$

$$\dot{\theta} = -\frac{I}{Q} = -\frac{U_{oc} - \sqrt{U_{oc}^2 - 4P_{bat}R}}{2RQ}. \quad (3.34e)$$

This integrated problem is more involved than previous instances of optimal control examined in this paper as we do not know the values of  $t_1$ ,  $t_2$ , and  $t_3$ . In addition, the boundary conditions for the variables  $v$  and  $\theta$  for each phase are unknown. To address these issues, a new independent variable is introduced, and the problem is reformulated accordingly [46].

The main idea behind the proposed approach is to make the unknown switching times part of the dynamic states; this is facilitated by introducing a new independent variable  $\tau$  with respect to which the switching times are parameterized. Hence, there is a linear relationship between the new variable and the original time variable, and the slope of this linear relation changes at each interval during the switches/transitions. In this direction, it is assumed that there are  $N = 2$  switches ( $N + 1 = 3$  time intervals); then the relation between  $\tau$  and  $t$  is given as

$$t = \begin{cases} (N+1)ts_1\tau, & \text{if } 0 \leq \tau \leq \frac{1}{N+1}; \\ (N+1)(ts_{i+1} - ts_i)\tau + (i+1)ts_i - its_{i+1}, & \text{if } \frac{i}{N+1} \leq \tau \leq \frac{i+1}{N+1}, \end{cases} \quad (3.35)$$

where  $ts_i$  is the  $i$ -th switching time; note that these are the additional variables with respect to our original problem.

Accordingly, the dynamics of the system with respect to  $\tau$  is,

$$\frac{d\mathbf{x}}{d\tau} = (N+1)(ts_{i+1} - ts_i)f_i(\mathbf{x}, u, t(\tau)), \quad (3.36)$$

and the objective function assumes the form,

$$\hat{L}(\hat{\mathbf{x}}, u, \tau) = (N + 1)(ts_{i+1} - ts_i)L(\mathbf{x}, u, t(\tau)), \quad (3.37)$$

where  $\hat{\mathbf{x}} = [\mathbf{x}, ts_1, \dots, ts_N]$  is the extended state.

Applying this strategy to the multi-phase DOC minimization for AEA, we have  $N = 2$  with three extra states in our dynamical model. Subsequently, we implement this method in Tomlab and obtain the numerical results as shown in Figs. 3.13 and 3.15. For the climb phase, the initial and terminal conditions are the same as in the previous section. Then, for the cruise and descent phases of the flight, all states except for the flight path angle are set to be continuous (assuming that there can be a steep change in the flight path angle); the terminal condition for the cruise phase is when the horizontal position reaches 300km. Finally, for the descent phase, the terminal conditions are consistent with altitude decreasing to zero and the horizontal flight distance of 57km (approximately satisfying the “Rule of three”).

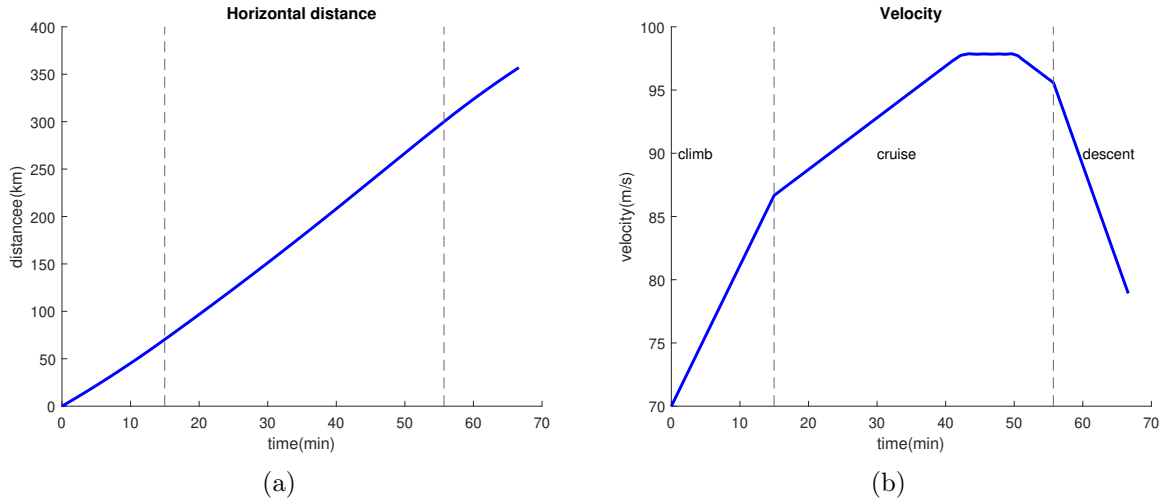


Figure 3.12: A complete flight phase; (a) Horizontal distance; (b) Velocity (magnitude).

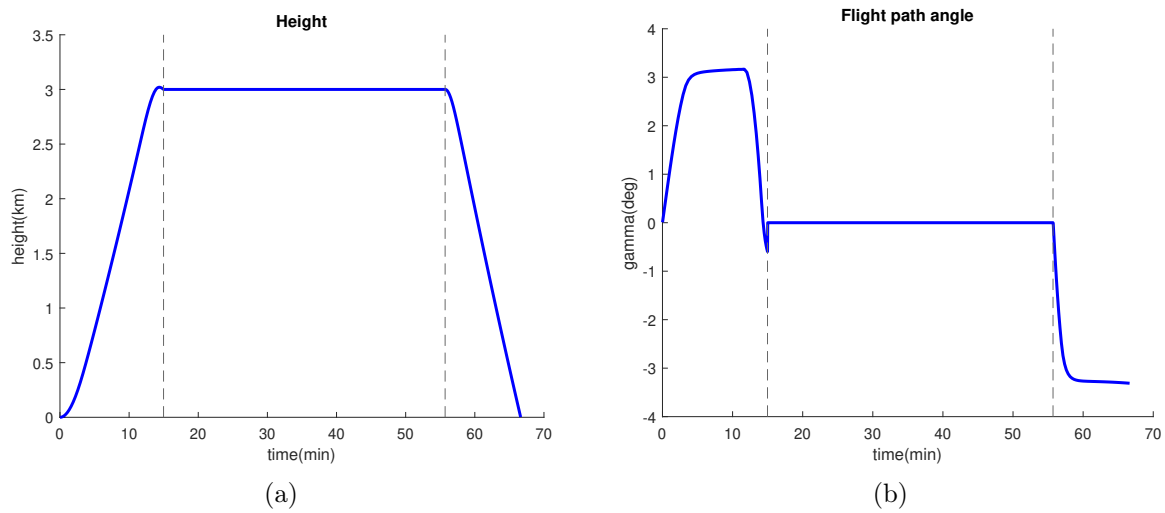


Figure 3.13: A complete flight phase; (a) Altitude; (b) Flight path angle.

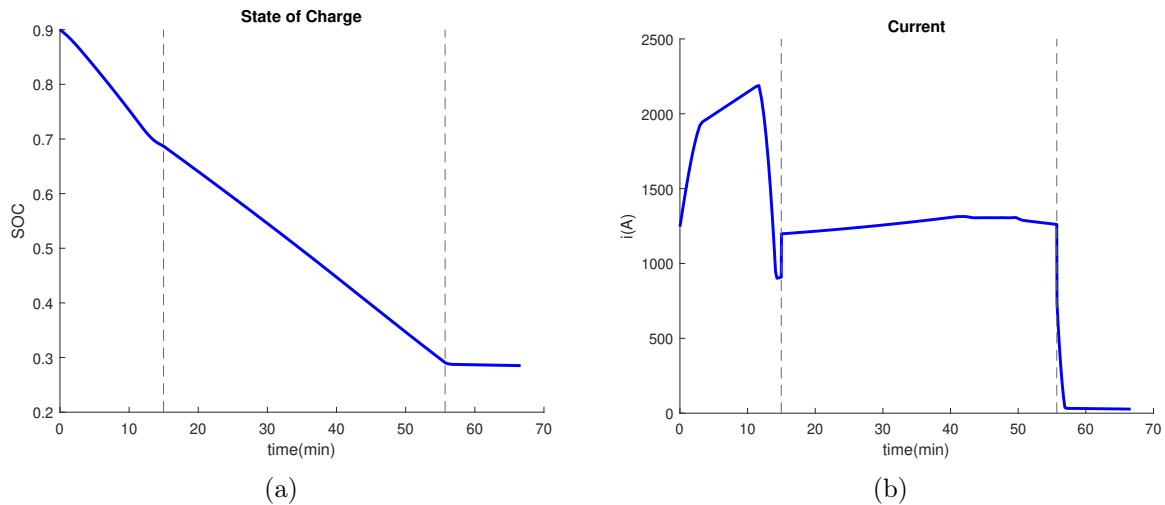


Figure 3.14: A complete flight phase; (a) State of charge; (b) Current.

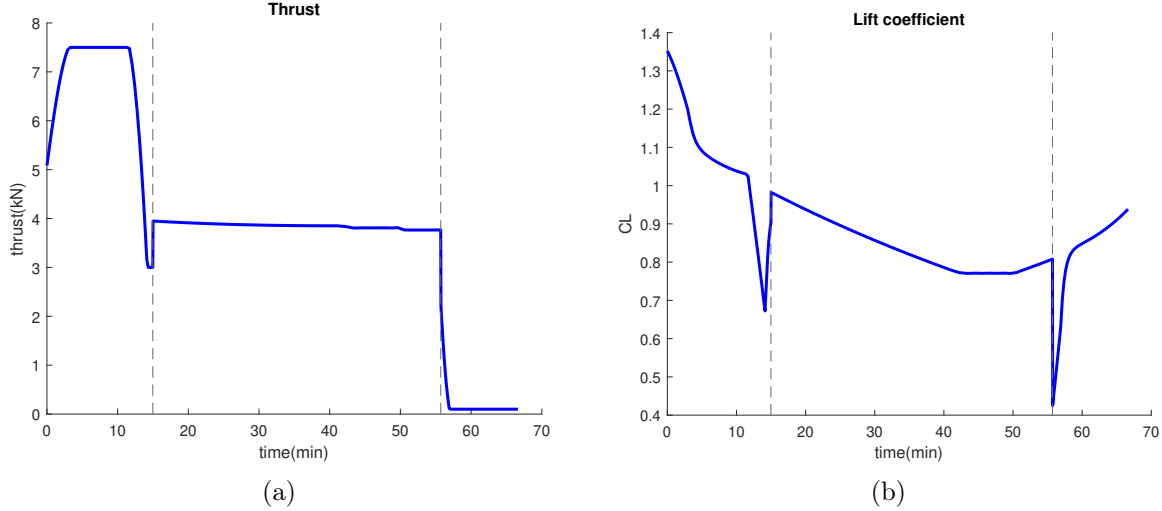


Figure 3.15: A complete flight phase; (a) Thrust; (b) Lift coefficient.

Examining Fig. 3.13 to Fig. 3.15 and comparing them with results obtained in [3] and the previous section, we note that for the climb phase, the velocity and flight path angle profiles are different from the results of the single-phase optimization approach. In the current setup, the velocity profile is monotonically increasing, and the flight path angle decreases to zero at the end of the climb phase. Correspondingly, the thrust profile is no longer constant during the climb phase, and the lift coefficient profile needs to decrease to about 0.6 at the end of the climb phase. During the cruise phase, we still have a similar control structure and state profiles analogous to the single optimization approach. However, the thrust variation is smaller than that for the single optimization case. For the descent phase, we also have a similar control structure and state profiles as compared with the single optimization approach.

### 3.5 Simulink model with different battery blocks

In this section, we present the Simulink model developed in conjunction with the proposed modeling and control approach for AEA energy management, as depicted in Fig. 3.16.

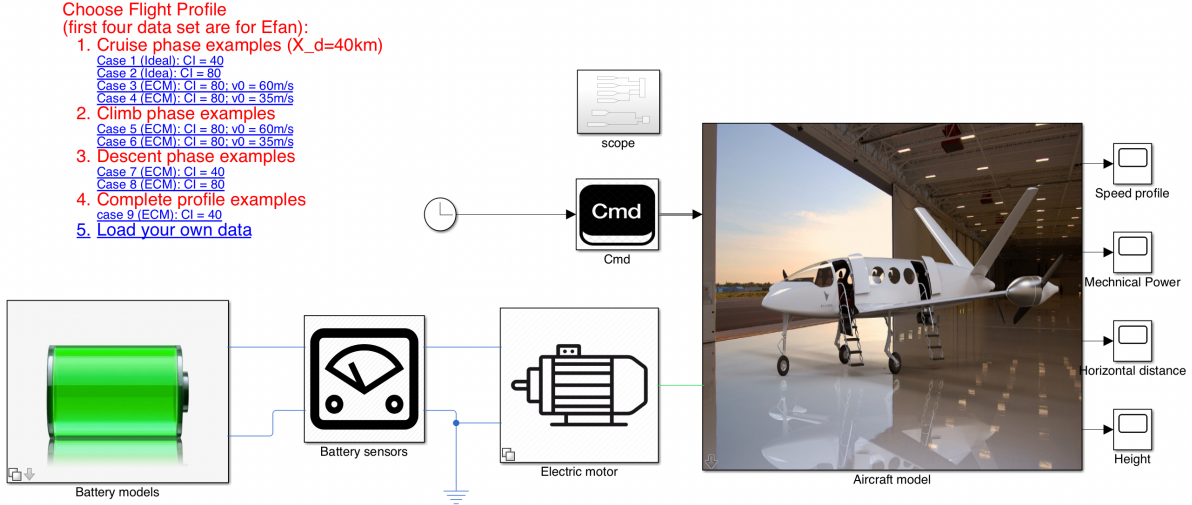


Figure 3.16: AEA Simulink Model.

This model is designed to be configurable, allowing the demonstration and validation of various facets of AEA energy management. For example, the battery subsystem is implemented as an interchangeable “variant subsystem”, which enables the selection of multiple battery models prior to simulation. Three battery models with different fidelities are available to explore the impact of flight dynamics on the battery pack. The corresponding optimal solutions are obtained from Tomlab and treated as tab signals to generate the command signals in the Simulink model. The primary blocks in the Simulink model are described in the following,

- **Battery models:** This variant subsystem contains three battery models: the ideal battery model, the ECM, and the SPM. The ideal battery model is a simple battery block from the Simulink Library Browser with minimal internal resistance (the model cannot be run with zero internal resistance) and no dynamics. The ECM is a Matlab function representing the relation between open circuit potential and the SOC of the battery; the input of this function is the SOC of the battery pack. The SPM, on the other hand, involves ODEs and Differential Algebraic Equations (DAEs); we utilize Matlab “ode15s” to solve the corresponding ODEs and DAEs at every second and take one of the states (open circuit potential) as the output of this block. The input of this block is the current passing through the battery.

- **Battery sensors:** This block observes the voltage and current of the battery while also computing the SOC of the battery (by integrating the current and then dividing the total charge of the battery) as well as the total operating cost. Note that the method utilized for computing the SOC of the battery is an idealization; SOC measurements are, in general, more challenging.
- **DC-DC Converter and Electric Motor:** These are standard devices from the Simulink Library Browser. The Motor block includes specific components for computing the power load and the torque load.
- **Cmd:** This block generates command signals for the aircraft, including the thrust force, lift coefficient, and flight path angle. The optimal solution obtained from Tomlab is used as tab data; then, interpolation with the time signal is applied to compute the command signals. A larger amount of tab data from the Tomlab results in more accurate command signals.
- **Aircraft Model:** Three aircraft models with different configurations are implemented: E-fan 1.0, a two-seat aircraft, and Eviation Alice. The second model provides means of including customized data for an aircraft. This block takes the command signals from “Cmd” block and propagates values of aircraft speed, horizontal distance, and altitude.

Table 3.4: Comparison of total costs with three distinct battery models.

Battery model	Total cost
Ideal	738.1
ECM	690.9
SPM	675.8

We now proceed to implement the optimal trajectories obtained from Tomlab on the Simulink model. Here we present the results for the cruise phase with the same flight conditions as in Table 3.2.

By examining Fig. 3.17 and Table 3.4, different battery models lead to variations in battery cell performance and total cost for the flight. For the SPM case, the voltage of the battery pack is

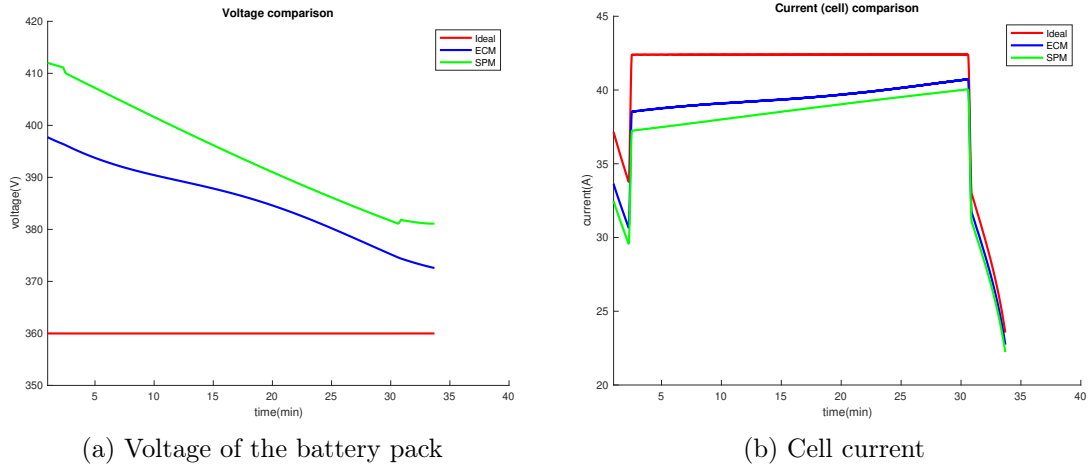


Figure 3.17: Comparisons of voltage and cell current for distinct battery models.

relatively high at the beginning of the discharge phase, resulting in a lower current drawn from the battery compared to the ideal model. In the meantime, SPM facilitates a better estimation of the key states for the battery cells, allowing, for example, monitoring the thermal behavior of the cells during the flight.

## Chapter 4

### **POWER ALLOCATION AND STRUCTURES STUDY FOR HYBRID-ELECTRIC AIRCRAFT**

The urgent need to mitigate aviation's environmental impacts and reduce dependence on fossil fuels, coupled with the current limited range of All-Electric Aircraft, has spurred the development of Hybrid Electric Aircraft. These innovative aircraft combine conventional gas engines with electric propulsion systems, presenting the potential for improved efficiency and reduced environmental impacts. However, the integration of a conventional propulsion path and an electric propulsion path poses a new challenge: how to allocate power optimally between these two sources to obtain optimal performance.

To address this challenge, leveraging the well-developed power allocation algorithms from ground Hybrid Electric Vehicles (HEVs) can significantly benefit the advancement of HEA algorithms. Ground HEVs have undergone extensive development over the past decades [47, 48, 49, 50, 51, 52, 53], resulting in robust power allocation algorithms in both research and industry. By utilizing this wealth of knowledge, the development of algorithms for aircraft can greatly benefit and progress.

In the case of ground HEVs, an energy management system plays a crucial role in controlling and coordinating power generation, energy storage, and power flow within subsystems to optimize overall system efficiency [54]. The purpose of the energy management system is to ensure that power is allocated and utilized in the most efficient way. Similarly, an efficient energy management system is vital to HEA. However, several key characteristics of aircraft need careful attention before borrowing experiences from HEV to HEA:

1. Operational Challenges. The demanding operational conditions encountered by aircraft, characterized by factors such as extremely low temperatures, intricate aerodynamics, and unpredictable weather patterns, pose unique challenges and requirements for the energy management systems of HEA. The power allocation algorithm must exhibit adaptability across diverse operating conditions to ensure efficient and reliable performance.

2. Weight sensitivity. Ground HEVs focus primarily on efficient propulsion for driving on roads, while the aircraft's propulsion system requires sufficient power for both propulsion and providing enough lift force to maintain flight. Consequently, HEA is very sensitive to weight; certain structures suitable for ground vehicles may not be a good option for aircraft;
3. Types of engines. Ground vehicles usually use an internal combustion engine (ICE), while aircraft employ different types of gas engines based on their size and flight missions, introducing additional complexity in designing the energy management system for HEA. Each engine type has unique operational characteristics, efficiency profiles, and power delivery capabilities, requiring specific power allocation strategies to optimize performance.

Despite these differences, there is still great potential to learn from ground HEVs and adapt their power allocation algorithms to the unique needs of HEA. The purpose of power allocation can be multifaceted. The energy consumption, which includes the burning of fuel and consumption of the battery charge, the amount of emissions produced while in flight, the rate at which the battery degrades, and the amount of noise, can all be factored into the objective function. For designing the energy management system for HEA in this dissertation, we only focus on fuel consumption minimization, which will indirectly result in fewer emissions. The basic assumption is that the flight profile for HEA is predetermined, and the power request is known in advance. The proposed algorithms aim to efficiently allocate the available power resources from the engines and the electric motors.

When developing the power allocation algorithm in this chapter, it is assumed that the propulsion system has a parallel structure, wherein the engines and the electric motors are able to drive the aircraft both individually or together. For ground HEVs, there are three most commonly used configurations: *a)* the series, *b)* the parallel, and *c)* the series-parallel (power-split). In the series configuration, the engine is used for driving a generator to power the electric motor when the battery does not have enough power. The power split configuration combines the series configuration and the parallel configuration together. In all of these configurations, there is a mechanical connection between the ICE and the electric motor; hence, the battery can be charged through regenerative braking and by the ICE.

Existing literature on hybrid architectures for aircraft propulsion [55, 56, 57, 58] mostly borrows principles from ground HEVs, often assuming that the gas turbines and the electric motors should be connected mechanically, allowing the turbine to charge the battery during flight. This connective mechanism has several potential benefits: (a) the engine can run in its most fuel-efficient region by utilizing the electric motor as an extra load to conserve fuel, and (b) the electric motor can operate in “one-engine-inoperative” (OEI) mode after the climb phase assuming the battery has sufficient capacity to support the aircraft landing safely. These benefits are compatible with series, parallel, and series-parallel configurations. On the other hand, MagniX—a manufacturer of electric propulsion systems for electric aircraft—proposed a novel parallel hybrid structure in 2021 in which the engine and electrical paths are independent (without a mechanical connection in place). In this configuration, the electric motor and the engine work together during the climb phase, while the engine is responsible for the cruise and descent phases. In addition, one can bypass the use of the engine and transition the HEA to an AEA—when the energy density of the battery reaches the desired level. In the automotive industry, this structure is classified as a “Through-the-Road” parallel hybrid electric vehicle [59], and it facilitates the transition from conventional automobiles to hybrid electric vehicles. This dissertation compares these two structures in the context of the aforementioned benefits, and specifically, through the lens of optimal power allocation.

This chapter is organized as follows. First, related work of power allocation for ground HEVS and HEA, and preliminary design for HEA, are provided in §4.1. In §4.2, a detailed power allocation algorithm for HEA is developed and analyzed. In §4.3, two parallel hybrid electric structures are compared in terms of fuel consumption, and numerical examples are provided.

#### **4.1 Related works**

In the context of energy management for ground HEVs, control strategies can be broadly classified as rule-based methods and optimization-based methods [60]. Rule-based strategies depend on modes of operation, where rules are determined based on heuristics, intelligence, or mathematical models, usually without a priori knowledge of a predetermined driving cycle [61]. Rule-based strategies can be divided into two subcategories: deterministic and fuzzy [62, 63, 64] rule-based control strategies. Peng *et al.* [65] developed a rule-based energy management strategy that is calibrated using dynamic programming (DP), optimizing the control actions for each mode.

On the other hand, optimization-based strategies are generally classified as real-time optimization and global optimization. Global optimization includes linear programming [66], DP [67, 68, 69, 70], optimal control theory (the minimum principle) [71, 72], stochastic DP [73], genetic algorithms [74, 75, 76], etc. Real-time optimization includes methods such as equivalent fuel consumption minimization [77, 78], model predictive control [79, 80, 81], reinforcement learning [82, 83, 84, 85], etc.

This dissertation primarily focuses on optimal control theory for HEA. The minimum principle has been widely applied to the energy management of ground HEVs, and numerous strategies have been developed in order to implement the minimum principle in real time. Kim *et al.* [77] applied the minimum principle to a power-split HEV, and optimal control is obtained from the Hamiltonian function. This unique property of this HEV problem, where the co-state corresponding to the battery's State of Charge (SOC) remains constant, allows for easy real-time optimal control implementation. They also compared the results of the minimum principle with DP and demonstrated that the proposed algorithm is globally optimal. Hou *et al.* [86] proposed a piecewise linear approximation to convexify the Hamiltonian function such that the minimum principle-based algorithm can be implemented in real time. The numerical results in a parallel HEV demonstrated a 6.96% reduction in fuel consumption compared to a conventional rule-based strategy, and a significant increase in computational performance.

Regarding power allocation algorithms for HEA, which utilize two energy sources for the propulsion system, several researchers have made significant contributions. Leite and Voskuyl [87] utilized DP to obtain an optimal energy management scheme for HEA for a given flight profile. Doff-Sotta *et al.* [88] developed a convex formulation for HEA energy management and demonstrated that the optimal control strategy significantly reduces fuel consumption compared to heuristic methods. Zhang *et al.* [89] proposed a nonlinear model predictive control-based optimal energy management strategy to minimize fuel consumption during flight. Li *et al.* [90] developed an adaptive power distribution strategy for a fuel cell-electric hybrid aircraft and verified the corresponding algorithms on a prototype electric aircraft. Donateo et al. made important contributions to energy management in different aircraft configurations. In [91], they applied DP for energy management for a lightweight rotorcraft, where the corresponding optimal control was formalized in terms of a shortest path problem on a graph, followed by the application of the Dijkstra algorithm for its solution; in [92], they

applied DP and the Equivalent Consumption Minimization Strategy (ECMS) in a hybrid electric helicopter to obtain the optimal usage of the battery for given flight missions; significant fuel reduction is achieved compared with the conventional turboshaft engine-only aircraft. Furthermore, [92] demonstrated that the fuel savings are the same whether or not the battery pack is charged during flight. Analogous results will be presented for the 19-seat fixed-wing conceptual aircraft in this chapter.

Although a few commercial HEA have been manufactured and are available on the market [12, 13, 10, 15], publicly accessible technical data and characteristics of these aircraft are rather limited. Nevertheless, numerous studies have delved into the design space of HEA, exploring various aspects of their development. Wall and Meyer [93] surveyed the development of simulated and physically realized Hybrid Electric Propulsion (HEP) systems and presented their suggestions on system modeling and control of HEP systems for future research. Zamboni *et al.* [94] proposed a methodology to conceptually model and size the HEP system. They concluded that the choice of HEP system architectures depends on the performance capability of the electric components, in particular of the battery. Finger and Braun [95] studied the parallel hybrid electric propulsion system for four different types of aircraft, including VTOL aircraft, analyzing specific scenarios where HEP proves to be energy-efficient and situations where it might have limited benefits. [96] proposed a methodology to determine the size of aircraft with different propulsion configurations, including hybrid electric and fully electric. De Vries *et al.* [97] also proposed a comprehensive preliminary sizing method for aircraft with different propulsion configurations. In [98], the conceptual design of HEA has been examined. This work introduced the morphologies and architectures of aircraft with HEP systems and proposed sizing methodology and corresponding integrated performance of HEA. The work [99], on the other hand, discussed the range equation for a series HEA. Isikveren *et al.* examined the design of VTOL aircraft [100]. Finger *et al.* compared two design approaches utilizing an existing 19-seat conventional aircraft as the baseline model [18]. One of the conceptual models in the aforementioned work is taken as the aircraft model in this dissertation as described in §2.1.

## **4.2 Power allocation algorithm for HEA**

The power allocation for HEA is formulated as an optimal control problem under the following assumption.

**Assumption 5.** *The flight profile is predetermined, and the velocity is assumed to be a constant value.*

The power algorithm is developed for the SOUL aircraft with one internal combustion engine and one electric motor.

#### 4.2.1 Power relation in the propulsion system

Several key components to formulate the optimal control problem, including the power demand for maintaining flight, the available power resources in the propulsion system, and their relation, are given as follows.

##### *Power demand*

The power required  $P_{req}$  to maintain flight at a certain velocity  $v$  and thrust  $T$  is given as,

$$P_{req} = T v. \quad (4.1)$$

Under the constant velocity assumption, the following relation is derived from Eq.(2.1c),

$$T = D + W \sin \gamma, \quad (4.2)$$

by combining Eq.(4.1) and Eqs.(2.2), the power demand can be computed as,

$$P_{req} = \frac{1}{2} \rho S C_{D,0} v^3 + \frac{K g^2 \cos^2 \gamma}{\rho S v} m^2 + mg \sin \gamma v. \quad (4.3)$$

During the constant altitude cruise phase, all elements on the right-hand side of Eq.(4.3) are constants except for the total mass  $m$ . Therefore, the required power is a function of the aircraft's total mass in this phase. During the accelerated climb and descent phases, the air density  $\rho$  is a function of the altitude  $h$ , which means that the required power becomes a function of both the total mass and the flight altitude.

### *Power available in the propulsion system*

In the aircraft SOUL, there are two power sources available in the propulsion system: the internal combustion engine that generates mechanical power by burning fuel and the electric motor that is supplied by the battery pack and converts electric energy into mechanical energy.

1. Power provided by the engine:

In this dissertation, it is assumed that the output power of the engine is regulated by the engine's throttle. The throttle serves as the control input in the optimal control problem. The relationship between the output power of the engine  $P_{e,out}$  and the throttle setting is given by:

$$P_{e,out} = \tau P_{e,max}, \quad (4.4)$$

where  $P_{e,max}$  is the maximum output power of the engine. The objective of the optimal control problem is to minimize the fuel consumption. Hence, understanding the specific fuel consumption (SFC) rate of the engine is essential. The actual fuel rate map of the engine is usually confidential. In this section, the data point (efficiency vs. output power) from Friedrich's paper [17] is adopted to fit an approximate curve, shown in Fig. 4.1. The fuel consumption per hour is modeled as a fourth-order polynomial of the engine's output power. It is observed that the optimal working region for the engine is about 4.5kW of output power.

2. Power provided by the electric motor:

It is assumed that the transfer efficiency of the electric motor remains constant, and the output power from the electric path  $P_{m,out}$  is determined by,

$$P_{m,out} = \eta_m P_{bat} = \eta_m U I, \quad (4.5)$$

where  $\eta_m$  is the total efficiency of the electric path;  $U$  is the terminal voltage of the battery pack;  $I$  is the current flowing out of the battery pack. It is assumed that the voltage of the battery pack is a constant value, and the SOC of the battery pack is one of the states in the optimal control problem. The dynamic of the SOC is given by Eq.(3.5).

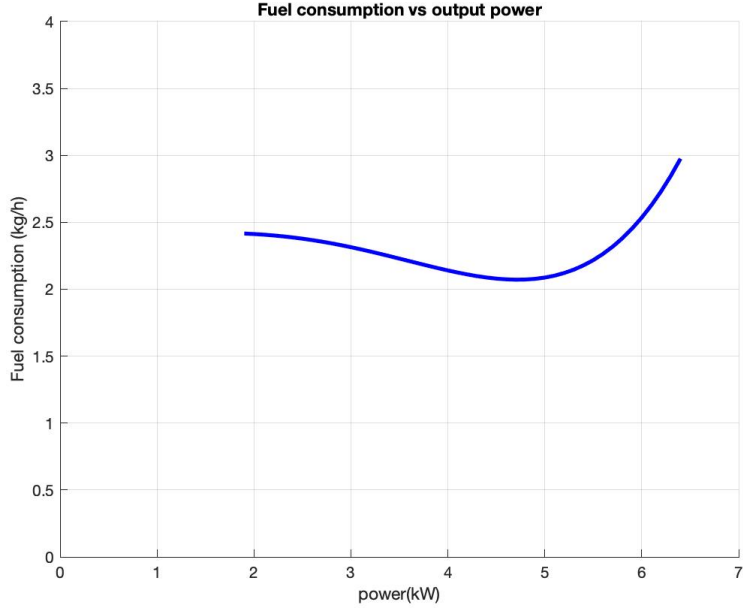


Figure 4.1: Fuel consumption rate at different output power.

#### *Power relation in the propulsion system*

The power available in the propulsion system is provided by the engine and the electric motor; the relation can be presented as

$$P_{\text{req}} = \eta_p(P_{\text{e,out}} + P_{\text{m,out}}), \quad (4.6)$$

where  $\eta_p$  is the transfer efficiency of the propeller, which is also assumed to be a constant value. Combining Eq.(4.1), Eq.(4.4), and Eq.(4.5), the following useful relation can be computed,

$$Tv = \eta_p(\tau P_{\text{e,max}} + \eta_m UI). \quad (4.7)$$

#### *4.2.2 States dynamics and operating modes analysis*

In the fuel minimization problem for the aircraft SOUL, the throttle of the engine is considered as the control input; the total mass of the aircraft and the SOC of the battery pack are the states.

The dynamics of these two states are given as

$$\dot{m} = -\dot{m}_f = -c, \quad (4.8a)$$

$$\dot{\theta} = -\frac{I}{Q}, \quad (4.8b)$$

where  $c$  is the fuel consumption rate (in kg/h), which is a fourth-order polynomial of the engine's output power, given in Eq.(4.9);  $Q$  is the total charge in the battery pack;

$$c = a_0 + a_1 \cdot P_{e,out} + a_2 \cdot P_{e,out}^2 + a_3 \cdot P_{e,out}^3 + a_4 \cdot P_{e,out}^4. \quad (4.9)$$

A HEP in a ground vehicle offers various operating modes to optimize energy usage and performance. These operating modes include:

1. **Electric Mode:** The vehicle operates solely on the electric motor, drawing energy from the battery pack. The ICE remains inactive in this mode.
2. **Engine Mode:** The vehicle operates solely on the ICE, and the electric motor remains inactive.
3. **Combined (Hybrid) Mode:** Both the ICE and the electric motor are active to drive the vehicle. The power distribution varies depending on the driving conditions and power demands.
4. **Power Split Mode:** In this mode, the ICE drives the vehicle and simultaneously charges the battery through the electric motor (working as a generator).
5. **Regenerative Braking Mode:** During braking or deceleration, the electric motor works as a generator, converting kinetic energy into electrical energy to charge the battery.

While theoretically, a HEA could potentially operate in all of these modes, practical constraints related to mechanical connections in the propulsion system and aerodynamics make it impractical and less beneficial to implement regenerative braking mode for aircraft. As a result, the regenerative mode is not considered for aircraft applications. Additionally, the aircraft SOUL cannot operate

in motor-alone mode due to size limitations (we refer the interested readers to [57] for a detailed explanation). As a result, the engine must be active and burn fuel at all times; therefore, the time history profile of the total mass will exhibit a monotonous decrease during flight due to fuel consumption.

When the HEP system works in the combined mode, the  $\theta$  decreases as the electrical charge is drawn from the battery pack. Conversely, in the power split mode, the  $\theta$  increases as the battery pack is charged through the electric motor acting as a generator.

The total mass of the aircraft is constrained by the size of the fuel tank, which determines the aircraft's fuel capacity. Let  $m_{\min}$  and  $m_{\max}$  be the lower and upper bounds for the aircraft's total mass, respectively;  $m_{\max} - m_{\min} = m_{f,0}$ , where  $m_{f,0}$  is the mass of the fuel initially loaded onto the aircraft.

For  $\theta$ , conservative boundary values are set to protect battery cells. In this chapter, the minimum value for  $\theta$  is assumed to be  $\theta_{\min} = 0.3$ , and the maximum value for  $\theta$  during the cruise phase is set to  $\theta_{\max} = 0.8$  to avoid overcharging the battery in flight; for the climb phase, its maximum value is set to 1, indicating that the battery starts from its fully charged state. The initial mass is represented as  $m_0$ ; the initial SOC of the battery pack is  $\theta_0$ .

#### *4.2.3 Fuel minimization problem*

By incorporating these constraints on the total mass and SOC, the formulation of the optimal energy management strategy allows for efficient energy utilization and optimal aircraft performance during different flight phases. The primary objective is to minimize fuel consumption while ensuring the integrity and performance of the battery pack throughout the flight. The decision not to explicitly consider battery charge consumption in the optimization problem is based on the assumption of a simple battery model with a constant voltage output. The value of battery charge consumption can be determined based on the initial and final conditions of the SOC of the battery pack. This simplification allows for a more tractable and computationally efficient optimization problem. Thus, the optimal control problem of interest can be formulated as follows:

**Problem 5.** Determine the time profile of  $\tau$  that solves the following problem:

$$J = \min_{\tau} -m(t_f), \quad (4.10a)$$

$$\text{s.t. } \dot{m} = -c, \quad (4.10b)$$

$$\dot{\theta} = -\frac{I}{Q}, \quad (4.10c)$$

$$m(t_0) = m_0; \quad \theta(t_0) = \theta_0, \quad (4.10d)$$

$$0.1 \leq \tau \leq 1, \quad (4.10e)$$

$$m_{min} \leq m \leq m_{max}; \quad \theta_{min} \leq \theta \leq \theta_{max}. \quad (4.10f)$$

**Remark 1.** Since flight profiles are given in advance, the terminal time  $t_f$  is given, and terminal boundary conditions for states are not necessary.

### Theoretical analysis

In Problem 5, the state constraint for  $\theta$  is an active constraint. This means that the constraint on  $\theta$  plays an active role in shaping the optimal control solution. In order to analyze the first-order necessary condition for optimality in such an optimal control problem with state constraints, a modified minimum principle is required.

**Informal theorem [101]** Given the following optimal control problem:

$$J = \min_{\mathbf{u}} \int_0^{t_f} F(\mathbf{x}(t), \mathbf{u}(t), t) dt + K(\mathbf{x}(t_f), t_f) \quad (4.11a)$$

$$\text{s.t. } \dot{\mathbf{x}}(t) = f(\mathbf{x}(t), \mathbf{u}(t), t), \quad \mathbf{x}(0) = \mathbf{x}_0, \quad (4.11b)$$

$$g(\mathbf{x}(t), \mathbf{u}(t), t) \geq 0, \quad (4.11c)$$

$$h(\mathbf{x}(t), t) \geq 0, \quad (4.11d)$$

$$a(\mathbf{x}(t_f), t_f) \geq 0, \quad (4.11e)$$

$$b(\mathbf{x}(t_f), t_f) = 0, \quad (4.11f)$$

where  $\mathbf{x}$  represents the states of a dynamical system;  $\mathbf{u}$  is the control input;  $F$  is the running cost;  $K$  is the terminal cost; the Hamiltonian  $H$  and Lagrangian  $L$  of this optimal control problem are

defined as

$$H(\mathbf{x}, \mathbf{u}, \boldsymbol{\lambda}, t) = F(\mathbf{x}, \mathbf{u}, t) + \boldsymbol{\lambda}^T \cdot f(\mathbf{x}, \mathbf{u}, t), \quad (4.12)$$

$$L(\mathbf{x}, \mathbf{u}, \boldsymbol{\lambda}, \boldsymbol{\mu}, \boldsymbol{\nu}, t) = H(\mathbf{x}, \mathbf{u}, \boldsymbol{\lambda}, t) + \boldsymbol{\mu}^T g(\mathbf{x}, \mathbf{u}, t) + \boldsymbol{\nu}^T h(\mathbf{x}, t), \quad (4.13)$$

then the optimal solution can be characterized as follows: Let  $\mathbf{x}^*(\cdot), \mathbf{u}^*(\cdot)$  be an optimal pair for the problem (Eqs.(4.11)) over a fixed interval  $[0, t_f]$ , such that  $\mathbf{u}^*(\cdot)$  is right-continuous with left-hand limits. Assume that  $\mathbf{x}^*(\cdot)$  has only finitely many junction times. Then there exist a piecewise absolutely continuous costates trajectory  $\boldsymbol{\lambda}(\cdot)$ , piecewise continuous multiplier functions  $\boldsymbol{\mu}(\cdot)$  and  $\boldsymbol{\nu}(\cdot)$ , and a vector  $\boldsymbol{\eta}(\tilde{t}_i)$  for each point  $\tilde{t}_i$  of discontinuity of  $\boldsymbol{\lambda}(\cdot)$ , for which the following conditions hold almost everywhere:

$$\mathbf{u}^*(t) = \arg \min_{\mathbf{u}} H(\mathbf{x}^*(t), \mathbf{u}(t), \boldsymbol{\lambda}(t), t), \quad (4.14a)$$

$$L_{\mathbf{u}}^*[t] = H_{\mathbf{u}}^*[t] + \boldsymbol{\mu}^T g_{\mathbf{u}}^*[t] = 0, \quad (4.14b)$$

$$\dot{\boldsymbol{\lambda}}(t) = -L_{\mathbf{x}}^*[t], \quad \frac{dH^*[t]}{dt} = \frac{dL^*[t]}{dt}, \quad (4.14c)$$

$$\boldsymbol{\mu}(t) \geq 0, \quad \boldsymbol{\mu}(t)g^*[t] = 0, \quad (4.14d)$$

$$\boldsymbol{\nu}(t) \geq 0, \quad \boldsymbol{\nu}(t)h^*[t] = 0. \quad (4.14e)$$

At the terminal  $t_f$ , the transversality conditions are given based on more information about controls. For any time  $\tilde{t}$  in a boundary interval and for any contact time  $\tilde{t}$  (states hit the boundary conditions), the costate trajectory  $\boldsymbol{\lambda}$  may have discontinuity given by the following jump conditions:

$$\boldsymbol{\lambda}(\tilde{t}^-) = \boldsymbol{\lambda}(\tilde{t}^+) + \boldsymbol{\eta}(\tilde{t})h_{\mathbf{x}}^*[\tilde{t}], \quad \boldsymbol{\eta}(\tilde{t}) \geq 0, \quad \boldsymbol{\eta}(\tilde{t})h^*[\tilde{t}] = 0, \quad (4.15a)$$

$$H^*[\tilde{t}^-] = H^*[\tilde{t}^+] - \boldsymbol{\eta}(\tilde{t})h_t^*[\tilde{t}]. \quad (4.15b)$$

This theorem is applied to Problem 5. First, the Hamiltonian (there is no running cost  $F$  in this problem; only the terminal cost is considered) and Lagrangian for this problem are given as

$$H(\mathbf{x}, \mathbf{u}, \boldsymbol{\lambda}, t) = \lambda_m(\dot{m}) + \lambda_{\theta}(\dot{\theta}), \quad (4.16)$$

$$L(\mathbf{x}, \mathbf{u}, \boldsymbol{\lambda}, \boldsymbol{\mu}, \boldsymbol{\nu}, t) = \lambda_m(\dot{m}) + \lambda_{\theta}(\dot{\theta}) + \nu_1(-\theta + \theta_{max}) + \nu_2(\theta - \theta_{min}), \quad (4.17)$$

to simplify expressions, we write the dynamics for  $m$  and  $\theta$  as

$$\dot{m} = -c_0 - c_1 \cdot \tau - c_2 \cdot \tau^2 - c_3 \cdot \tau^3 - c_4 \cdot \tau^4, \quad (4.18a)$$

$$\dot{\theta} = -\frac{(A + Bm^2 + mgv \sin \gamma)/\eta_p - \tau P_{e,max}}{\eta_m U Q}, \quad (4.18b)$$

where  $A = \frac{1}{2}\rho S C_{D,0} v^3$  and  $B = \frac{Kg^2 \cos^2 \gamma}{\rho S v}$ .

The optimal control should satisfy Eq.(4.14a), which is

$$u^* = \arg \min_u (\lambda_m(\dot{m}^*) + \lambda_\theta(\dot{\theta}^*)), \quad (4.19)$$

and the dynamics of costates with respect to time is derived from Eq.(4.14c),

$$\dot{\lambda}_m = -\frac{\partial L}{\partial m} = -[-\lambda_\theta \frac{2Bm + gv \sin \gamma}{\eta_m U Q \eta_p}], \quad (4.20a)$$

$$\dot{\lambda}_\theta = -\frac{\partial L}{\partial \theta} = -[-\nu_1 + \nu_2]. \quad (4.20b)$$

Analyzing Eq.(4.19), we observe that the Hamiltonian is a fourth-order polynomial of the control input. As such, in order to obtain its minimum, we could take its derivative with respect to the control input, arriving at the following condition,

$$\lambda_m(-c_1 - 2c_2\tau - 3c_3\tau^2 - 4c_4\tau^3) + \lambda_\theta\left(\frac{P_{e,max}}{\eta_m U Q}\right) = 0. \quad (4.21)$$

In this equation, both  $\lambda_m$  and  $\lambda_\theta$  change along with time; hence, we do not have a closed form for the optimal control. One way to solve this problem based on our analyses is to express  $\tau$  with  $\lambda_m$ ,  $\lambda_\theta$  and other parameters from Eq.(4.21), then construct a set of ODEs and solve an initial value problem (with initial guesses for the costates). The states of this ODE initial value problem are original states and the corresponding costates  $\lambda_m$  and  $\lambda_\theta$ .

#### 4.2.4 Numerical results

The numerical results obtained from Tomlab for Problem 5 during different phases are presented. The information about the costates provided by Tomlab helps to testify the consistency between

the numerical results and theoretical analyses.

#### *Constant altitude cruise phase*

For illustrating the impact of flight profiles on optimal power allocation results, we consider four distinct flight profiles with different boundary conditions during the cruise phase,

1. Case 1:  $v = 20m/s$ ,  $\theta(t_0) = 0.6$ ,  $\theta(t_f) = 0.5$ ;
2. Case 2:  $v = 25m/s$ ,  $\theta(t_0) = 0.6$ ,  $\theta(t_f) = 0.5$ ;
3. Case 3:  $v = 30m/s$ ,  $\theta(t_0) = 0.6$ ,  $\theta(t_f) = 0.5$ ;
4. Case 4:  $v = 30m/s$ ,  $\theta(t_0) = 0.8$ ,  $\theta(t_f) = 0.4$ .

For all cases, the terminal horizontal distance is set to be 74km, and the corresponding terminal time  $t_f$  can be computed based on the flight profile and required speed; the initial total mass is  $m_0 = 210$  kg; constraints for states and control input are given as

$$185kg \leq m \leq 210kg \quad (4.22a)$$

$$0.3 \leq \theta \leq 0.8 \quad (4.22b)$$

$$0.1 \leq \tau \leq 1 \quad (4.22c)$$

The optimal solutions provided by Tomlab lead to the following observations:

1. *Charging the battery during the cruise phase slightly improves the engine efficiency.*

Fig. 4.2 and Fig. 4.3 show the time history profiles of case 1. In this case, the engine is allowed to charge the battery pack through the electric motor/generator. It is observed from Fig. 4.2c that the SOC of the battery pack increases from 10 minutes to about 47 minutes, and on this interval, the fuel rate is relatively low compared to other intervals. The comparison between Fig. 4.3c and Fig. 4.3a indicates that when the fuel rate is relatively low, the output engine power is about 4.2 kW, which is within the engine's efficient working region. In contrast, during other intervals when the engine's throttle is only 0.1, the fuel rate is nearly 2.45 kg/h.

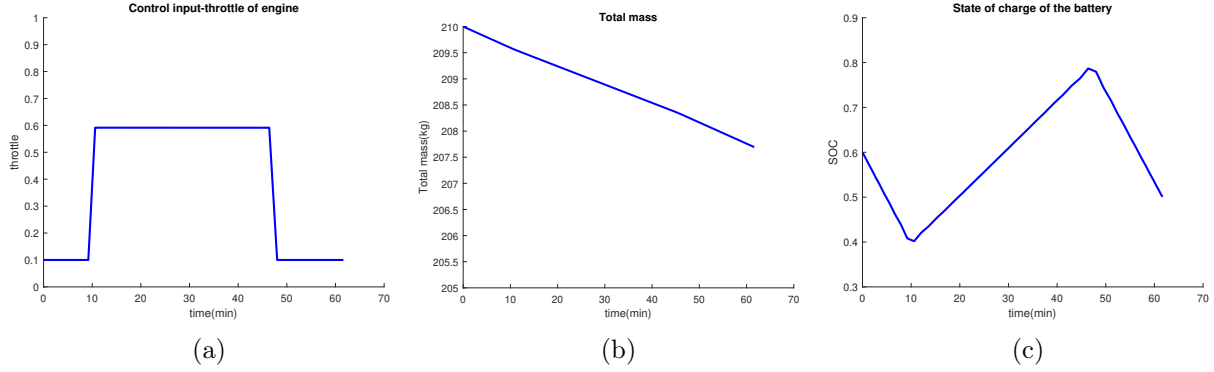


Figure 4.2: Case 1–control input and states: (a) the throttle of the engine, (b) the total mass, (c) the SOC of the battery pack.

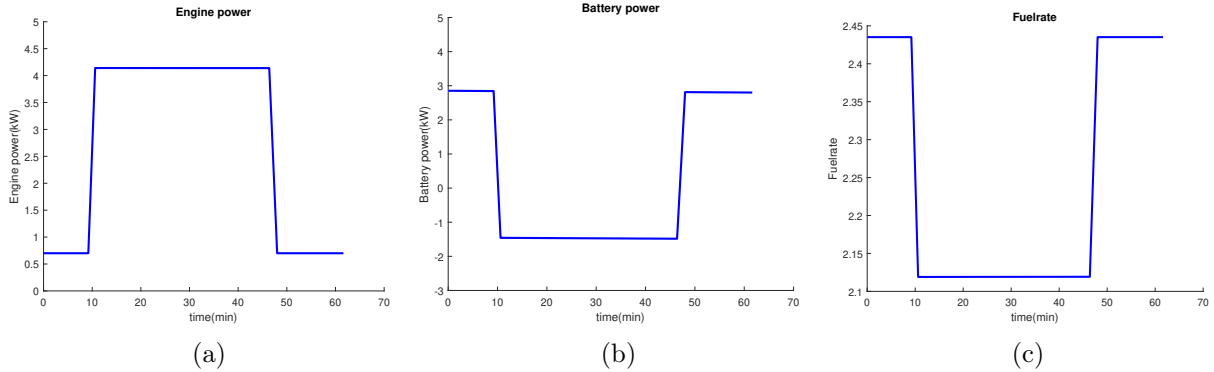


Figure 4.3: Case 1–power allocation and fuel consumption rate: (a) engine output power, (b) battery output power, (c) the corresponding fuel rate (kg/h) under control.

The total fuel consumption of case 1 is 2.31 kg when we allow the engine to charge the battery during flight. Now, we change one of the constraints while implementing Tomlab to solve this problem. The original constraint on the current is  $-220A \leq I \leq 220A$ ; now, we set this constraint as  $0 \leq I \leq 220A$ , meaning that we cannot use the engine to charge the battery. The results are given in Fig. 4.4 and Fig. 4.5.

The total fuel consumption is 2.4 kg when we change the current constraint. By comparing this with the previous case, where the engine was allowed to charge the battery, we observe a minimal amount of fuel saving of 0.09 kg (the aircraft model we use here is an ultralight

aircraft, and the average fuel rate is  $2.2\text{kg}/\text{h}$ , which is a relatively small value; hence the fuel saving is relatively small). The reason for this fuel saving is that when the engine is utilized to charge the battery, it operates in a more efficient region where the specific fuel consumption rate is relatively low. This optimized operation leads to a slight improvement in overall engine efficiency, resulting in the observed fuel saving.

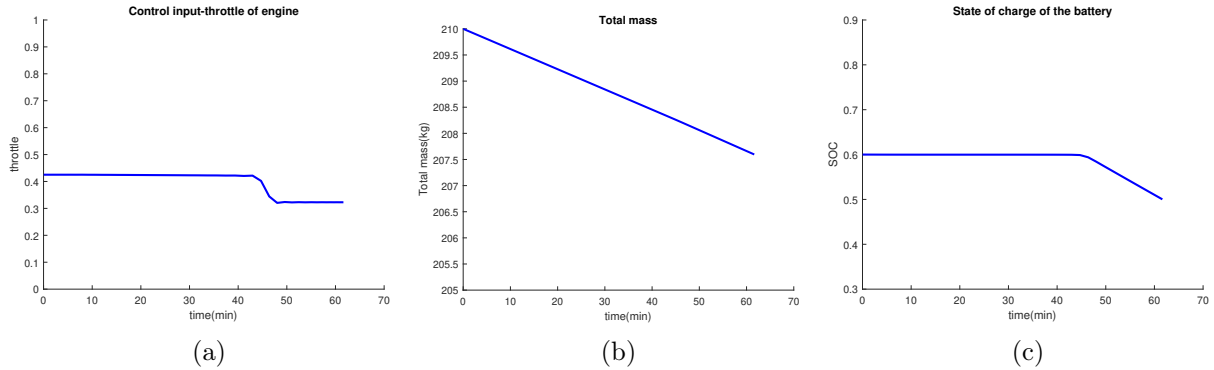


Figure 4.4: Case 1 (Not charging the battery pack during flight)—control input and states: (a) the throttle of the engine, (b) the total mass, (c) the SOC of the battery pack.

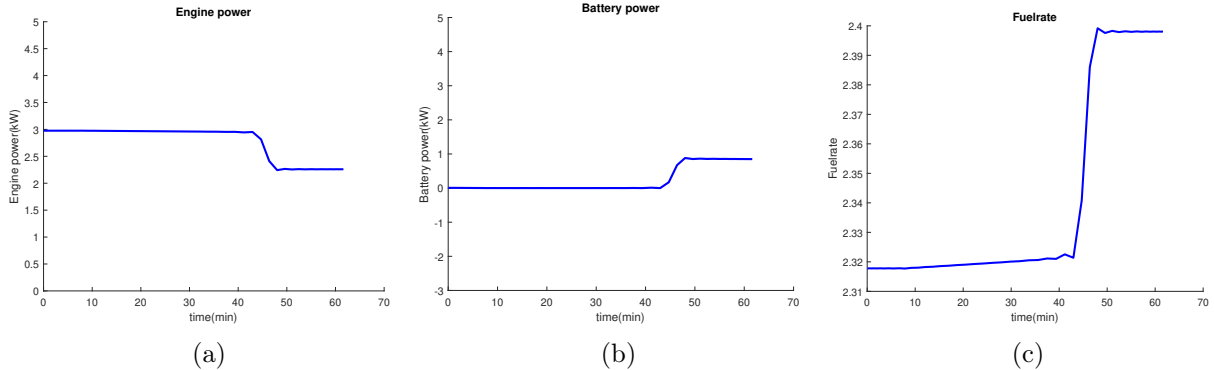


Figure 4.5: Case 1 (Not charging the battery pack during flight)—power allocation and fuel consumption rate: (a) engine output power, (b) battery output power, (c) the corresponding fuel rate ( $\text{kg}/\text{h}$ ) under control.

2. Different cruise speeds lead to different power allocation as well as different switching times.

The SOC and fuel rate for the first three cases are compared, and the results are presented in Figures 4.6 to 4.8.

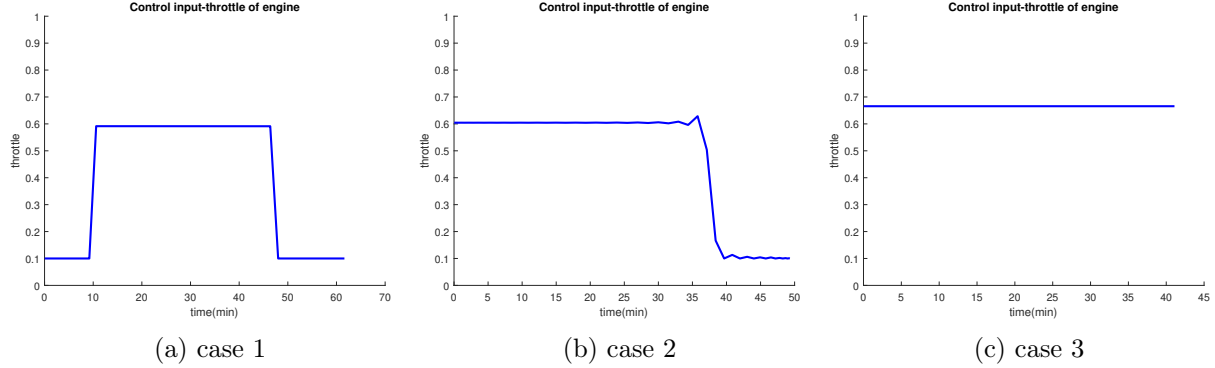


Figure 4.6: The time history profiles of control input for the first three cases.

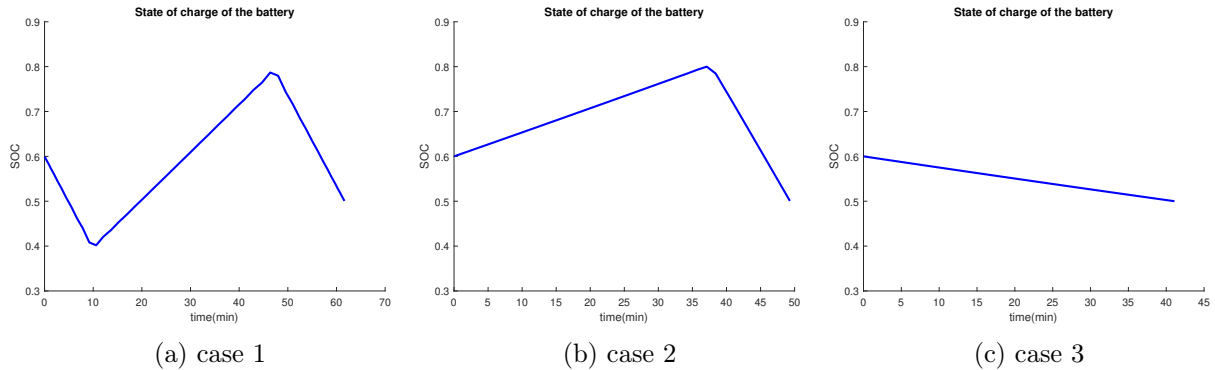


Figure 4.7: The time history profiles of SOC for the first three cases.

By comparing the control input profiles (Fig. 4.6) and the corresponding fuel rate profiles (Fig. 4.8), we can observe a common trend in the logic of optimal control solutions for all three cases. The optimal control strategy steers the throttle to around 0.6 while simultaneously satisfying the boundary conditions. This particular throttle setting allows the aircraft to achieve an efficient power allocation, which is achieved by charging the battery pack (Fig. 4.7). In this relatively efficient region, the fuel rate hovers around 2.1 kg/h, which is the minimum value that the engine can take.

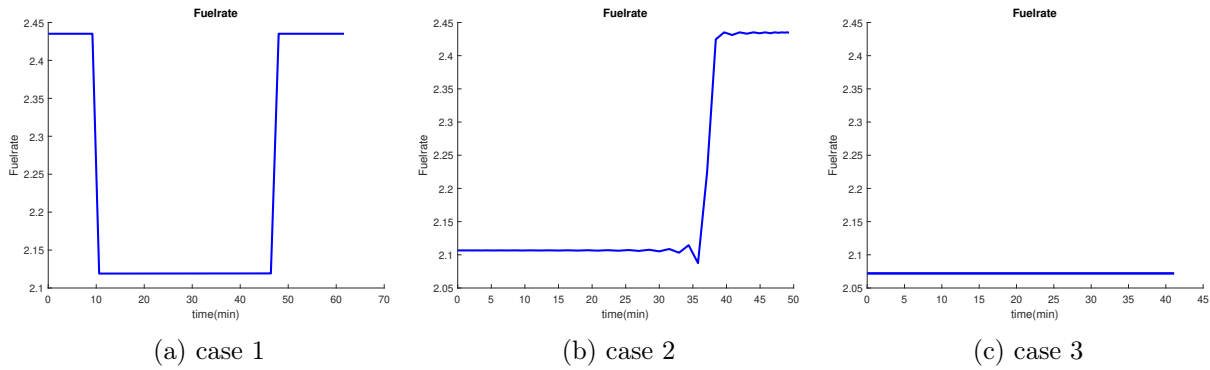


Figure 4.8: The time history profiles of fuel rate for the first three cases.

3. Boundary conditions also affect the power allocation results.

To verify this statement, we compare cases 3 and 4, both having the same cruise speeds but different boundary conditions for the SOC of the battery pack. Since the trend of the engine power profile is identical to the control input profile, we focus on comparing the control input profiles here. From Fig. 4.9, it is observed that for case 3, by taking the combined mode all the time, the propulsion system can achieve its optimal fuel efficiency. For case 4, we have more battery capacity available, and the optimal solution shows that the HEP system should run out of battery capacity and try to stay in the efficient region as long as possible.

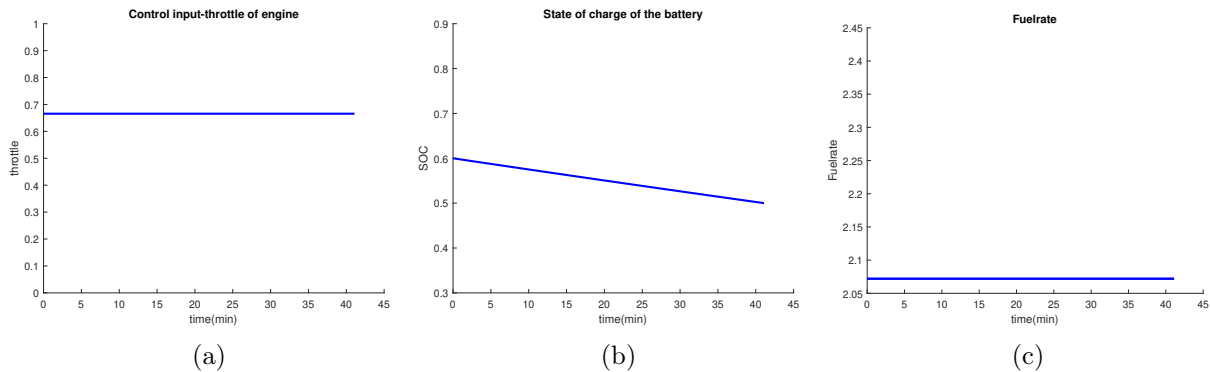


Figure 4.9: The time history profiles for case 3.

The fundamental characteristic of the control strategy during the cruise phase is to steer the

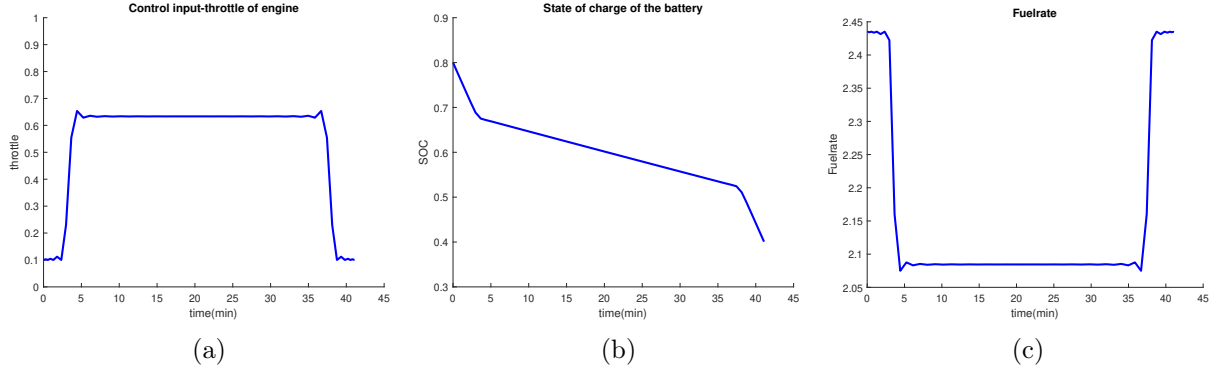


Figure 4.10: The time history profiles for case 4.

engine to work within its efficient region for as long as possible while still satisfying the boundary conditions for the SOC. When the power demand exceeds the combination of efficient engine power (about 4.5 kW) and electrical power, the HEP system should run out of available battery charge while keeping engine power around 4.5 kW; when the power demand is lower than the efficient engine power, the control strategy should adopt the power split mode on certain time intervals.

#### *Constant speed climb phase*

One of the primary benefits of the HEP system is its energy-saving potential due to the inclusion of an additional electrical energy source, which also allows the downsizing of the engine. Hence, during the climb phase, the engine and the electric motor should work in the combined mode to drive the vehicle together. With this observation, we will now delve into fuel minimization for HEA during the climb phase.

The flight profile is given as follows: the climb speed is 20 m/s, the terminal climb height is 700 m, and the terminal horizontal distance for the climb phase is about 3.7 km.

Eq.(4.3) provides the method of computing the required power to fly at a constant speed. The air density is constant during the cruise phase; however, during the climb phase, this value varies with the altitude. When using Tomlab to solve the optimal control problem, the US Standard Atmosphere (1976) model is applied to calculate the air density based on altitude information.

For states and control input constraints, it is assumed that the battery pack is fully charged

before take-off ( $\theta = 1$ ). Hence, constraints during the climb phase are given as

$$185kg \leq m \leq 210kg \quad (4.23a)$$

$$0.3 \leq \theta \leq 1 \quad (4.23b)$$

$$0.1 \leq \tau \leq 1 \quad (4.23c)$$

The numerical solutions are given in Fig. 4.11 and Fig. 4.12.

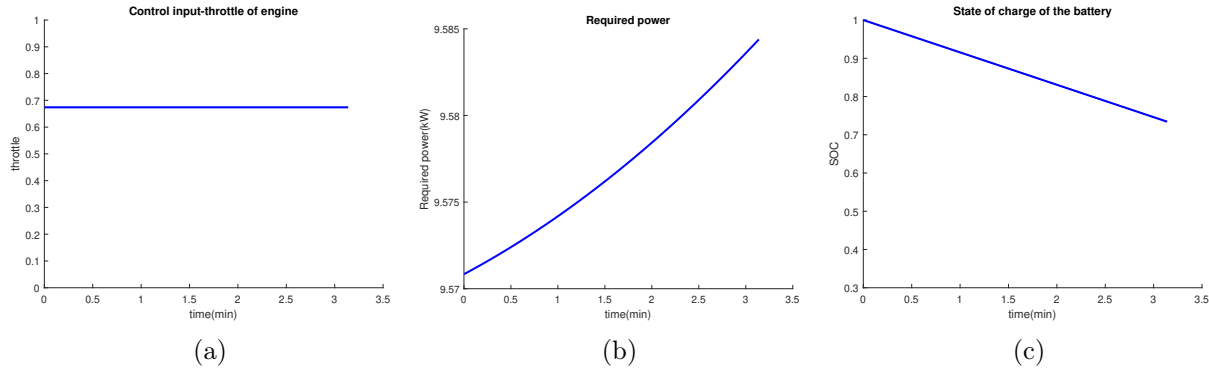


Figure 4.11: Climb phase control input and states: (a) the throttle of the engine, (b) the total mass, (c) the SOC of the battery pack.

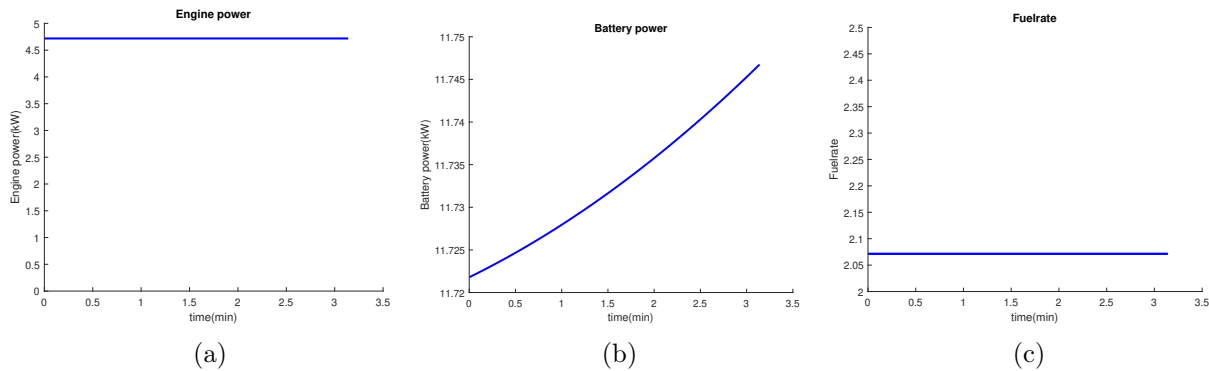


Figure 4.12: Climb phase power allocation and fuel consumption rate: (a) engine output power, (b) battery output power, (c) the corresponding fuel rate (kg/h) under control.

During the cruise phase, the required power exhibits a monotonically decreasing behavior as the aircraft burns fuel continuously. However, during the climb phase, the required power follows a different trend. This is attributed to the fact that  $P_{req}$  depends not only on the total mass but also on the air density  $\rho$ , which varies with altitude. Consequently, as the aircraft ascends, the changing air density impacts the power requirements. From the fuel consumption figure (Fig. 4.12c), a pattern similar to that during the cruise phase is observed: when the engine's output power is around 4.5 kW, the engine operates within its optimal operation region, resulting in relatively low fuel consumption rate during this region. Fig. 4.11a and Fig. 4.12c demonstrate that the optimal solution involves steering the engine to operate within its optimal region.

To further verify this observation, the following climb profiles are tested, and a comparison of the power allocation results is made.

1. Case 1:  $h = 700$  m,  $x_{cl} = 2$  nm,  $\gamma = 10.7$  deg;

The power required to climb is around 9.62 kW; considering the efficiency of the propeller, the power demanded from the propulsion system is around 14.17 kW; the optimal solution shows that the engine's output power should be around 4.72 kW, and the electrical power should be about 11.8 kW;

2. Case 2:  $h = 700$  m,  $x_{cl} = 3$  nm,  $\gamma = 7.2$  deg;

The power required to climb is around 7.15 kW; the power demanded from the propulsion system is around 10.53 kW; the optimal solution shows that the engine power should be about 4.72 kW, and the electrical power should be around 7.26 kW.

These two cases show that during the climb phase, the required power to fly is higher than the maximum output power of the engine. As such, the combined mode must be chosen to maintain flight; what the optimal control does is to allocate the power between the engine and the electric motor in order to minimize fuel consumption by steering the engine to operate within its optimal region.

### ***4.3 Comparison of two parallel hybrid electric configurations***

One observation drawn from §4.2.4 indicates that charging the battery during specific flight conditions slightly enhances the engine’s efficiency. However, it is noteworthy that the reduction in fuel consumption is minimal. Initially, we hypothesized that this scenario might be attributed to the size of the aircraft model: the fuel consumption is already quite limited, making it difficult to observe a clear difference between charging and not charging the battery during flight. To further investigate this scenario, we applied the power allocation algorithm to a larger conceptual aircraft (listed in §2.1), yet the resulting fuel-saving remains insignificant. This observation prompts a fundamental question: Is it indeed worthwhile to charge the battery during flight at all? Considering the limited impact on fuel consumption, conducting a more comprehensive investigation and analysis becomes important to determine the practical benefits and feasibility of implementing battery charging strategies during flight.

In this section, two parallel hybrid electric configurations, one with a mechanical connection between the engines and the electric motors and the other without, are compared in the context of fuel minimization. The power allocation algorithm proposed in §4.2 is transformed into a finite-dimensional optimization problem and employed in both of the aforementioned hybrid electric configurations. Subsequently, sensitivity analyses are performed to investigate the effects of charging the battery during flight and the influence of the initial take-off weight on fuel consumption.

#### *4.3.1 Parallel hybrid electric architectures*

For a conventional aircraft that relies on engines for propulsion, it is challenging to devise effective methods to operate the engine within its peak efficiency regime; this is primarily due to significant variations in power requirements between the climb and cruise phases of a typical flight profile. One of the key benefits associated with hybrid electric aircraft is the ability to reduce the size of the engine and utilize the electric motor as supplementary propulsion, allowing the engine to operate at its most efficient regime during flight. As a result, when adopting this perspective for the development of hybrid-electric aircraft architectures, designers frequently assume a mechanical connection in the propulsion system. The most commonly employed architectures include series, parallel, and series-parallel configurations. The parallel architecture is the most popular configuration due to

its relatively higher efficiency and lower weight (in comparison with the series configuration), as well as its simpler energy management (as compared with the series-parallel configuration). In general, a mechanical connection in the propulsion system enables conventional engines to operate more efficiently, either by decoupling the engine from the propeller (in the series configuration) or by taking the electric motor as an extra load for the engine (in the parallel configuration). Nevertheless, to the best of our knowledge, this potential advantage of having a mechanical connection in HEA has not been validated, either theoretically or experimentally.

In addition, the mechanical connection between the conventional engine and the electric motor often necessitates a complex clutch/gearing mechanism and an advanced control algorithm for the hybrid propulsion system. In addition, charging the battery during flight introduces new challenges, such as the need for more sophisticated cooling systems and the possibility of battery pack degradation.

On the other hand, MagniX has recently proposed a novel hybrid structure (similar to the “Through-the-Road” structure employed in automobiles) for aircraft electric propulsion. In particular, the conventional engine and electric paths are *mechanically independent* in the Magnix design, with two entirely separate control systems for each propulsion path. With this architecture, the hybrid electric propulsion system can still be advantageous as it allows for efficient engine operation. Additionally, the absence of mechanical connections reduces the overall weight of the aircraft and may improve safety due to a simplified mechanical system.

This dissertation examines the standard parallel architecture (referred to as the connected configuration) and the MagniX architecture (referred to as the independent configuration). In the connected configuration, as illustrated in Fig. 4.13, both the internal combustion engine/gas turbine and the electric motor are connected to the propeller. As a result, this configuration supports the following operating modes: *a*) Engine mode, *b*) Motor mode, *c*) Combined mode, and *d*) Power split mode (details listed in §4.2.2). In the independent configuration, as illustrated in Fig. 4.14, the propulsion system retains the first three operating modes; however, the engine cannot charge the battery during flight.

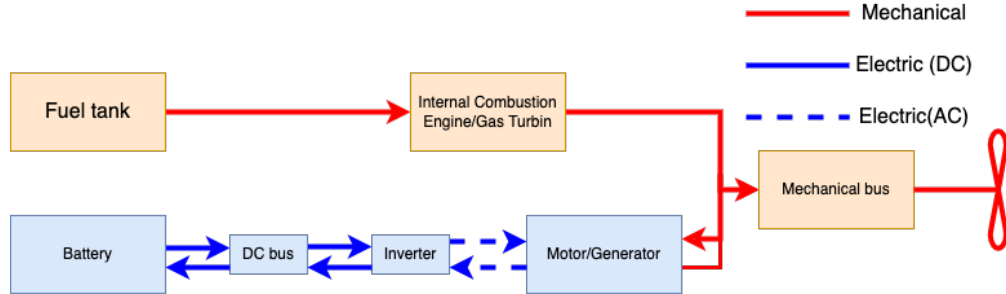


Figure 4.13: Connected parallel hybrid architecture.

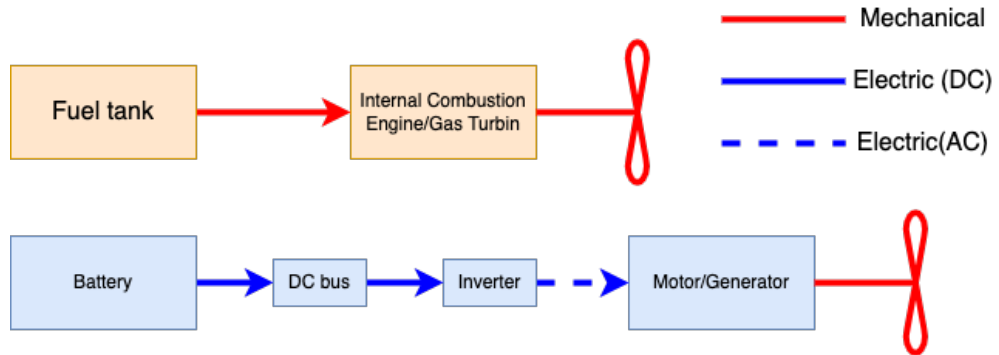


Figure 4.14: Independent parallel hybrid architecture.

#### 4.3.2 Power allocation problem transformation

The HEA power allocation problem in §4.2 (represented as an optimal control problem) is reformulated as a finite-dimensional optimization problem; the second-order sufficient conditions for the solution to this problem are verified, and numerical simulations for the conceptual aircraft model (in §2.1.3) are then provided in this subsection.

##### Analytic setup

In §4.2, the aircraft was assumed to have a connected hybrid structure and that the engine can charge the battery during flight. The objective was to minimize fuel consumption, equivalent to maximizing the terminal weight of the aircraft. The flow rate was assumed to be a fourth-order polynomial of the engine's output power. For the conceptual aircraft model proposed in §2.1.3, however, it is assumed that the flow rate  $c$  is nearly a linear function of the engine's output power.

Instead of using the SFC and power to compute the flow rate, a representation of the flow rate as a function of the output power is derived, and the dynamics of the aircraft mass is re-parameterized as a linear function of the control input as,

$$\dot{m} = -(c_1 P_{e,out} + c_2 P_{e,out}) = \tilde{c}_1 \tau + \tilde{c}_2. \quad (4.24)$$

In order to examine the effect of the battery pack capacity on fuel consumption, rather than the SOC of the battery pack, the remaining charge  $q$  in the battery pack is used as a state whose dynamic is given by

$$\dot{q} = -I. \quad (4.25)$$

In theory, the performance and solution of an optimal control problem are independent of the magnitude of the states and the control input. In practice, however, numerical issues may arise in the solver when these magnitudes are vastly different; in Problem 5, the mass of the conceptual aircraft is approximately 6000 kg, the range of the state of charge of the battery pack is zero to one, and the battery pack capacity is 400 Ah. Hence, we employ the standard remedy of applying the affine variable transformations to the aircraft mass and the remaining charge in the battery pack, namely,

$$\hat{m} = a_1 m + b_1, \quad (4.26a)$$

$$\hat{q} = a_2 q + b_2, \quad (4.26b)$$

we now define the scaled time  $\hat{\tau} \in [0, 1]$ ; the dynamics of “scaled states” with respect to the “scaled time” is written as,

$$\dot{\hat{m}} = k_{11}\tau + k_{10}, \quad (4.27a)$$

$$\dot{\hat{q}} = k_{21}\tau + k_{20} + k_{22}\hat{m}^2 + k_{23}\hat{m}, \quad (4.27b)$$

where both states are linear in the control input  $\tau$ . The scaled optimal control problem is now written as,

**Problem 6.** Find  $\tau$  that solves the following problem

$$J = \min_{\tau} -\hat{m}(\hat{t} = 1) \quad (4.28a)$$

$$\text{s.t. } \dot{\hat{m}} = k_{11}\tau + k_{10}, \quad (4.28b)$$

$$\dot{\hat{q}} = k_{21}\tau + k_{20} + k_{22}\hat{m}^2 + k_{23}\hat{m}, \quad (4.28c)$$

$$\hat{m}(0) = 1, \quad \hat{q}(0) = \hat{q}_0, \quad (4.28d)$$

$$\hat{q}(1) = \hat{q}_f, \quad (4.28e)$$

$$0 \leq \tau \leq 1, \quad (4.28f)$$

$$0 \leq \hat{m} \leq 1, \quad 0 \leq \hat{q} \leq 1, \quad (4.28g)$$

where  $-\hat{m}(\hat{t} = 1)$  represents the negative of the aircraft's terminal mass.

The dynamics of both states are linear in the control input with boundaries; hence, this formulation of the power allocation problem is in the form of a bang-bang control problem with state constraints, where the optimal control switches between the boundary values and possible singular arcs (we refer the interested reader to [22] for a detailed introduction to the bang-bang principle in optimal control). When solving this problem using Tomlab for a reasonable flight profile, the only active state constraint is  $\hat{q} = 1$ ; hence, we subsequently only consider the constraint,

$$S(\hat{q}(\hat{t})) = \hat{q} - 1 \leq 0. \quad (4.29)$$

in the sequel  $S(\hat{q}(\hat{t})) \leq 0$  is denoted as  $S$  for brevity. An interval  $[\hat{t}_1, \hat{t}_2] \in [0, 1]$  is called a boundary arc if  $S(\hat{q}(\hat{t})) \equiv 0$  holds for all  $\hat{t} \in [\hat{t}_1, \hat{t}_2]$ . Hence on the boundary arc the derivative of  $S$  with respect to the scaled time  $\hat{t}$  should be zero for all  $\hat{t} \in [\hat{t}_1, \hat{t}_2]$ , where,

$$\frac{dS}{d\hat{t}} = \frac{\partial S}{\partial \mathbf{x}} \frac{\partial \mathbf{x}}{\partial \hat{t}} = [0 \ 1] \begin{bmatrix} \dot{\hat{m}} \\ \dot{\hat{q}} \end{bmatrix} = \dot{\hat{q}}, \quad (4.30)$$

with  $\mathbf{x} = [\hat{m} \ \hat{q}]^\top$ . Hence, the boundary control  $\tau_b$  can be computed from  $\frac{dS}{d\hat{t}} = \dot{\hat{q}} = 0$  as the following feedback expression

$$\tau_b = -\frac{1}{k_{21}}(k_{20} + k_{22}\hat{m}^2 + k_{23}\hat{m}). \quad (4.31)$$

The augmented Hamiltonian of Problem (4.28) is given as,

$$\begin{aligned} H &= \lambda_1 \dot{\hat{m}} + \lambda_2 \dot{\hat{q}} + \eta S \\ &= \lambda_1 k_{10} + \lambda_2 (k_{20} + k_{22} \hat{m}^2 + k_{23} \hat{m}) + \eta (\hat{q} - 1) + (\lambda_1 k_{11} + \lambda_2 k_{21}) \tau \\ &= H_1 + \sigma(\hat{t}) \tau. \end{aligned} \quad (4.32)$$

Note that the Hamiltonian is linear in the control  $\tau$ ; from the Pontryagin's minimum principle [22], the optimal control on interior arcs with  $S < 0$  is obtained as,

$$\tau^* = \begin{cases} \tau_{\max} & \text{if } \sigma(t) < 0 \\ \tau_{\min} & \text{if } \sigma(t) > 0. \end{cases} \quad (4.33)$$

For a boundary arc, the optimal control has been computed as  $\tau_{\min} < \tau_b < \tau_{\max}$ . Since the optimal control should minimize the Hamiltonian, this minimum principle yields,

$$\sigma(\hat{t}) = 0, \quad \text{for all } \hat{t} \in [\hat{t}_1, \hat{t}_2]. \quad (4.34)$$

This relation is interpreted as the property that the boundary control behaves formally like a singular control by Maurer in [102]. Using Tomlab to solve Problem 6, the optimal control follows a “max-boundary-min” structure. Combining the numerical results with the preceding theoretical analysis yields the following optimal control structure,

$$\tau^* = \begin{cases} \tau_{\max}, & \text{if } 0 \leq \hat{t} \leq \hat{t}_1, \\ \tau_b, & \text{if } \hat{t}_1 \leq \hat{t} \leq \hat{t}_2, \\ \tau_{\min}, & \text{if } \hat{t}_2 \leq \hat{t} \leq 1. \end{cases} \quad (4.35)$$

This optimal control problem is then formulated as a finite-dimensional optimization problem to investigate the second-order sufficient conditions and the sensitivity to initial state conditions. This approach is particularly useful when the structure of the optimal control, i.e., the sequence of bang-bang and boundary arcs, has been derived. The *arc-parameterization* method in [103] is applied to formulate the optimization problem with variables  $\mathbf{x} = [\xi_1, \xi_2, \xi_3, z]^T$  (different  $\mathbf{x}$  than

in Eq. (4.30)) as,

$$\xi_1 = \hat{t}_1 - 0, \quad \xi_2 = \hat{t}_2 - \hat{t}_1, \quad \xi_3 = \hat{t}_f - \hat{t}_2, \quad z = \hat{m}(\hat{t}_2),$$

the last variable is introduced for the simplicity of constraints formulation. The power allocation problem can now be represented as an optimization problem,

**Problem 7.** Find four variables  $\mathbf{x} = [\xi_1, \xi_2, \xi_3, z]^\top$  that solves the following problem,

$$\min_{\mathbf{x}} G := -z - k_{10}\xi_3 \quad (4.37a)$$

$$\text{s.t. } \Phi_1 := h_{13}\xi_1^3 + h_{12}\xi_1^2 + h_{11}\xi_1 + h_{10} - 1 = 0, \quad (4.37b)$$

$$\Phi_2 := g_{13}\xi_3^3 + g_{12}z\xi_3^2 + g_{11}\xi_3^2 + k_{20}\xi_3 + k_{22}z^2\xi_3 + k_{23}z\xi_3 + 1 - \hat{q}_f = 0, \quad (4.37c)$$

$$\Phi_3 := z - \frac{-\tan(\frac{r_0\xi_2}{2}) + f_1m_0 + f_2\xi_1 + f_3}{f_1(1 + \tan(\frac{r_0\xi_2}{2}))(f_1m_0 + f_2\xi_1 + f_3)} + \frac{k_{31}}{2k_{32}} = 0, \quad (4.37d)$$

$$\Phi_4 := \xi_1 + \xi_2 + \xi_3 = 1. \quad (4.37e)$$

Appendix A.1 explains in detail how this optimization problem is derived from the original optimal control problem. Note that the Lagrangian used to deduce second-order sufficient conditions for Problem 7 is

$$L := G + \rho_1\Phi_1 + \rho_2\Phi_2 + \rho_3\Phi_3 + \rho_4\Phi_4. \quad (4.38)$$

### Numerical case study

To examine the power allocation problem for the HEA, the following flight conditions are considered:  $y_d = 400$  km,  $v = 100$  m/s,  $\theta_0 = 0.7$ ,  $m_0 = 6350$  kg,  $\theta_f = 0.4$ ; we use Tomlab to solve Problem 6 and re-scale the results back to their original states. Numerical results are shown in Fig. 4.15 and Fig. 4.16. The fuel consumed for this example is 310.8 kg. Fig. 4.16 shows that the optimal control structure follows the optimal control structure in Eq. (4.35).

The corresponding optimization problem is then solved with ipopt in CasADi [104]; the optimal variables are determined as,  $[\xi_1, \xi_2, \xi_3, z]^\top = [0.1807, 0.6801, 0.1392, 0.3706]$ , and the optimal objective value is  $-\hat{m}(1) = -0.3525$ . Hence, the aircraft's terminal mass is  $m = 6039.2$  kg and 310.8 kg of fuel is consumed. In this numerical case, the dual variables are also provided by ipopt,

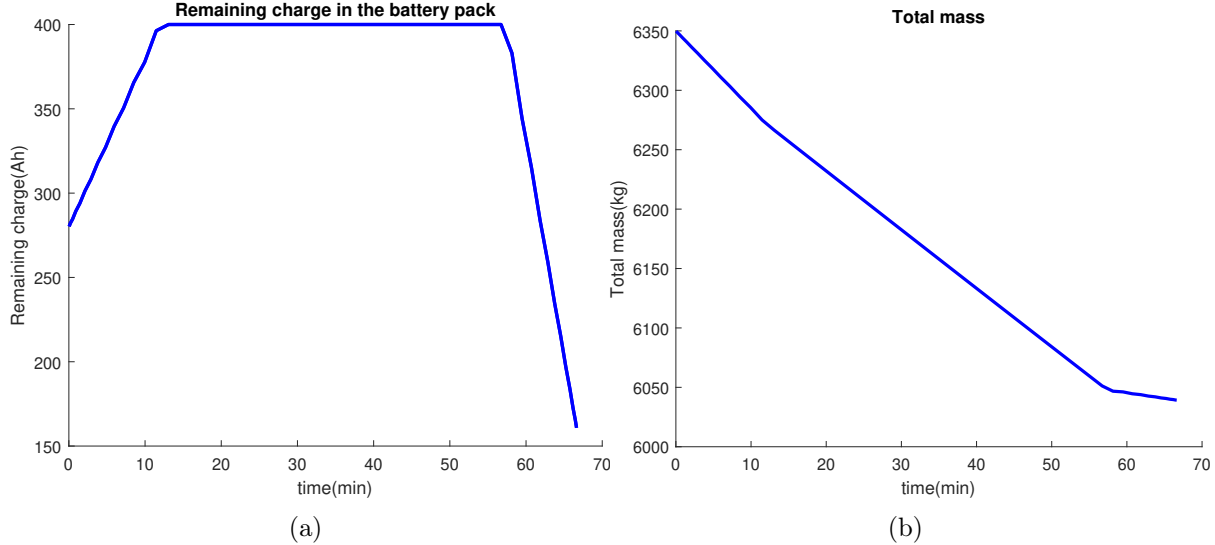


Figure 4.15: (a) Remaining charge in the battery pack; (b) Total mass of the aircraft.

namely,  $[\rho_1, \rho_2, \rho_3, \rho_4] = [-0.1253, -0.1272, 0.9971, -0.6783]$ ; the first order necessary condition for optimality is checked, i.e.,  $L_{\mathbf{x}} = 0$ ; moreover, the Hessian  $L_{\mathbf{xx}}$  of the Lagrangian for  $\mathbf{x} = [0.1807, 0.6801, 0.1392, 0.3706]$  is

$$L_{\mathbf{xx}} = \begin{bmatrix} -0.0186 & -0.0188 & 0 & 0 \\ -0.0188 & -0.0144 & 0 & 0 \\ 0 & 0 & -0.0028 & 0.0211 \\ 0 & 0 & 0.0211 & 0.0002 \end{bmatrix} \quad (4.39)$$

and

$$\Phi_{\mathbf{x}} = \begin{bmatrix} 1.6741 & 0 & 0 & 0 \\ 0 & 0 & -4.3085 & -0.0231 \\ 0.8907 & 0.6803 & 0 & 1 \\ 1 & 1 & 1 & 0 \end{bmatrix}, \quad (4.40)$$

with  $\text{rank } \Phi_{\mathbf{x}} = 4$  and  $L_{\mathbf{xx}}$  as positive definite. Hence, the second-order sufficient conditions are satisfied, and the optimal solution is unique and, in fact, globally optimal. With this transition to the finite-dimensional optimization problem, one can conduct sensitivity analysis on the optimal

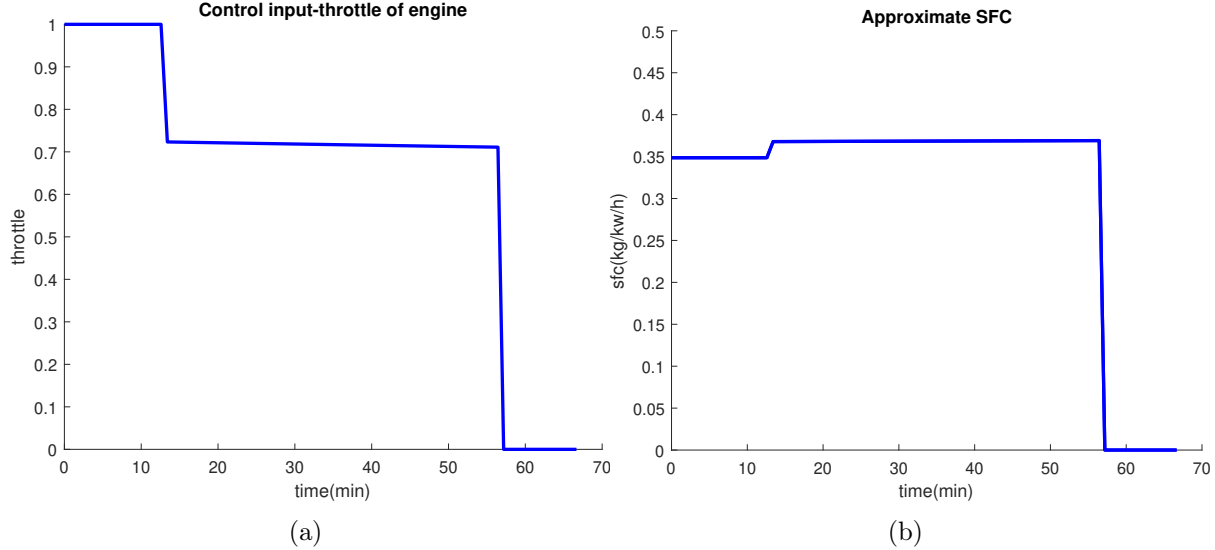


Figure 4.16: (a) Control input; (b) Approximate Specific Fuel Consumption.

solution as well, a technique that proves instrumental to address the question posed at the beginning of this section.

#### 4.3.3 Comparison of two parallel configurations

The mechanical connection between the engine and the electric motor in the HEA propulsion system enables the engine to charge the battery pack in flight. During the climb phase, the power demand is usually greater than the engine's maximum output power; consequently, the propulsion system usually operates in the combined mode. The power-split mode is often applicable during the cruise and descent phases. The fuel consumption during the cruise phase is compared between charging and not charging the battery. The second potential advantage of charging the battery in flight is that the electric motor can operate in the OEI mode. Two scenarios—when the battery pack has sufficient capacity onboard or is fully charged at the beginning of the cruise phase—are compared.

*To Charge or not in-flight during the cruise phase*

First, fuel consumption during the cruise phase is compared between charging and not charging the battery pack. By solving Problem 6 with the extra constraint  $\dot{q} \leq 0$ , the optimal fuel consumption can be determined when charging the battery pack during the flight is not allowed (only positive current can flow through the battery pack). In this direction, all other conditions and constraints are assumed to remain unchanged.

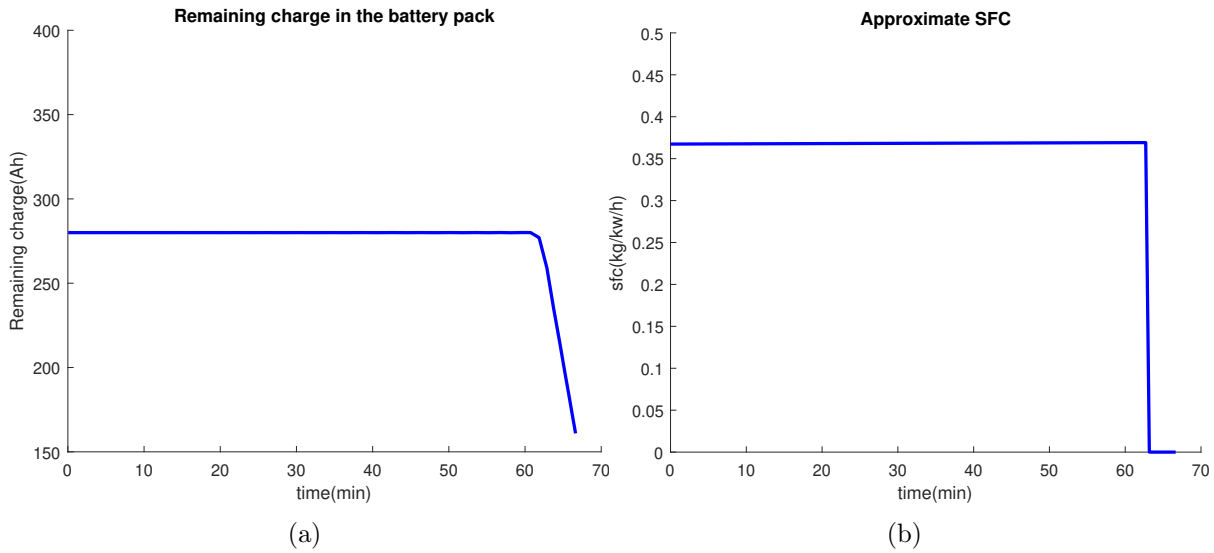


Figure 4.17: (a) Remaining charge in the battery pack; (b) Approximate Specific Fuel Consumption.

Observing Fig. 4.17, when charging the battery during the flight is not allowed, the optimal power distribution strategy yields an “engine-alone” then “motor-alone” structure. The total amount of fuel consumed is 311.08 kg, which is only 0.33 kg more than the case when charging the battery is allowed in flight. Comparing the first segment of Fig. 4.16b and Fig. 4.17b, it is observed that when charging the battery on  $[0, \hat{t}_1]$  in Fig. 4.16b, the SFC is about 0.35 kg/kw/h, which is less than the case when the battery was not being charged ( $0.367 - 0.369$  kg/kw/h) in Fig. 4.17b. However, after fully charging the battery, the aircraft will again operate in the engine alone mode, where the SFC is about  $0.367 - 0.369$  kg/kw/h in Fig. 4.16b, the same as when charging is not permissible.

In addition to this numerical example, Monte Carlo studies facilitate generating different flight

profiles and allow comparing the respective fuel consumption between charging and not charging the battery pack during flight. As these studies show, the maximum amount of fuel saved by charging the battery during flight is rather minimal, namely, 0.82 kg.

Charging the battery during flight can improve the efficiency of the engine, but the duration of this enhanced performance depends on the initial and terminal constraints of the battery pack. After fully charging the battery, the engine will return to its inefficient operational region. In fact, overall, the fuel savings by charging the battery to steer the engine to operate more efficiently are rather negligible.

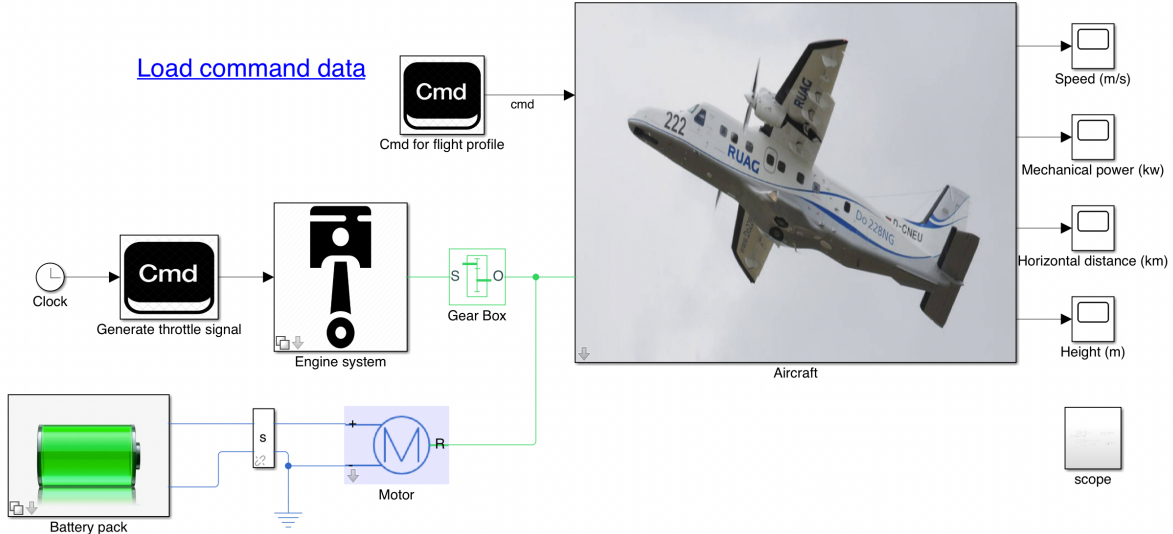


Figure 4.18: HEA Simulink model

In §3.5, we developed a Simulink Project-based environment to validate the energy management algorithms for an AEA; in this section, a similar Simulink environment for HEA has been developed, as shown in Fig. 4.18. A key feature of this simulation environment is its reconfigurability. The new “Engine system” block contains two types of engines: the ICE (for the SOUL aircraft model) and the turbine engine. Fig. 4.19 depicts the turbine engine. The optimization approach detailed previously results in the command signal to the Simulink model, and the corresponding fuel consumption for the charging and not charging cases is computed. In the Simulink model, fuel consumption is proportional to the combustor’s input heat signal. For the charging case, the fuel consumed is

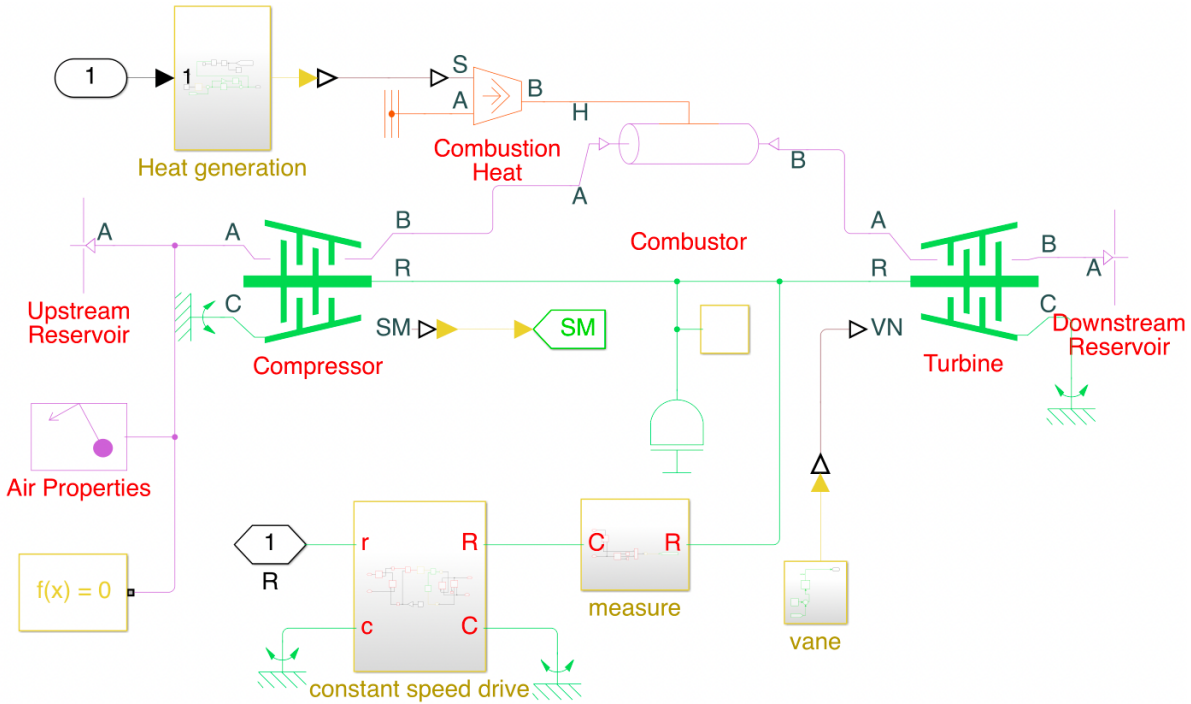


Figure 4.19: Turbine engine.

377.67 kg, whereas, for the not charging case, the fuel consumed is 377.63 kg. The corresponding time histories for the fuel consumption are shown in Fig. 4.20; the fuel consumption rate between 10 and 60 minutes is slightly different, but the total quantity of fuel consumed is nearly identical.

#### *Increase battery pack capacity onboard*

The second potential benefit of charging the battery is that it enables the electric motor to operate in the OEI mode. To achieve this advantage, the electrical path must contain sufficient energy to allow the aircraft to land safely at the nearest airport in case of engine failure. Therefore, the battery pack must have sufficient capacity onboard or be fully charged at the beginning of the cruise phase. These two scenarios are compared based on the total fuel consumption for the climb and cruise phases when the corresponding take-off weights are different due to different battery pack configurations. In the preceding section, it was assumed that the battery pack had two parallel paths with a total capacity of 400 Ah. Each parallel path in the battery pack has a 200 Ah capacity

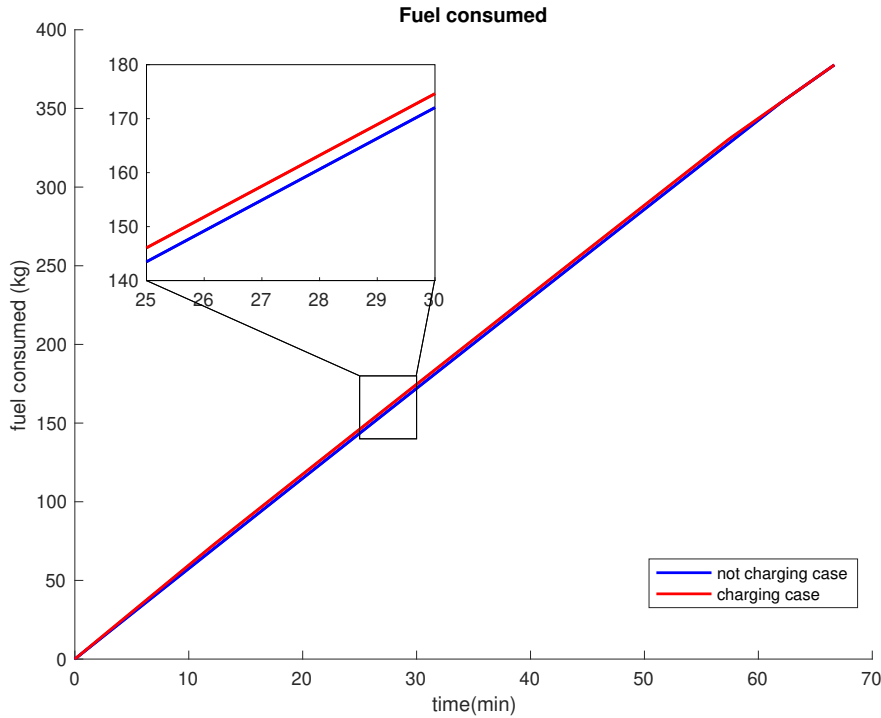


Figure 4.20: Simulink generated time history for the fuel consumption.

and weighs 600 kg. Different battery pack configurations are achieved by adjusting the number of parallel paths. Adding or removing parallel paths has no effect on the output voltage of the battery pack; it only increases or decreases the total capacity. First, fuel consumption during the climb phase with a fixed flight path angle is computed, and the terminal condition for the climb phase is when the altitude reaches 3000 m.

Table 4.1: Fuel consumption of the climb phase with different battery pack configurations.

Number of parallel paths	1	2	3
Total capacity of the battery pack (Ah)	200	400	600
MTOW (kg)	5785	6385	6985
SOC after climb	0.38	0.69	0.79
Remaining charge (Ah)	76	276	474
Fuel consumed during climbing (kg)	32.84	37.55	42.02

Table 4.1 shows that when the difference in take-off weight is 1200 kg, the difference in fuel

consumption is only 10 kg (between one path and three paths). Optimal power allocation solutions indicate that during the climb phase, the electric motor operates at its maximum output power while the engine operates in accordance with the power demand.

For the cruise phase, we compare the following cases:

1. case 1:  $Q = 200$  Ah,  $m_0 = 5750$  kg,  $\theta_0 = 0.4$ ,  $\theta_f = 1$ ;
2. case 2:  $Q = 400$  Ah,  $m_0 = 6350$  kg,  $\theta_0 = 0.7$ ,  $\theta_f = 1$ ;
3. case 3:  $Q = 400$  Ah,  $m_0 = 6350$  kg,  $\theta_0 = 0.7$ ,  $\theta_f = 0.5$ , and the engine cannot charge the battery;
4. case 4:  $Q = 600$  Ah,  $m_0 = 6950$  kg,  $\theta_0 = 0.8$ ,  $\theta_f = 0.67$ , and the engine cannot charge the battery.

It is assumed that cases 1 and 2 have the connected architecture; hence, the engine can charge the battery in-flight. The battery pack should be fully charged after the climb phase to make sure there is sufficient electrical energy for the aircraft landing safely. Cases 3 and 4 have independent architectures, and the battery packs have sufficient capacity during the cruise phase. Then the cruise phase ranging from 150 km to 400 km is swept to compute the fuel consumption for the four cases listed above. The cruise speed is fixed as 80 m/s for all cases. The simulation result is given in Fig. 4.21.

It is observed that the fuel consumption is nearly a linear function of the flight distance for each case (with different slopes). The sensitivity derivative shows that the derivative of the objective function with respect to the terminal time  $\hat{t}_f$  is a constant value, but this value changes slightly as the terminal time changes. For example, in case 2,  $\frac{dG}{dt_f} = 0.6498$  when  $t_f = 0.375$ ;  $\frac{dG}{dt_f} = 0.6363$  when  $\hat{t}_f = 1$ ; this value decreases as the final time  $\hat{t}_f$  increases. In the simulation result, the slope of the red line in Fig. 4.21 is 0.6433. Reference [105] provides an explicit formula for computing the sensitivity derivatives, namely,

$$\begin{bmatrix} \frac{d\mathbf{x}^p}{dp} \\ \frac{d\rho^p}{dp} \end{bmatrix} = - \begin{bmatrix} L_{\mathbf{xx}} & \Phi_{\mathbf{x}}^* \\ \Phi_{\mathbf{x}} & \mathbf{0} \end{bmatrix} \begin{bmatrix} L_{\mathbf{x}p} \\ \Phi_p \end{bmatrix}, \quad (4.41)$$

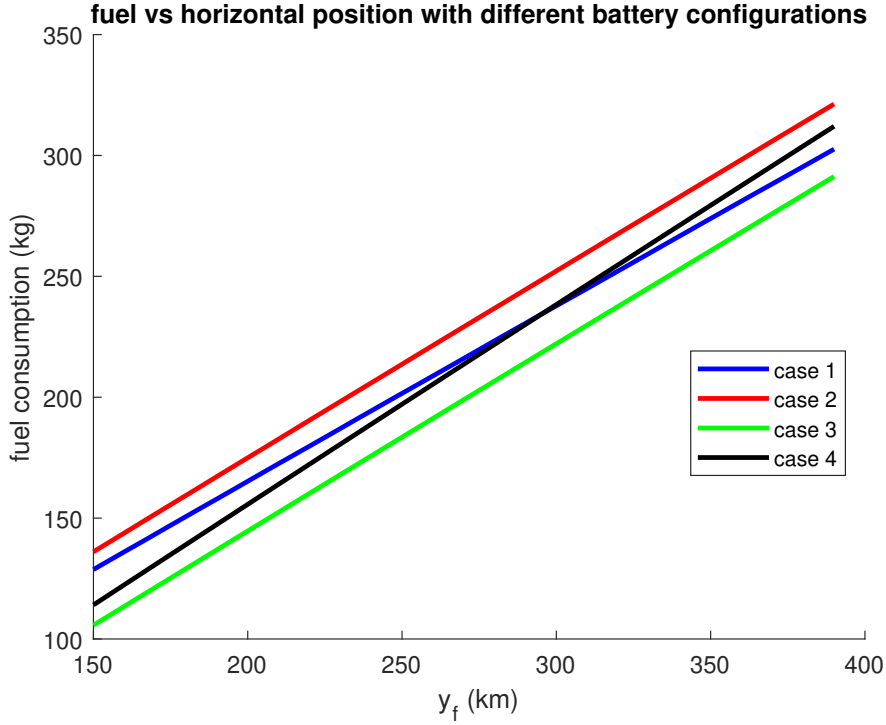


Figure 4.21: Fuel consumption with different battery configurations; cases 1 and 2 are connected configurations; cases 3 and 4 are independent configurations.

where  $\boldsymbol{x}^p$  and  $\boldsymbol{\rho}^p$  are the optimal and dual variables corresponding to parameter  $p$ . Then, the derivative of the objective function  $G$  with respect to the parameter  $t_f$  is computed as

$$\frac{dG}{dt_f} = \frac{\partial G}{\partial \boldsymbol{x}} \frac{\partial \boldsymbol{x}}{\partial t_f}. \quad (4.42)$$

The following observations are obtained when comparing distinct cases with the same terminal battery charge condition (after charging for the connected case; at beginning of the cruise phase for the independent case):

1. Comparing case 2 and case 3, it is observed that these two scenarios have the same initial aircraft mass and battery pack capacity; the only difference is the terminal condition for the SOC of the battery pack. Case 2 requires the battery to remain in a fully-charged state (400 Ah) after a short period of the cruise flight; case 3 requires the remaining charge in the battery pack to be more than 200 Ah. Simulation results show that case 2 needs about 30 kg

more fuel consumed than case 3 for all flight ranges.

2. Comparing case 1 and case 3 (the blue line and the green line), the remaining charge in the battery pack is 200 Ah for both cases. Even though case 1 has a lighter initial aircraft mass, charging the battery to its fully-charged state requires more fuel; carrying more battery packs can save fuel under this remaining charge condition.
3. Comparing case 2 and case 4, same as the comparison between case 1 and case 3; the remaining charge in the battery pack is 400 Ah for both cases. Increase the battery capacity onboard can still save fuel.

Hence, with the same remaining battery charge requirement, increasing the battery capacity onboard is more favorable than charging the battery in-flight in terms of fuel saving and CO<sub>2</sub> emissions.

Similarly, the sensitivity derivative of the objective function with respect to the initial weight can be computed as,

$$\frac{dG}{dm_0} = \frac{\partial G}{\partial \mathbf{x}} \frac{\partial \mathbf{x}}{\partial m_0}. \quad (4.43)$$

The corresponding value turns out to be minimal for the proposed aircraft. For example,  $\frac{dG}{dm_0} = 0.0216$  at  $m_0 = 6350$  kg when the flight conditions are set as  $y_d = 400$  km,  $v = 80$  m/s,  $\theta_0 = 0.7$ ,  $\theta_f = 0.4$ ; as the initial weight increases (the battery capacity remain constant as 400 Ah),  $\frac{dG}{dm_0}$  increases slightly,  $\frac{dG}{dm_0} = 0.0222$  at  $m_0 = 6540$  kg. The fuel consumption only increases by 4.38 kg when the initial weight increases from 6350 kg to 6550 kg. Then flight profiles from the previous section (Monte Carlo) are simulated, and the maximum fuel consumption difference is 6.61 kg between initial weight 6350 kg and 6550 kg. As such, the fuel consumption during the cruise phase is rather insensitive to the initial weight.

## Chapter 5

### **VERTIPORT SELECTION AND TASK ASSIGNMENT FOR UAM**

The development of Urban Air Mobility (UAM) encompasses a wide range of research domains, spanning aircraft technology, infrastructure construction, autonomous operations, regulatory considerations, public acceptance, and more. Within the framework of this dissertation, Chapters 3 and 4 primarily focus on electrically propelled fixed-wing aircraft, which are particularly well-suited for Regional Air Mobility (RAM) operations. Simultaneously, significant ongoing advancements are occurring in the area of electric Vertical Takeoff and Landing (eVTOL) aircraft and related technologies.

Numerous companies and startups, including established aerospace manufacturers, are actively engaged in the research and development of eVTOL. Some notable examples include companies like Ehang, Joby Aviation, Volocopter, Lilium, Airbus, Boeing, and many others. For example, Ehang's unmanned aerial vehicle, EH216-S, has completed all of its planned tests and flights and was certified by the Civil Aviation Administration of China in August 2023. Joby Aviation has received a Special Airworthiness Certificate from the FAA for the first aircraft built at its Pilot Production Line in Marina, California.

In addition, a number of UAM industries, including Ferrovial, Urban-Air Port Ltd., and Skysports, are actively investigating the possibility of ultra-compact, rapidly deployable, multifunctional vertiports for both manned and unmanned aircraft around the world. An illustrative embodiment of this endeavor is the Air-One vertiport, an innovation designed and realized by Urban-Air Port in Coventry, UK. Anticipated to be operational in 2025, Air-One represents a pioneering initiative intended to offer comprehensive services for eVTOLs and drones.

Furthermore, to enable the successful deployment of AAM systems, pivotal regulatory entities such as the FAA in the United States and the European Union Aviation Safety Agency (EASA) in Europe are working closely with industry stakeholders. Their collaboration addresses critical aspects such as safety, certification, airspace integration, and infrastructure requirements, shaping

the frameworks and standards for AAM operations.

Within this landscape of research opportunities and challenges, this dissertation focused on two topics specifically: the optimal selection of vertiports to enhance overall traffic performance in a city and the task allocation and route design for eVTOLs to maximize airline profits. These investigations contribute valuable insights to the growing field of UAM and can help inform decision-making in future UAM implementations.

This chapter is organized as follows. Related works for the vertiport selection problem, fundamental network concepts, and traffic equilibria are introduced in §5.1. The mixed-integer linear program is formulated in §5.2, along with a numerical example in the city of Anaheim. §5.3 provides related works for task assignment problems. §5.4 presents the task network formulation, the mixed-integer program for identifying multiple paths, and a numerical example of assigning tasks to multiple vehicles.

## **5.1 Related works for vertiport selection and traffic equilibria**

### *5.1.1 Related work*

Transportation network design involves the optimal modification of an existing ground transportation network [106, 107]. These modifications encompass expanding the capacity of existing links or introducing new links to the network. The quality of the modifications is assessed based on factors such as traveler congestion in the modified network and the costs associated with the modifications.

The input of the problem includes, *a*) The existing transportation network topology, *b*) Travel demand between each origin-destination pair for a specific time interval, *c*) Road characteristics, such as flow capacity and free travel time, *d*) A set of candidate options for modifications and their cost, *e*) The overall budget for modifications. The outcome of the problem is a set of modifications that satisfies the budget constraint and minimizes the congestion of travelers. [108] provides a survey on recent transportation network design.

One crucial aspect in the design of the transportation network involves the prediction of the collective behavior of selfish travelers in congested transportation networks [109]. Two distinct prediction models have been used in the literature. The first model, referred to as the Beckmann

model [110], involves the minimization of a convex polynomial function subject to linear constraints. The second model, known as the Nesterov & de Palma model [111, 112], entails the minimization of a linear function subject to linear constraints. When combined with the Bureau of Public Roads function for link delays, the Beckmann model provides prediction results similar to the Nesterov & de Palma model in terms of user distribution, the price of anarchy, and the Braess paradox phenomenon. We refer interested readers to [113] for a detailed numerical comparison of the two models.

The Nesterov & de Palma model exhibits superior computational efficiency compared to the Beckmann model. The reason is that a network design problem requires not only the prediction of traffic patterns but also the optimization of the predicted traffic patterns by designing the network parameters. The former task just involves the resolution of a convex optimization problem, while the latter presents a nonconvex optimization problem that encompasses the Karush–Kuhn–Tucker (KKT) conditions of a convex optimization problem [107]. Due to the polynomial objective function, the KKT conditions—in particular, the vanishing gradient condition—of the Beckmann model include polynomial equalities [107]. On the other hand, the KKT conditions in the Nesterov & de Palma model include only linear equalities and inequalities [114]. As a result, using the Nesterov & de Palma model, the network design optimization is equivalent to a mixed integer linear program (MILP) [114, 115, 116]. In contrast, using the Beckmann model, solving a MILP—or equivalently, a linear-linear bilevel optimization problem—only provides a local descent direction, not a globally optimal solution, for the network design optimization [117].

### 5.1.2 Hybrid ground-air transportation networks formulation

We introduce some fundamental network concepts, including nodes, links, incidence matrices, link and node capacities, and travel time.

#### *Nodes and links*

Let  $\mathcal{N} = \{1, 2, \dots, n_n\}$  represent the set of nodes in the ground transportation network. Among all these nodes,  $\mathcal{V} = \{v(1), v(2), \dots, v(n_v)\}$  comprises the nodes that contain a candidate vertiport location, where  $v(i) \in \mathcal{N}$  for all  $i = 1, 2, \dots, n_v$ . Let  $\mathcal{L} = \{1, 2, \dots, n_l\}$  denote the set of links. Each

link is an ordered pair of distinct nodes, where the first and second nodes are referred to as the “tail” and “head” of the link, respectively.

Furthermore,  $n_g \leq n_l$  denotes the number of ground links, and  $n_a := n_l - n_g$  denotes the number of air links. A ground link  $k = (i, j)$  with  $1 \leq k \leq n_g$  indicates that any ground travelers can travel from node  $i$  to node  $j$ , and an air link  $k = (i, j)$  with  $n_g + 1 \leq k \leq n_l$  means any aircraft can fly from node  $i$  to node  $j$ .

### *Incidence matrices*

The topology of the hybrid ground-air network is represented by the node-edge incidence matrix, denoted as  $E \in \mathbb{R}^{n_n \times n_l}$ . The entry  $[E]_{ik}$  in matrix  $E$  corresponds to the relationship between node  $i$  and link  $k$  is defined as follows:

$$[E]_{ik} = \begin{cases} 1, & \text{if node } i \text{ is the tail of link } k, \\ -1, & \text{if node } i \text{ is the head of link } k, \\ 0, & \text{otherwise.} \end{cases} \quad (5.1)$$

Note that  $[E]_{ik} \neq 0$  for some  $n_g + 1 \leq k \leq n_l$  only if  $i \in \mathcal{V}$ .

The topology of the vertiports and air links is represented by the following *unsigned incidence matrix*  $D \in \mathbb{R}^{n_v \times n_l}$  for air links. The entry  $[D]_{ik}$  is associated with node  $i$  and link  $k$  as follows

$$[D]_{ik} = \begin{cases} 1, & \text{if } k \geq n_g + 1 \text{ and } [E]_{v(i),k} \neq 0, \\ 0, & \text{otherwise.} \end{cases} \quad (5.2)$$

### *Demand matrix*

We distinguish different travelers in the network using their destinations, denoted by a subset of nodes  $\{s(1), s(2), \dots, s(n_d)\} \subset \mathcal{N}$ . These nodes represent the various destination points in the hybrid network. A *demand matrix*  $S \in \mathbb{R}^{n_n \times n_d}$  is introduced to represent the *traffic demand*, which represents the number of trips per unit between different origin and destination nodes. The matrix  $S$  is defined as follows: for any  $i \in \mathcal{N}$  with  $i \neq s(j)$ , the entry  $[S]_{ij}$  in matrix  $S$  denotes the traffic demand from node  $i$  to node  $s(j)$ , *i.e.*, the number of travelers leaving node  $i$  heading towards node

$s(j)$  per unit time. If  $[S]_{ij} > 0$ , then  $(i, s(j))$  is also known as an *origin-destination pair*. To ensure that the total flow is conserved,  $[S]_{s(j),j} = -\sum_{i,i \neq s(j)} [S]_{ij}$  for all  $j = 1, 2, \dots, n_d$  is defined such that the sum of each column in matrix  $S$  equals zero, enabling convenient definition of flow conservation constraints in matrix form.

### Flow matrix

At a static traffic equilibrium, the number of travelers entering and exiting the same link is balanced. The number of travelers on different links per unit of time is represented by the *flow matrix*  $X \in \mathbb{R}^{n_l \times n_d}$ . Specifically, the entry  $[X]_{kj}$  in matrix  $X$  denotes the amount of travelers exiting link  $k$  while heading towards destination node  $s(j)$  per unit time.

### Flow conservation

By construction, the demand matrix  $S$ , flow matrix  $X$ , and incidence matrices  $E$  together satisfy the following *flow conservation constraint*:

$$EX = S, \quad X \geq 0. \quad (5.3)$$

Note that the above constraints implicitly imply that the sum of each column in matrix  $S$  equals zero. This observation justifies the definition of the negative entries in matrix  $S$ .

**Example 1.** Consider the example network in Fig. 5.1, where black and blue arcs denote ground and air links, respectively. The blue nodes contain candidate locations for vertiports. In this case, we have  $\mathcal{N} = \{1, 2, 3, 4\}$ ,  $\mathcal{V} = \{2, 3\}$ ,  $\mathcal{L} = \{1, 2, 3, 4, 5, 6\}$ , and matrices  $E$  and  $D$  are as follows

$$E = \begin{bmatrix} 1 & 1 & 0 & 0 & 0 & 0 \\ -1 & 0 & 1 & 0 & 1 & -1 \\ 0 & -1 & 0 & 1 & -1 & 1 \\ 0 & 0 & -1 & -1 & 0 & 0 \end{bmatrix}, \quad D = \begin{bmatrix} 0 & 0 & 0 & 0 & 1 & 1 \\ 0 & 0 & 0 & 0 & 1 & 1 \end{bmatrix}.$$

Furthermore, a possible choice of demand matrix  $S$  and flow matrix  $X$  that satisfy the constraints

in Eq.(5.3), are as follows:

$$S = \begin{bmatrix} 5 & -5 & 0 & 0 \\ 10 & 0 & 0 & -10 \end{bmatrix}^\top, \quad X = \begin{bmatrix} 5 & 0 & 0 & 0 & 0 & 0 \\ 3 & 7 & 7 & 3 & 0 & 4 \end{bmatrix}^\top.$$

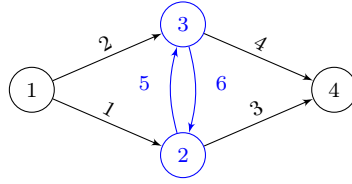


Figure 5.1: An example of a hybrid ground-air transportation network

#### Capacity and free travel time

The *link capacity* of a ground or air link represents the maximum amount of travelers that can exist on the link per unit of time. For ground links, this capacity depends on the number of lanes and cycle time of traffic signals; for air links, the capacity depends on the available airspace and the maximum allowed aircraft density of each flight leg. We denote the link capacity of all the air and ground links using the *link capacity vector*  $f \in \mathbb{R}_+^{n_l}$ , where its entry  $[f]_k$  denotes the capacity of link  $k$ .

The *free travel time* of a ground or air link represents the time consumed by each traveler to traverse the link when no traffic congestion is present. We denote the free travel time of all links using a vector  $c \in \mathbb{R}^{n_l}$ , where the  $k$ -th entry denotes the free travel time on link  $k$ .

The Nesterov & de Palma model [111, 112] establishes a coupling between the link capacity, the free travel time, and the flow matrix as follows: First, the traffic flow on each link should never exceed its capacity, *i.e.*,

$$\sum_{j=1}^{n_d} [X]_{kj} \leq [f]_k, \quad \forall k \in \mathcal{L} \tag{5.4}$$

Second, the travel time on a link is determined based on its flow relative to its capacity. If the traffic flow on a link is below its capacity, then the travel time of this link remains equal to the corresponding free travel time. If the traffic flow on a link equals its capacity, then the average travel time of this link is lower bounded by the corresponding free travel time. In other words, if

vector  $\tilde{c} \in \mathbb{R}^{n_l}$  is such that  $[\tilde{c}]_k$  denotes the travel time on link  $k$ , then the following conditions hold for all  $k \in \mathcal{L}$ :

$$\sum_{j=1}^{n_d} [X]_{kj} < [f]_k \Rightarrow [\tilde{c}]_k = [c]_k, \quad (5.5a)$$

$$\sum_{j=1}^{n_d} [X]_{kj} = [f]_k \Rightarrow [\tilde{c}]_k \geq [c]_k. \quad (5.5b)$$

In addition to the link capacity, we also consider the additional capacity of vertiports in the hybrid ground-air transportation network. Each vertiport has a limited number of touch-down and lift-off pads, which restricts the maximum amount of take-off and landing operations per unit of time. Similar to those in the Nesterov & de Palma model, we make the following assumptions. First, the total air traffic entering and exiting a vertiport should never exceed its capacity, *i.e.*,

$$\sum_{k=1}^{n_l} \sum_{j=1}^{n_d} [D]_{ik} [X]_{kj} \leq [g]_i, \quad \forall i = 1, 2, \dots, n_v. \quad (5.6)$$

Second, the delay at a vertiport depends on the flow relative to its capacity. If the traffic flow on a vertiport is below its capacity, then the delay at this vertiport is zero; if the traffic flow on a vertiport reaches its capacity, then the average flight delay at this vertiport is nonnegative. In other words, if vector  $\tilde{e} \in \mathbb{R}^{n_v}$  is such that  $[\tilde{e}]_i$  denote the average flight delay at vertiport  $i$ , then the following condition holds for all  $i = 1, 2, \dots, n_v$ :

$$\sum_{k=1}^{n_l} \sum_{j=1}^{n_d} [D]_{ik} [X]_{kj} < [g]_i \Rightarrow [\tilde{e}]_i = 0, \quad (5.7a)$$

$$\sum_{k=1}^{n_l} \sum_{j=1}^{n_d} [D]_{ik} [X]_{kj} = [g]_i \Rightarrow [\tilde{e}]_i \geq 0. \quad (5.7b)$$

In practice, link and node capacities are defined in terms of the number of ground or air vehicles rather than the number of travelers or passengers in the vehicles. Hence, the value of the link and node capacities above often depends on the average number of passengers per ground vehicle and air vehicle. The latter increases, for example, with the capacity of the vehicle and the average level of ridesharing.

**Remark 2.** Several studies in the literature have considered the link capacity constraints (Eq.(5.4)) in ground transportation network models [118], including the Beckmann model [119] and the Nesterov & de Palma model [111, 112]. We refer interested readers to [113] for a detailed numerical comparison of the effects of these constraints in different transportation models.

### 5.1.3 Traffic equilibria with node and link capacities

The concept of *static equilibrium matrix* is introduced for subsequent mathematical model formulation.

**Definition 1.** Matrix  $X \in \mathbb{R}^{n_l \times n_v}$  is a static equilibrium matrix defined by the tuple  $\{S, E, D, c, f, g\}$  if it optimizes the following linear program,

$$\begin{aligned} & \min_X c^\top X \mathbf{1}_d \\ & \text{s.t } EX = S, \quad X \geq 0, \\ & \quad X \mathbf{1}_d \leq f, \quad DX \mathbf{1}_d \leq g. \end{aligned} \tag{5.8}$$

**Remark 3.** Optimization (5.8) augments the multicommodity min-cost flow problem [120, Chp. 4] with additional node capacity constraints. The main difference between optimization (5.8) and previous work on the Nesterov & de Palma model for ground traffic [111, 112] is that optimization (5.8) contains the vertiport capacity constraints in Eq.(5.6), which, unlike the link capacity well-studied in the literature, are defined on the nodes of the network rather than the links.

The linear program in Definition 1 is our prediction model for the traffic patterns—including flow and travel cost—of a hybrid ground-air transportation network. The following proposition provides two equivalent characterizations of static equilibrium matrix based on the optimality condition of linear programs.

**Proposition 1.** Matrix  $X \in \mathbb{R}^{n_l \times n_v}$  is a static equilibrium matrix associated with the tuple  $\{S, E, D, c, f, g\}$  if and only if there exists  $V \in \mathbb{R}^{n_n \times n_d}$ ,  $U \in \mathbb{R}^{n_l \times n_d}$ ,  $p \in \mathbb{R}^{n_l}$ , and  $q \in \mathbb{R}^{n_v}$  such that the following two conditions hold simultaneously:

1. The following constraints are satisfied:

$$EX = S, \quad X\mathbf{1}_d \leq f, \quad DX\mathbf{1}_d \leq g, \quad (5.9a)$$

$$(c + p + D^\top q)\mathbf{1}_d^\top = E^\top V + U, \quad (5.9b)$$

$$X \geq 0, \quad U \geq 0, \quad p \geq 0, \quad q \geq 0. \quad (5.9c)$$

2. One of the following two sets of constraints are satisfied:

either

$$\begin{aligned} \text{tr}(X^\top U) &= 0, \quad p^\top X\mathbf{1}_d = f^\top p, \\ q^\top DX\mathbf{1}_d &= g^\top q, \end{aligned} \quad (5.10)$$

or

$$c^\top X\mathbf{1}_d + f^\top p + g^\top q = \text{tr}(V^\top S). \quad (5.11)$$

*Proof.* See Appendix B.1 □

The conditions in Eq.(5.10) and Eq.(5.11) are also known as the *complementary slackness condition* and the *zero-duality-gap condition*. For linear programs, these two conditions are equivalent [121, Thm. 1.3.3]. Both conditions will be used to define and simplify the mathematical program with equilibrium constraints for vertiport selection.

Let  $\tilde{c} = c + p$  and  $\tilde{e} = q$ . One can verify that the conditions in Eqs.(5.9a, 5.9c, and 5.10) together imply the constraints in Eq.(5.3, 5.4, 5.6, 5.5, and 5.7). Hence, the equilibria model in Definition 1 satisfies the second and the third assumptions we introduced at the beginning of this section.

Furthermore, the conditions in Proposition 1 also imply that only routes with the minimum accumulated travel time are used, a property known as the Wardrop equilibrium principle [122]. To see this implication, we define the set of *route vectors* from node  $i$  to destination node  $s(j)$  as follows:

$$\mathcal{P}(i, s(j)) = \left\{ u \in \{0, 1\}^{nl} \middle| \begin{array}{l} [Eu]_i = 1, [Eu]_{s(j)} = -1, \\ [Eu]_k = 0, \forall k \neq i, s(j). \end{array} \right\}. \quad (5.12)$$

Intuitively, each vector  $u$  in set  $\mathcal{P}(i, s(j))$  defines a sequence of links connecting node  $i$  and node  $s(j)$  in a head-to-tail fashion; link  $k$  is on the route defined by  $u$  if and only if  $[u]_k = 1$ . Note that

the set  $\mathcal{P}(i, s(j))$  is not necessarily a singleton since there can be multiple routes—routes composed of ground links, air links, or a combination of both—between each origin-destination pairs.

Based on the above definition, the following corollary shows that any tuple  $\{X, U, V, p, q\}$  satisfying the conditions in Proposition 1 implies that any used routes have the lowest accumulated travel time, where the travel time of link  $k$  is given by  $[c + p + Dq]_k$ .

**Corollary 1.** *Let  $\{X, U, V, p, q\}$  satisfy the conditions in (5.9) and Eq.(5.10), and  $\bar{c} := c + p + Dq$ . Let  $i \in \{1, 2, \dots, n_n\}$  and  $j \in \{1, 2, \dots, n_d\}$  such that  $i \neq s(j)$  and  $[S]_{i,s(j)} > 0$ . If  $u^* \in \mathcal{P}(i, s(j))$  and  $[X]_{kj} > 0$  for all  $k$  such that  $[u^*]_k = 1$ , then the following condition holds for all  $u \in \mathcal{P}(i, s(j))$ :*

$$\bar{c}^\top u^* \leq \bar{c}^\top u. \quad (5.13)$$

Corollary 1 shows that the equilibria model in Definition 1 also satisfies the first assumption we introduced at the beginning of this section: any routes with positive traffic flow have the lowest accumulated time of travel.

Alternatively, one can predict the traffic equilibria using an extension of the Beckmann model rather than an extension of the Nesterov & de Palma model [119]. However, the Beckmann model results in a set of equilibrium conditions with more nonlinear equality constraints than those in Nesterov & de Palma model [106, 107]: the equilibrium conditions in the Beckmann model are the KKT conditions of a nonlinear convex optimization, which contain nonlinear constraints; in contrast, the equilibrium conditions in the Nesterov & de Palma model, as we showed in Proposition 1, only contain linear constraints. On the other hand, studies have shown that the Nesterov & de Palma model and the Beckmann model give similar prediction results [113]. Therefore, we chose the Nesterov & de Palma model as the basis of our equilibria model.

## 5.2 Groud-Air hybrid transportation network design

In this section, we first formulate the vertiport selection problem as a mixed integer linear program, then we implement this approach to an actual city's transportation network.

### 5.2.1 Mixed-integer linear programming

We first introduce a mathematical model that selects the location and capacity of vertiports in a hybrid ground-air transportation network to optimize the resulting traffic equilibria. In particular, we aim to modify the optimal solution of the linear program (5.8) by choosing the entries in the vertiport-capacity vector  $g$  among discrete values—including zero values, in which case the corresponding vertiport location is discarded. The following assumption is made for linear program (5.8).

**Assumption 6.** *Linear program (5.8) is feasible and has a bounded optimal value.*

Assumption 6 implies that link capacity and vertiport capacity in the hybrid air-ground transportation network are large enough to accommodate the traffic demand, *i.e.*, the flow conservation constraints in (5.3) and capacity constraints in Eq.(5.4) and Eq.(5.6) hold simultaneously. Based on this assumption, we define the objective function and a mathematical program with equilibrium constraints (MPEC) for vertiport selection problem.

#### MPEC key components

We first introduce key components to define the MPEC, such as the design variables, the objective function, and the constraints.

The following assumption is made for the vertiport capacity vector  $g$ .

**Assumption 7.** *There exists  $G \in \mathbb{R}_+^{n_v \times n_c}$  such that the vertiport capacity vector  $g$  in Definition 1 satisfies the following constraints:*

$$[g]_i \in \{0, [G]_{i1}, [G]_{i2}, \dots, [G]_{i,n_c}\},$$

where  $[G]_{i1} < [G]_{i2} < \dots < [G]_{i,n_c}$  for all  $i = 1, 2, \dots, n_v$ .

Assumption 7 states that the capacity of the  $i$ -th vertiport is selected from an increasing sequence  $\{0, [G]_{i1}, [G]_{i2}, \dots, [G]_{i,n_c}\}$ . For example, if  $n_c = 3$ , then the capacity of the  $i$ -th vertiport can be zero—in this case, this vertiport is discarded—or a small, medium, or large value, denoted by  $[G]_{i1}$ ,  $[G]_{i2}$ , and  $[G]_{i3}$ , respectively.

Based on Assumption 7, the *selection matrix* is defined as follows. Let  $B \in \mathbb{R}^{n_v \times n_c}$  be a binary matrix such that  $[g]_i = [G]_{ij}$  if and only if  $[B]_{ij} = 1$ . Then Assumption 7 holds if and only if

$$g = (B \odot G)\mathbf{1}_c, \quad B\mathbf{1}_c \leq \mathbf{1}_v, \quad B \in \{0, 1\}^{n_v \times n_c}. \quad (5.14)$$

In other words, each choice of  $B$  that satisfies the constraints in (5.14) corresponds to a value of capacity vector  $g$  that satisfies Assumption 7. The binary matrix  $B$  is used as a design variable in the vertiport selection problem.

With the design variable  $B$  and Assumptions 6 and 7, the objective function for the vertiport selection problem can be defined as follows. Given a set of vertiport with corresponding capacity, we first introduce a quantitative measure for the quality of the traffic equilibria. To this end, given a selected capacity vector  $g$ , let  $\{X, U, V, p, q\}$  be a tuple that satisfies the equilibrium conditions in Proposition 1. The quality of this tuple is evaluated by the following *network loading function*:

$$\ell(X, p, q) := (c + p + D^\top q)^\top X \mathbf{1}_d = \sum_{k=1}^{n_l} \underbrace{[c + p + D^\top q]_k}_{\bar{c}_k} \underbrace{[X \mathbf{1}_d]_k}_{\bar{x}_k}. \quad (5.15)$$

Here the value of  $\bar{c}_k$  is the travel time on link  $k$  at the equilibrium: it is the sum of the free travel time  $[c]_k$  and the extra time delay caused by the congestion on the link and nodes, given by  $[p + D^\top q]_k$ . The value of  $\bar{x}_k$  is the total amount of travelers entering or exiting link  $k$  per unit time<sup>1</sup>.

Assumption 7 states that the location and capacity of the vertiports depend on a binary selection matrix  $B$ : if  $\sum_{j=1}^{n_c} [B]_{ij} = 0$ , then vertiport  $i$  is not selected; if  $[B]_{ij} = 1$ , then vertiport  $i$  is selected with capacity  $[G]_{ij}$  at the cost of  $[K]_{ij}$ . In addition, the capacity selection for all the vertiports is subject to a budget constraint defined by parameter  $\gamma$ .

Now we analyze the constraints for the selection problem. The first set of constraints is given in Eqs.(5.9, 5.10) (or Eq.(5.11)) and Eq.(5.14). Together these constraints define the coupling relation among the selection matrix  $B$ , the capacity vector  $g$ , and the static traffic equilibria that correspond to the tuple  $\{X, U, V, p, q\}$ .

In addition, we also consider the following budget and logical constraints on the selection matrix  $B$ . First, constructing and maintaining a vertiport comes at a cost—which typically increases with

---

<sup>1</sup>At a static equilibrium, the number of travelers entering and exiting the same link are the same; see [112].

the vertiport capacity. To impose a budget constraint in the vertiport selection problem, a *cost matrix*  $K \in \mathbb{R}^{n_v \times n_c}$  is introduced, and its entry  $[K]_{ij}$  is the cost of selecting capacity  $[G]_{ij}$  for the  $i$ -th vertiport.  $\gamma \in \mathbb{R}$  denotes the upper bound on the total cost of vertiport selection, then a budget constraint takes the following form:

$$\mathbf{1}_v^\top (K \odot B) \mathbf{1}_c \leq \gamma. \quad (5.16)$$

Second, the choice of vertiport location is often subject to additional logical constraints: for example, two locations close to each other cannot be selected simultaneously due to noise management regulations, and some locations must be selected as an air traffic hub. To account for these logical constraints, we consider the following linear constraints on the selection matrix  $B$

$$A \text{vec}(B) \leq b, \quad (5.17)$$

where  $\text{vec} : \mathbb{R}^{n_v \times n_c} \rightarrow \mathbb{R}^{n_v n_c}$  is a vectorization map such that  $[\text{vec}(B)]_{(i-1)n_v+j} = B_{ij}$  for all  $i = 1, 2, \dots, n_v$  and  $j = 1, 2, \dots, n_c$ ,  $A \in \mathbb{R}^{n_b \times (n_v n_c)}$  and  $b \in \mathbb{R}^{n_b}$  defines all the logical constraints on matrix  $B$ .

**Example 2.** To illustrate the logical constraints on vertiport location, we consider the case with two candidate vertiport locations, and each vertiport has two candidate capacity value, i.e.,  $n_v = n_c = 2$ . In this case, If we let

$$A = \begin{bmatrix} 1 & 1 & 1 & 1 \\ -1 & -1 & -1 & -1 \end{bmatrix}, \quad b = \begin{bmatrix} 1 \\ -1 \end{bmatrix}, \quad (5.18)$$

then the constraint in (5.17) implies that one and only one of the two candidate vertiport location can be selected, i.e.,

$$[B]_{11} + [B]_{12} + [B]_{21} + [B]_{22} = 1. \quad (5.19)$$

### The MPEC formulation

We now introduce the mathematical program that selects the value of capacity vector  $g$ . The idea is to optimally choose the value of vector  $g$  such that the resulting equilibrium minimizes a weighted sum of the network loading function in Eq.(5.15) and the selection cost defined in the left hand side of Eq.(5.16).

**Problem 8.** Find  $g$  such that the following problem is solved,

$$\begin{aligned}
& \underset{\substack{g, B, p, q, \\ X, U, V}}{\text{minimize}} \quad (c + p + D^\top q)^\top X \mathbf{1}_d + \omega \mathbf{1}_v^\top (K \odot B) \mathbf{1}_c \\
& \text{subject to} \quad EX = S, \quad X \mathbf{1}_d \leq f, \quad DX \mathbf{1}_d \leq g, \\
& \quad (c + p + D^\top q) \mathbf{1}_d^\top = E^\top V + U \\
& \quad X \geq 0, \quad U \geq 0, \quad p \geq 0, \quad q \geq 0, \\
& \quad c^\top X \mathbf{1}_d + f^\top p + g^\top q = \text{tr}(V^\top S), \\
& \quad g = (G \odot B) \mathbf{1}_c, \quad B \mathbf{1}_c \leq \mathbf{1}_v, \\
& \quad \mathbf{1}_v^\top (K \odot B) \mathbf{1}_c \leq \gamma, \quad A \text{vec}(B) \leq b, \\
& \quad B \in \{0, 1\}^{n_v \times n_c},
\end{aligned} \tag{5.20}$$

where  $\omega \in \mathbb{R}_+$  is a weighting parameter.

Problem 8 is a *mathematical program with equilibrium constraints* (MPEC): it includes the equilibrium conditions in Eq.(5.9) and Eq.(5.11) as part of its constraints. Proposition 1 shows that these constraints—which jointly depend on the primal and dual variables for linear program (5.8)—together ensure that matrix  $X$  is a static equilibrium matrix in the sense of Definition 1; similar constraints are common in MPEC, see [123, Sec. 7.1]. According to Proposition 2, one can alternatively replace the duality gap constraint in Problem 8—which was first introduced in Eq.(5.11)—with the complementarity constraints in Eq.(5.10). However, such replacement introduces even more bilinear functions of the unknowns. Hence we choose to write optimization in its current form; a similar MPEC was also used in electrified ground network design [114].

A globally optimal solution of Problem 8 is challenging to compute since its objective function and constraints contains bilinear functions of unknowns, such as  $p^\top X \mathbf{1}_d$  and  $g^\top q$ .

We now show that the MPEC in Problem 8, a bilinear mixed integer optimization problem, is equivalent to a MILP. As a result, one can compute a global optimal solution of optimization Problem 8 using off-the-shelf optimization software, such as GUROBI [124].

The first step is to apply the following proposition to replace the bilinear constraints in Problem 8 with a linear one.

**Proposition 2.** Let  $G \in \mathbb{R}_{++}^{n_v \times n_c}$ . There exists a large enough  $\mu \in \mathbb{R}_{++}$  such that the following two sets of conditions are equivalent.

1. There exists  $\delta \in \mathbb{R}$ ,  $q \in \mathbb{R}^{n_v}$ ,  $B \in \{0, 1\}^{n_v \times n_c}$  and  $g \in \mathbb{R}^{n_v}$  such that

$$\delta = g^\top q, \quad g = (G \odot B)\mathbf{1}_c, \quad B\mathbf{1}_c \leq \mathbf{1}_v, \quad q \geq 0. \quad (5.21)$$

2. There exists  $\delta \in \mathbb{R}$ ,  $q \in \mathbb{R}^{n_v}$ ,  $B \in \{0, 1\}^{n_v \times n_c}$  and  $Y \in \mathbb{R}^{n_v \times n_c}$ , such that

$$\begin{aligned} \delta &= \mathbf{1}_v^\top Y \mathbf{1}_c, \quad 0 \leq Y \leq \mu B, \quad B\mathbf{1}_c \leq \mathbf{1}_v, \\ 0 &\leq G \odot (q\mathbf{1}_c^\top) - Y \leq \mu(\mathbf{1}_v \mathbf{1}_c^\top - B), \quad q \geq 0. \end{aligned} \quad (5.22)$$

*Proof.* See Appendix B.3. □

Proposition 2 allows us to replace the bilinear function  $g^\top q$ , appearing in the constraints of Proposition 2, with a linear function of an auxiliary matrix  $Y$ .

Our next step is to show the bilinear objective function of optimization Problem 8 is also equivalent to a linear one. To this end, by using Proposition 1 again we can show the following:

$$p^\top X \mathbf{1}_d = f^\top p, \quad q^\top D X \mathbf{1}_d = g^\top q.$$

Next, using Proposition 2, we can further replace the inner product  $q^\top g$  with a linear function of the auxiliary matrix  $Y$ . By combining these results together, we can replace the bilinear objective function in Problem 8 with a linear one.

Equipped with these results, we can reformulate Problem 8 as the following equivalent MILP.

**Problem 9.** Find  $B$ ,  $Y$ , and tuple  $\{X, U, V, p, q\}$  such that the following problem is solved,

$$\begin{aligned}
 & \underset{\substack{B, p, q, Y, \\ X, U, V}}{\text{minimize}} \quad c^\top X \mathbf{1}_d + f^\top p + \mathbf{1}_v^\top Y \mathbf{1}_c + \omega \mathbf{1}_v^\top (K \odot B) \mathbf{1}_c \\
 & \text{subject to } EX = S, \quad X \mathbf{1}_d \leq f, \quad DX \mathbf{1}_d \leq (G \odot B) \mathbf{1}_c, \\
 & \quad (c + p + D^\top q) \mathbf{1}_d^\top = E^\top V + U \\
 & \quad X \geq 0, \quad U \geq 0, \quad p \geq 0, \quad q \geq 0, \\
 & \quad c^\top X \mathbf{1}_d + f^\top p + \mathbf{1}_v^\top Y \mathbf{1}_c = \text{tr}(V^\top S), \tag{5.23} \\
 & \quad 0 \leq G \odot (q \mathbf{1}_c^\top) - Y \leq \mu(\mathbf{1}_v \mathbf{1}_m^\top - B), \\
 & \quad B \mathbf{1}_c \leq \mathbf{1}_v, \quad \mathbf{1}_v^\top (K \odot B) \mathbf{1}_c \leq \gamma, \\
 & \quad 0 \leq Y \leq \mu B, \quad A \text{vec}(B) \leq b, \\
 & \quad B \in \{0, 1\}^{n_v \times n_c},
 \end{aligned}$$

where  $\mu$  is a large enough positive scalar

Problem 9 is a MILP: its objective function and constraints only depend on linear functions of the unknowns, and it contains a binary unknown matrix  $B$ . One can solve such MILP and obtain a globally optimal solution using off-the-shelf optimization software.

One challenge in solving Problem 9 is to choose an appropriate value for the scalar parameter  $\mu$ . For the equivalence in Proposition 2 to hold, one must choose  $\mu$  to be large enough such that  $\mu$  upper bounds each element in matrix  $G \otimes (q \mathbf{1}_c^\top)$  and matrix  $Y$ . On the other hand, choosing  $\mu$  to be too large can cause slow convergence and memory error when solving Problem 9. This phenomenon is well-known in the mixed integer programming literature. For the guidelines on diagnosing and preventing large values of parameter  $\mu$ , we refer the interested readers to [125, Sec. 3.4].

In practice, one can choose an appropriate value for  $\mu$  by letting  $\mu = \bar{q} \max_i [G]_{i,n_c}$ , where  $\bar{q} \in \mathbb{R}_+$  is an estimate of the maximum delay among all vertiports at equilibrium. One can empirically estimate the magnitude of  $\bar{q}$  using the magnitude of free travel time  $c$ . In our numerical experiments, we find that letting  $\bar{q}$  be one order of magnitudes higher than the value of  $c^\top \mathbf{1}_{n_l}$  usually gives a valid estimate. On the other hand, if  $\mu$  is too small or too large, the MILP in (5.23) will become infeasible or ill-conditioned, and numerical MILP solvers will fail to provide a solution.

### 5.2.2 Numerical results

We demonstrate our algorithm using the Anaheim ground transportation network model developed in [126], which contains more than 400 nodes and 900 links. Our goal is to numerically demonstrate the effects of adding different vertiports to an existing ground transportation network in terms of traffic loading in the network.

The Anaheim ground transportation network model consists of a well-defined arterial grid system integrated with an extensive freeway system. See Fig. 5.2 for an illustration.<sup>2</sup> The model includes the data for 1) the incidence matrix, 2) the demand matrix, 3) the free travel time, and 4) the link capacity. Based on these data, we construct the Nesterov & de Palma model for the ground transportation network, which is known to produce similar results as the Beckmann model [113].

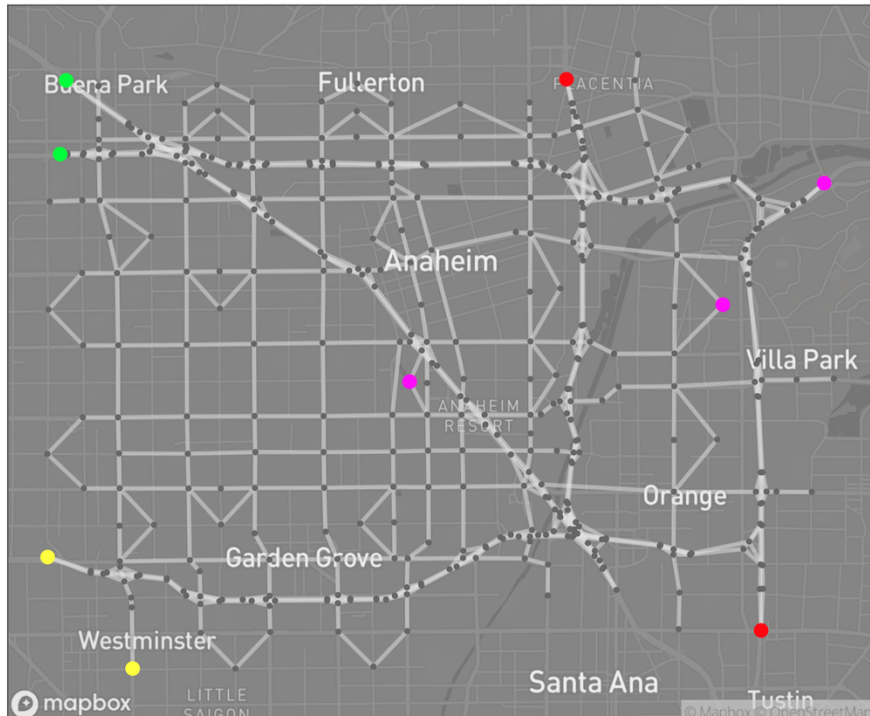


Figure 5.2: The Anaheim network where the candidate vertiport locations are marked with colored circles.

In addition to the Anaheim ground transportation network, we construct an air transportation

---

<sup>2</sup>The map images we used are generated by Mapbox. <https://www.mapbox.com>

network as follows. Based on their location and travel demands, we choose nine different destination nodes in the Anaheim network as candidate locations for vertiports; see Fig. 5.2 for an illustration. The capacity of each vertiport can be either 600 or 1200 takeoffs and landings per hour; choosing these capacities will take 1 or 2 units of cost. We add an air link to each pair of vertiports if their physical distance is greater than the median of the pairwise distance of all the nodes in the Anaheim network. The free travel time of these air links is set to be proportional to the corresponding distance, and the flow capacity is fixed to be 80 flights per hour for all air links.

We also consider the following budget and logical constraints on the vertiport locations. First, the total selection budget  $\gamma$  is chosen such that  $\gamma \in [5, 11]$ . Second, the locations marked in Fig. 5.2 are subject to the logical constraints listed in Tab. 5.1.

Table 5.1: Logical constraints for vertiport locations marked in Fig. 5.2

Marker color	Constraints on the corresponding locations
red	both are selected
magenta	at least one is selected
yellow	one and only one is selected
green	one and only one is selected

With the above choices of parameters, we solve Problem 9. To demonstrate our results, we define the following notion of *link loading* for each link  $k = 1, 2, \dots, n_l$ :

$$\ell_k(X, p, q) = [c + p + D^\top q]_k [X \mathbf{1}_d]_k. \quad (5.24)$$

Intuitively,  $\ell_k$  denotes the number of vehicles traveling on link  $k$  at the equilibrium—which is also the summand in the total link loading defined in (5.15).

Fig. 5.3 shows the link loading in the ground and air networks when we let choose the budget to be  $\gamma = 8$ . The shape of the marker indicates the capacity of the corresponding vertiport: the square marker denotes the capacity value of 600, which costs one unit in the budget; the triangle marker denotes the capacity value of 1200, which costs 2 units in the budget. In this case, a total of six vertiports are selected, and only two of them have the larger capacity value of 1200: the one near Westminster and the one near Villa Park; the latter fact is consistent with the air link loading

distribution in Fig. 5.3: the vertiports near Westminster and Villa Park are connecting some of the flight legs with the highest loading; hence they necessarily need larger capacity.

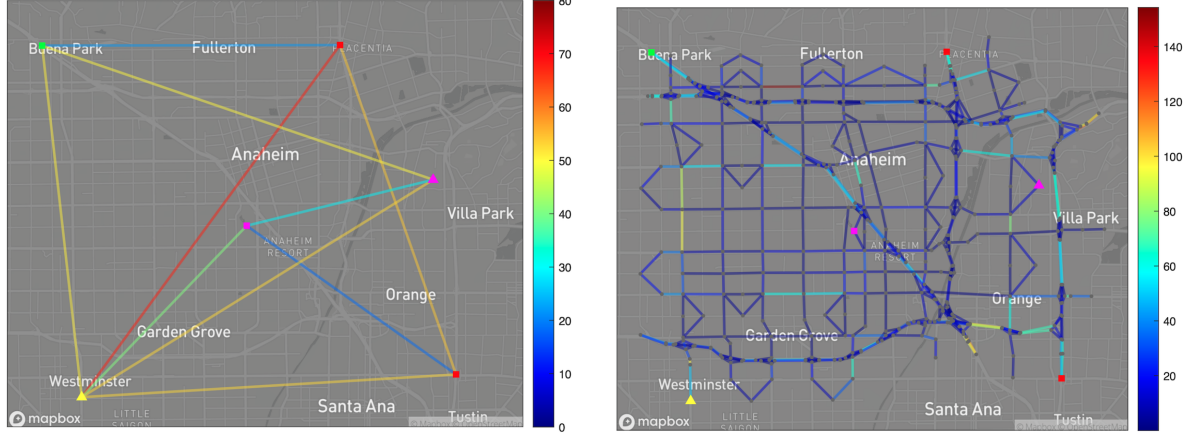


Figure 5.3: The optimal air and ground traffic network loading when vertiport selection budget  $\gamma = 8$ .

### 5.3 Related works for task assignment problem

As previously mentioned, UAM is still in its early stages of development, and our understanding of this field is rather limited. Regarding the task assignment problem within the context of UAM, numerous critical questions need to be addressed to obtain a comprehensive understanding. These questions span various aspects, including the requisite number of vehicles to meet daily air travel demands, the optimal approach to the management battery packs in eVTOL aircraft (*i.e.*, whether to charge or replace the battery during daily operations), the impact of battery charging duration on overall profits, the ideal cruise speed of eVTOL aircraft for optimal profitability, the influence of task waiting times, *etc..* Addressing these questions provides valuable insights into the operational efficiency and profitability of the UAM system.

Multi-robot task allocation has been a popular topic in the robotics community for decades [127, 128]; some commonly used strategies include mixed-integer linear programming [129, 130], Hungarian methods [131, 132], greedy algorithms [133], auction algorithms [134, 135], game theory [136], and more. With the increasing demands and the scale of the problem, a recent trend for this type of problem is to solve it in real time and in a distributed manner.

However, our approach focuses on designing a centralized and offline algorithm to address some of the questions mentioned above. In this chapter, we will assign a sequence of tasks to each vehicle within a specified time duration, such as a day, with the purpose of maximizing the overall profits of completing these tasks. We formulate tasks as a directed graph and transform the task assignment problem into identifying multiple non-intersecting paths that maximize the overall profits while satisfying time and battery charge constraints.

The literature most closely related to our research is the line of work on the team orienteering problem with time window (TOPTW) [137]. The orienteering problem (OP) is also known as the selective traveling salesman problem (TSP); the TSP is to minimize the travel time while the OP involves maximizing the total score collected. Furthermore, It is not required to visit all nodes in the network for OPs. TOPTW is an OP where the purpose is to identify multiple paths, with each node having specific time window constraints that necessitate the node to be visited only during the specified time window. TOPTW essentially is the same as elementary shortest path problem with resource constraints (ESPPRC). Both OP and TOPTW are typically modeled using graph representation and formulated as a mixed-integer program. In these formulations, integer variables are used to make decisions regarding which nodes or edges should be included in the optimal solution. Both problems are known to be NP-hard.

The common strategies for solving OP and TOP are classified as exact and heuristic algorithms. Exact methods include solving a mixed-integer program by branch-and-cut procedure [138, 139], dynamic programming (DP) [140, 141], etc. Heuristics methods include ant colony system [142, 143], tabu search [144, 145], guided local search [146], etc.

Our algorithm first addresses the single path identification problem by utilizing DP. Feillet *et al.* [141] proposed an exact solution procedure for ESPPRC. The algorithm is adapted from Desrochers' label correcting algorithm [147] and is able to deal with graphs containing negative cost cycles. The efficiency of the algorithm is numerically demonstrated. Righini and Salani [140] presented and compared three DP-based algorithms for ESPPRC: exact DP, branch-and-bound based on state-space relaxation, and decremental state-space relaxation. The DP-based labeling algorithm by Feillet is modified and implemented in our algorithm.

Subsequently, we solve the multiple paths identification using a greedy algorithm. Greedy algorithms are often used to solve task assignment problems whose objective function is submod-

ular [148, 149, 150, 151]. Guannan *et al.* [133] proposed a distributed greedy algorithm for the multi-agent task assignment problem. Only local information and local communication are needed for each agent to select its task. The sub-optimality of the proposed algorithm was proved, and a refined efficiency ratio bound was provided. Xu *et al.* [152, 153] proposed a greedy algorithm for a TOP with a ratio of  $1 - (1/e)^{\frac{1}{2+\epsilon}}$  where  $\epsilon$  is a given constant. They considered different scenarios, such as extra node costs and different vehicle types, and adjusted the proposed algorithm for these scenarios.

#### **5.4 Task assignment and vehicle routing for UAM**

This section introduces a novel task assignment and vehicle routing algorithm for UAM. In addition to the geographic air network where eVTOLs operate, a task network is constructed for the assignment algorithm. By employing this formulation, the task assignment problem for UAM is transformed into finding multiple non-intersecting paths that maximize profits.

##### *5.4.1 Task network formulation*

Suppose that in a metropolitan city with a number of vertiports and predetermined daily travel demands, an airline company operates a fleet of eVTOLs to meet these demands. The vertiports establish a geographic network, with each node representing a vertiport. Each travel demand is associated with a profit based on the travel distance, the number of passengers, battery consumption, etc. The primary goal is to develop an algorithm that assigns a sequence of travel demands to each vehicle in order to maximize the overall profits of these demands while satisfying certain constraints, such as time window constraints and battery constraints.

Fig. 5.4 presents a simple illustrative example of a geographic network consisting of four vertiports. Each link in the network is assigned a weight that represents the travel time between two vertiports. For example, the travel time from vertiport 1 to vertiport 2 is 7.07 minutes.

##### *Assumptions for constructing the task network*

When constructing the task network, the following characteristics are assumed for the tasks and the network:

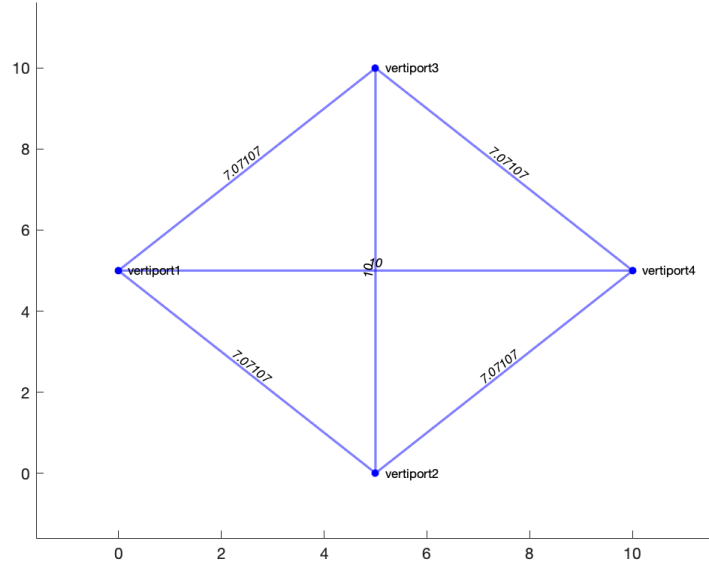


Figure 5.4: Vertiport network example.

**Definition 2.** A “travel demand”, which is referred to as a task, involves transporting a specific number of passengers from one vertiport to another. All the relevant information associated with this task is provided in advance;

**Assumption 8.** Tasks are modeled as a directed graph. Each task is a node in the graph. A directed connection is established between two tasks if a vehicle is able to sequentially accomplish them within time windows, which requires the vehicle to fly from the destination of the preceding task to the origin of the subsequent task and arrive before the latest starting time. This ensures that the tasks can be efficiently executed in a specific order without violating any time constraints.

We introduce the following key concepts to define task information within the context of the problem:

1. **Time-dependent profit  $r_i$ :** Each task, denoted as  $i$ , is associated with a time-dependent profit, represented as  $r_i$ . This profit is a stepwise function, equaling zero outside the time window and equaling a positive constant during the time window interval when the task

can be performed. The profit reflects the monetary benefit the airline company gains from successfully completing task  $i$  during its specified time window.

2. **Time window**  $[a_i, b_i]$ : Each task  $i$  is assigned a time window, denoted as  $[a_i, b_i]$ , where  $a_i$  is the earliest starting time of task  $i$ ;  $b_i$  is the latest starting time by which task  $i$  must begin. This time window provides the visiting constraints: if a vehicle arrives before  $a_i$ , it has to wait until  $a_i$ ; and task  $i$  cannot be completed later than  $b_i$ ;
3. **Service time**  $s_i$ : Each task  $i$  is associated with a service time, denoted as  $s_i$ . This represents the duration required to transport passengers from the origin vertiport to the destination vertiport for task  $i$ ;

Fig. 5.5 presents an illustrative example of a task network consisting of seven tasks. The horizontal axis represents the earliest starting time of each task. For instance, the earliest starting time of task 1 is at  $t = 0$ , and the earliest starting time of task 7 is at  $t = 90$  min. The vertical axis represents the profit associated with each task. For example, task 4 has the highest profit of  $p_4 = 4.8$ . The labels above each node indicate the origin and destination locations of the corresponding task. For example, task 1 is to transfer passengers from vertiport 2 to vertiport 1.

The directed link between two nodes signifies that a vehicle can sequentially complete the tail node and the head node within their respective time windows. Each link is associated with a time cost and a corresponding battery charge cost. For example, the link between node 1 and node 4 indicates that after completing task 1, the vehicle needs to fly from vertiport 1 to vertiport 2, and this link is referred to as a “non-profit” link; in contrast, the link between node 1 and node 6 has zero time cost since the destination location of node 1 is the same with the origin location of task 6.

Fig. 5.5 also presents a feasible task path in this network  $1 \rightarrow 3 \rightarrow 5 \rightarrow 6 \rightarrow 7$ . It displays the total profits and the time cost associated with the “non-profit” links. It is obvious that path  $1 \rightarrow 4 \rightarrow 5 \rightarrow 6 \rightarrow 7$  yields a higher profit than  $1 \rightarrow 3 \rightarrow 5 \rightarrow 6 \rightarrow 7$ , as node 4 is positioned higher than node 3.

Fig. 5.6 represents a vehicle’s route corresponding to the path  $1 \rightarrow 4 \rightarrow 5 \rightarrow 6 \rightarrow 7$  in task network Fig. 5.5. For a vehicle to complete this task path, the flying route for this vehicle is vertiport 2  $\rightarrow$  1  $\rightarrow$  3  $\rightarrow$  2  $\rightarrow$  3  $\rightarrow$  1  $\rightarrow$  2  $\rightarrow$  4  $\rightarrow$  3.

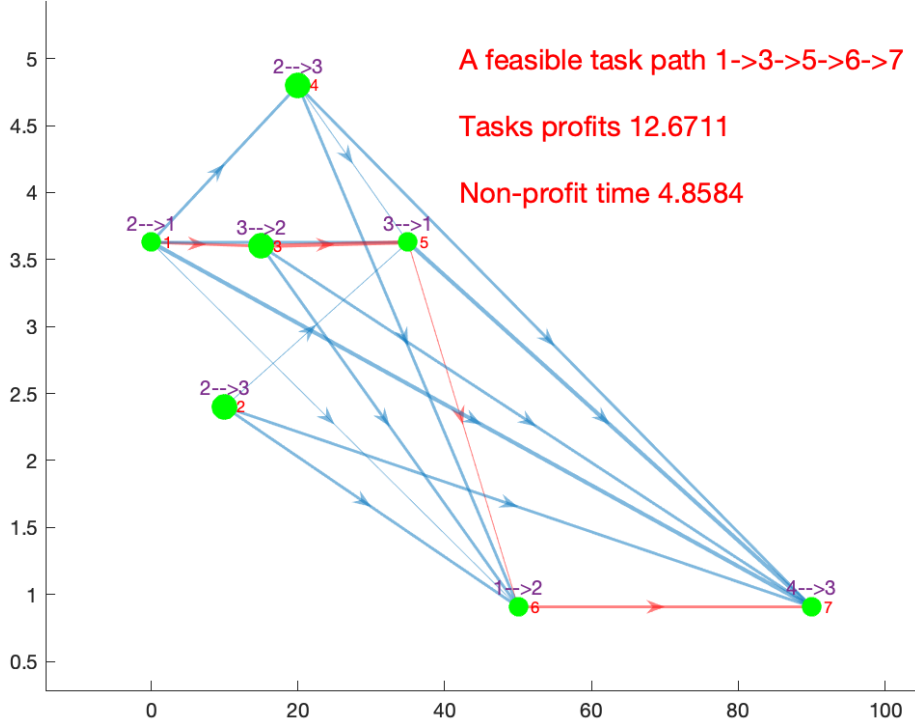


Figure 5.5: Task network example.

With this novel formulation, the task assignment problem for multiple agents is transformed into a “max-profit paths finding problem”. The goal is to identify multiple non-intersecting paths in the task network, aiming to maximize the total profits generated from these paths while satisfying the time and battery charge constraints.

**Remark 4.** *It is required that each task can only be completed by one vehicle in the task network; if two vehicles visit the same node, only one vehicle can obtain the benefit, and the other vehicle incurs an extra battery charge cost since each task represents a physical transportation.*

#### 5.4.2 Mixed integer programming

We now introduce a mathematical model that selects paths in the task network as an effort to optimize the task assignment problem. Suppose a directed graph  $\mathcal{G} = (\mathcal{V}, \mathcal{E})$ , where  $\mathcal{V}$  is the set of

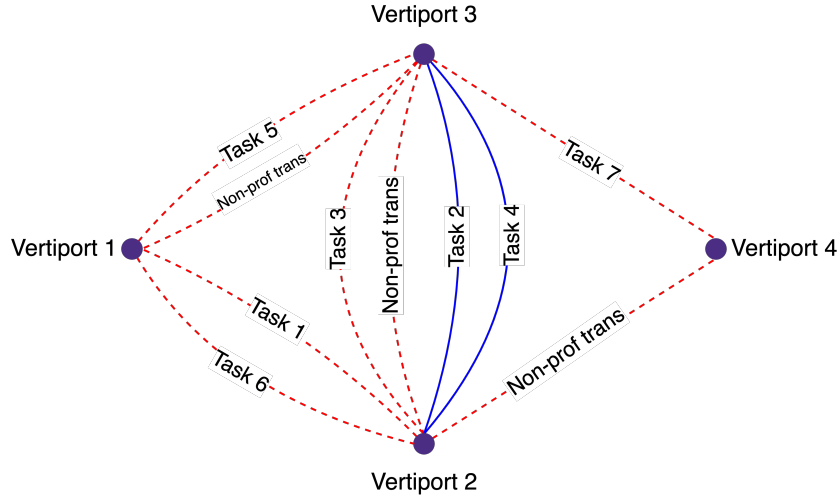


Figure 5.6: Vehicle route for the feasible task path  $1 \rightarrow 3 \rightarrow 5 \rightarrow 6 \rightarrow 7$  in Fig. 5.5.

tasks;  $\mathcal{E}$  is the set of links; a directed link  $(i, j)$  exists if and only if the following condition holds,

$$b_j \geq a_i + s_i + \tau_{i,j}, \quad (5.25)$$

where  $\tau_{ij}$  is the traveling time associated with edge  $(i, j)$ ; if the destination location of task  $i$  and the origin location of task  $j$  are the same, then  $\tau_{ij} = 0$ ; otherwise  $\tau_{ij} = \Delta_t d(i, j) + \delta_t$ , where  $d(i, j)$  is the distance between the destination location of task  $i$  and the origin location of task  $j$ , and  $\Delta_t$  is a constant time parameter;  $\delta_t$  accounts for the eVTOL's takeoff and landing time, which is a constant value.

We also introduce the following notions to formulate the mathematical optimization problem,

- $t_i^k$  is the time when node  $i$  is visited by vehicle  $k$ ;
- $\theta_i^k$  is the SOC of the battery when vehicle  $k$  arrives node  $i$  without having started to execute this task;
- $\tilde{\theta}_i$  is the ratio of the battery charge consumed by task  $i$  to the maximum charge capacity of the vehicle's battery;

- $\bar{\theta}_{ij}$  is the ratio of the battery charge consumed by arc  $(i, j)$  to the maximum charge capacity of the vehicle's battery;
- $\theta_{min}$  and  $\theta_{max}$  are the lower and upper bounds for the vehicle's SOC, respectively;
- $t_c$  is the time required for the vehicle to be fully charged, which is assumed to be a constant value for simplicity;
- $x_{ij}^k$  and  $y_{ik}$  are decision variables, where  $x_{ij}^k = 1$  indicates that the edge  $(i, j)$  is used by vehicle  $k$  in its path;  $y_{ik} = 1$  denotes that the task  $i$  is completed by vehicle  $k$ ;

among these parameters,  $t_i^k$  and  $\theta_i^k$  are variables of the optimization problem;  $\tilde{\theta}_i$ ,  $\bar{\theta}_{ij}$ ,  $\theta_{min}$ ,  $\theta_{max}$ , and  $t_c$  are constant parameters provided in advance.

The objective function in the optimization problem is formulated as

$$\sum_{k=1}^{N_v} \sum_{i=1}^{N_t} r_i(t_i^k) y_{ik} - \omega \sum_{k=1}^{N_v} \sum_{i,j \in \mathcal{V}} x_{ij}^k \bar{\theta}_{ij} \quad (5.26)$$

where  $N_v$  is the number of vehicles;  $N_t$  is the number of tasks;  $\omega$  is the weight parameter to convert the battery charge into monetary cost. This objective function considers both task profits and “non-profit” battery charge consumption.

**Remark 5.**  $N_v$  is assumed to be a very large number since we need Problem 10 to determine the number of vehicles needed.

With these notions and the objective function, the optimization problem is defined as,

**Problem 10.** Determine  $x_{ij}^k, y_{ik}, t_i^k, \theta_i^k$  that solves the following problem,

$$\max_{x_{ij}^k, y_{ik}, t_i^k, \theta_i^k} \sum_{k=1}^{N_v} \sum_{i=1}^{N_t} r_i(t_i^k) y_{ik} - \omega \sum_{k=1}^{N_v} \sum_{i,j \in \mathcal{V}} x_{ij}^k \bar{\theta}_{ij} \quad (5.27a)$$

$$s.t. \quad \sum_{i \in \mathcal{V}} x_{ih}^k = \sum_{j \in \mathcal{V}} x_{hj}^k = y_{hk}, \quad \forall k \in \{1, 2, \dots, N_v\}, \quad \forall h \in \mathcal{V}, \quad (5.27b)$$

$$\sum_{k=1}^{N_v} y_{ik} = 1, \quad (5.27c)$$

$$t_j^k \geq t_i^k + s_i + \tau_{ij} - M(1 - x_{ij}^k), \quad i, j \in \mathcal{V}, \quad \forall k \in \{1, 2, \dots, N_v\}, \quad (5.27d)$$

$$\theta_j^k \geq \theta_i^k + \tilde{\theta}_i + \bar{\theta}_{ij} - M(1 - x_{ij}^k), \quad i, j \in \mathcal{V}, \quad \forall k \in \{1, 2, \dots, N_v\}, \quad (5.27e)$$

$$\theta_i^k \geq \tilde{\theta}_i, \quad \forall i \in \mathcal{V}, \quad \forall k \in \{1, 2, \dots, N_v\}, \quad (5.27f)$$

$$t_i^k = \max\{a_i, t_i^k\}, \quad \forall i \in \mathcal{V}, \quad \forall k \in \{1, 2, \dots, N_v\}, \quad (5.27g)$$

$$t_i^k \leq b_i, \quad \forall i \in \mathcal{V}, \quad k \in \{1, 2, \dots, N_v\}, \quad (5.27h)$$

$$-\min\{\theta_i^k - \theta_{min}, 0\}(\theta_i^k - \theta_{max}) = 0 \quad (5.27i)$$

$$-\min\{\theta_i^k - \theta_{min}, 0\}(t_i^k - \bar{t}_c) = 0, \quad (5.27j)$$

$$\bar{t}_c = t_i^k + t_c, \quad (5.27k)$$

$$x_{ij}^k \in \{0, 1\}, \quad (i, j) \in \mathcal{E}, \quad (5.27l)$$

$$y_{ik} \in \{0, 1\}, \quad i \in \mathcal{V}, \quad k \in \{1, 2, \dots, N_v\}, \quad (5.27m)$$

where  $M$  is a very large constant number to facilitate the definition of time and battery charge constraints.

Each constraint in this problem is explained in the following,

- Eq.(5.27b) ensures a conservative relation between visited links and visited nodes. If task  $h$  is visited by vehicle  $k$ , then there are only one incoming edge and one outgoing edge of task  $h$  are visited by vehicle  $k$ ;
- Eq.(5.27c) ensures each node can be visited once and only once;
- Eq.(5.27d) introduces time constraints for vehicle  $k$  to complete task  $i$  and task  $j$  sequentially.

When  $x_{ij}^k = 1$ , the arriving time at task  $j$  should be later than the arriving time to task  $i$  plus the service time of task  $i$  and the traveling time from  $i$  to  $j$ ; In other words, the vehicle must reach task  $i$ , complete it, and then travel to task  $j$ , ensuring that task  $j$  is visited after task  $i$  in the itinerary if  $x_{ij}^k = 1$ . When  $x_{ij}^k = 0$ , there are no constraints between  $t_i^k$  and  $t_j^k$ ;

- In Eq.(5.27e), when  $x_{ij}^k = 1$ , vehicle  $k$  needs to satisfy the battery charge constraints in order to complete task  $i$  and task  $j$  sequentially; when  $x_{ij}^k = 0$ , there are no constraints between  $t_i^k$  and  $t_j^k$ ;
- Eq.(5.27f) requires that the SOC of vehicle  $k$  must be greater than or equal to the battery charge consumed by task  $i$  when the vehicle arrives at node  $i$ . This ensures that the vehicle has enough battery charge to complete task  $i$ ;
- Eq.(5.27g) and Eq.(5.27h) constrain the starting time of task  $i$  within the given time window; Eq.(5.27g) indicates that if the vehicle arrives node  $i$  before  $a_i$ , it has to wait until  $a_i$  to begin the task;
- Eq.(5.27i) and Eq.(5.27j) are the state-triggered constraints. If  $\theta_i^k \geq \theta_{\min}$ , then  $-\min\{\theta_i^k - \theta_{\min}, 0\} = 0$ , leading to Eq.(5.27i) and Eq.(5.27j) hold without any requirement on the sign of terms in parentheses; in contrast, if  $\theta_i^k \leq \theta_{\min}$ , then this constraint requires  $\theta_i^k - \theta_{\max} = 0$  and  $t_i^k - \bar{t}_c = 0$ , respectively, which means the SOC of vehicle  $k$  is charged to  $\theta_{\max}$  and the corresponding time for vehicle  $k$  is postponed.

Essentially, this problem is similar to TOPTW constraints except for the following differences,

1. In the original TOPTW, all agents start from the same node and end at the same node (might be different from the starting node). In Problem 10, all vehicles need to start from different nodes since each node can only be visited once by one vehicle, and there is no fixed ending point for each path. We let the algorithm lead us to find the best ending node for each path;
2. In the original TOPTW, resources are usually independent (for example, time is one of the most common resources). In Problem 10, the battery's SOC is one of the resources, and the

SOC is coupled with the time: when a vehicle's SOC is lower than  $\theta_{min}$ , it has to be charged; this action will cost time, hence affect both the SOC constraint and the time constraint.

#### 5.4.3 Greedy algorithm and sub-modular proof

This mixed-integer programming is an NP-hard problem, indicating that finding an exact solution efficiently is computationally challenging. In this subsection, the concepts of submodular problems are introduced, the submodular property of the objective functions in Problem 10 is proved, and a greedy algorithm to solve this problem is presented.

The following assumption is essential for the subsequent submodular property,

**Assumption 9.** *All vehicles are identical, and each vehicle's initial location is decided by the optimal solution of Problem 10. The number of vehicles required for a specific task network is also obtained from the solution of Problem 10.*

We refer to nodes with zero indegree as “starting points”. Assumption 9 requires us to identify multiple paths with different starting points in the task network. We will present how to choose the starting points in the task network dynamically based on the structure of the task network.

**Remark 6.** *Instead of assigning multiple tasks to each vehicle, Problem 10 essentially is to identify multiple paths for different starting points in the task network.*

#### *Max-profit path for a single vehicle*

Finding a maximum-profit path for a single vehicle is similar to the ESPPRC, which involves finding the minimum cost elementary path (with no repeated nodes) between two specified nodes while satisfying resource constraints [154]. The only difference is that we do not specify the ending node for the max-profit path problem; instead, we need to determine the ending node that yields the max-profit path. The standard approach to solve ESPPRC relies on dynamic programming, which is to associate with each feasible partial path a label indicating the cost and the consumption of resources while also eliminate labels with the help of dominance rules [141]. The algorithm proposed by Feillet *et al.* [141] is adopted with some modifications due to the special properties of the task network. The following notions are introduced to describe the algorithm:

- $\mathcal{L}_i$  is the list of labels on node  $v_i$ ;  $\lambda_i \in \mathcal{L}$  contains the profit, the cost on resources such as consumed time and battery charge, and the paths ending in  $v_i$  (*i.e.*, the set of nodes  $[v_{ini}, \dots, v_i]$ );
- $S(v_i)$  is the set of successors of node  $v_i$ ;
- $E$  is the set of nodes waiting to be treated;
- $F_{ij}$  is the set of labels extended from node  $v_i$  to node  $v_j$ .

---

**Algorithm 1** Maximum profit path with resource constraints

---

Initialize and label the starting point  $v_{ini}$

```

2: for all  $j \in S(v_{ini})$  do
    $\mathcal{L}_j \leftarrow \phi$ 
4: end for
    $E = \{v_{ini}, S(v_{ini})\}$ 
6: while  $E \neq \phi$  do
    $v_i = E(1)$ 
8:   for  $v_j \in S(n_i)$  do
       $F_{ij} = \phi$ 
10:    for  $\lambda_i \in \mathcal{L}_i$  do
       if  $v_j \notin \lambda_i$  then
12:          $F_{ij} \leftarrow F_{ij} \cup Extend(\lambda_i, v_j)$ 
       end if
14:    end for
        $\mathcal{L}_j \leftarrow EFF(F_{ij} \cup \mathcal{L}_j)$ 
16:   end for
    $E = E / \{v_i\}$ 
18: end while

```

---

The procedure  $Extend(\lambda_i, v_j)$  is a function that returns updated labels for  $v_j$  if the transportation from  $v_i$  to  $v_j$  is feasible; otherwise, it returns nothing. The procedure  $EFF(F_{ij} \cup \mathcal{L}_j)$  eliminates non-dominant labels from  $\mathcal{L}_j$  (We refer the interested readers to [141] for a detailed explanation of this function). The difference between Algorithm 1 and the algorithm proposed by Feillet is that, after updating labels of  $v_j \in S(v_{ini})$ , we do not add  $v_j$  to  $E$  due to the special structure of the task network, *i.e.*, all tasks are time sequentially connected, and a vehicle can only traverse the network

in one direction. This indicates that once the path travels from  $v_i$  to  $v_j$ , it is impossible for it to travel back to  $v_i$  due to time constraints. By eliminating the addition of nodes back to the set  $E$  in the algorithm, we avoid unnecessary computations and effectively limit the search space. This modification significantly reduces computational time and lays the foundation for the subsequent greedy algorithm.

### *Submodular property*

To explain the submodular property of Problem 10, the objective function is rewritten as

$$\max_{P^* \subset \mathcal{P}} f(P^*) = \sum_{i=1}^{|P^*|} g(p_i) \quad (5.28)$$

where  $\mathcal{P}$  is the set of all feasible paths;  $P^*$  is a subset of  $\mathcal{P}$ , and the cardinality of  $P^*$  is  $|P^*|$ ;  $p_i = [v_1, v_2, \dots, v_l]$ ,  $v_1, \dots, v_l \in \mathcal{V}$  is a feasible path in  $P^*$ ;  $g(p_i)$  is the pure profit generated by path  $p_i$ . Essentially Eq.(5.28) is the same as Eq.(5.27a); in both equations, the goal is to find multiple paths to maximize the pure profits in the task network. This objective function has the submodular property.

**Lemma 1.** *A function  $f : 2^N \rightarrow \mathbb{R}$  is submodular if and only if for every  $X, Y \in N$ ,  $f(X) + f(Y) \geq f(X \cap Y) + f(X \cup Y)$ .*

With this lemma, the following theory is proposed,

**Theorem 1.** *The objective function in Problem 10 is a submodular function.*

*Proof.* Let  $N = \mathcal{P}$  be the set of all feasible paths in the task network, and  $X, Y$  are two subsets of  $N$ . Denote paths in  $X$  as  $[p_{x1}, p_{x2}, \dots, p_{xn}]$  and paths in  $Y$  as  $[p_{y1}, p_{y2}, \dots, p_{yn}]$ . If  $X$  and  $Y$  have no intersecting paths, then  $X \cap Y = \emptyset$ ,  $f(X \cap Y) = 0$ , and  $f(X \cup Y) = f([p_{x1}, \dots, p_{xn}, p_{y1}, \dots, p_{yn}]) = f([p_{x1}, \dots, p_{xn}]) + f([p_{y1}, \dots, p_{yn}]) = f(X) + f(Y)$ ; hence the submodular property is satisfied.

If  $X$  and  $Y$  have intersecting paths, without losing generalizations, suppose that only  $p_{x1}$  and  $p_{y1}$  have one shared node  $v_s$ ; all other paths are non-intersecting. Let  $p_{x1} = [v_{x1}, \dots, v_s, \dots, v_{xm}]$  and  $p_{y1} = [v_{y1}, \dots, v_s, \dots, v_{ym}]$ , where  $xm$  and  $ym$  are the total nodes visited in two paths, respectively. In the task network, this indicates that two vehicles visit the same task  $v_s$ , and only one can obtain

the profit of this task; denote the incoming edges for path  $p_{x1}$  and  $p_{y1}$  are  $(x_i, s)$  and  $(y_i, s)$ , respectively (the incoming edges cannot be the same for two paths; otherwise there will be more than one shared nodes), and the outgoing edges for paths  $p_{x1}$  and  $p_{y1}$  are  $(s, x_o)$  and  $(s, y_i)$ , the pure profit of path  $p_{x1}$  is computed as

$$g(p_{x1}) = r_{v_{x1}} + \dots + r_{v_s} + \dots + r_{v_{xm}} - \omega(\bar{\theta}_{v_{x1}v_{x2}} + \dots + \bar{\theta}_{v_{xi}v_s} + \bar{\theta}_{v_sv_{xo}} + \dots), \quad (5.29)$$

the pure profit of path  $p_{y1}$  is computed as

$$g(p_{y1}) = r_{v_{y1}} + \dots + r_{y_s} + \dots + r_{v_{ym}} - \omega(\bar{\theta}_{v_{x1}v_{x2}} + \dots + \bar{\theta}_{v_{yi}v_s} + \bar{\theta}_{v_sv_{yo}} + \dots), \quad (5.30)$$

then  $f(X) + f(Y) = g(p_{x1}) + \dots + g(p_{xm}) + g(p_{y1}) + \dots + g(p_{ym})$ .

$X \cap Y$  is the single node  $v_s$ , the pure profit is  $f(X \cap Y) = r_{v_s}$ ;  $X \cup Y$  is the set of all paths in  $X$  and  $Y$  including the intersecting paths  $p_{x1}$  and  $p_{y1}$ . By Remark 4, when a node is visited by two vehicles, only one vehicle can obtain the profit, and the other vehicle needs to pay extra battery charge cost. Hence,

$$f(X \cup Y) = g(p_{x1}) + \dots + g(p_{xm}) + g(p_{y1}) + \dots + g(p_{ym}) - r_{v_s} - \omega\bar{\theta}_{v_s}, \quad (5.31)$$

where  $\omega\bar{\theta}_{v_s}$  is the battery charge cost of task  $v_s$ . Then, we conclude that  $f(X) + f(Y) \geq f(X \cap Y) + f(X \cup Y)$ , where the right hand side is shorter in  $\omega\bar{\theta}_{v_s}$ . This conclusion can be generalized to multiple intersections between  $X$  and  $Y$ .  $\square$

### *Greedy algorithm*

The greedy algorithm constructs a solution by starting with an empty set and iteratively adding new elements that improve the current solution the most. It is able to guarantee that the solution is at least  $\frac{1}{1+\kappa}$  of the optimal solution for submodular functions, where  $\kappa$  is the curvature of the submodular function. The curvature of Eq.(5.28) depends on the battery charge consumption of each task and varies with the task network. We have demonstrated that the objective function for our task assignment problem is submodular. Now, we propose the greedy algorithm. Let  $m$  be the number of starting points. Algorithm 2 starts with these  $m$  nodes and dynamically adds more

“starting nodes” as needed.

---

**Algorithm 2** Greedy algorithm for multiple paths

---

```

Initialize  $m$  starting nodes
2:  $F = \mathcal{V}$ ,  $N_w = m$ 
  while  $F \neq \emptyset$  or  $N_w = N_v$  do
    4:   Run Algorithm 1 for each starting nodes, obtain  $m$  paths
        Finalize non-intersecting paths, remove nodes in these paths from  $F$ ,
    6:   For paths that share nodes with other paths, finalize the path with the highest profit, remove
        nodes in this path from  $F$ 
        Rebuild the task network after removing all nodes of finalized paths
    8:   Identify new starting nodes,  $N_w = [N_w, N_f]$ 
  end while

```

---

#### 5.4.4 Numerical results

We use a simple geographic network and a randomly generated task set to show information of UAM obtained from the solution of Problem 10.

Suppose we have a geographic network shown in Fig. 5.7.

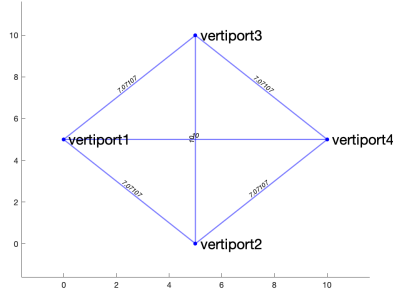


Figure 5.7: Geographic network with 8 vertiport

Vehicle index	Sequence of tasks
1	[2, 9, 13, 19, 25, 36]
2	[3, 14, 22, 26, 40]
3	[5, 18, 27, 31, 44, 49]
4	[4, 10, 20, 28, 33, 50]
5	[6, 12, 23, 39, 45]
6	[1, 7, 17, 24, 46]
7	[8, 21, 32, 38, 43]
8	[15, 30, 34, 41, 47]
9	[11, 16, 29, 35, 48]
10	[37, 42]

Table 5.2: Path assignment results.

The following task set has been considered: The total number of tasks is 50; the starting time range for tasks is [0, 3hr]. The origin and destination locations are randomly generated.

The numerical results obtained from the greedy algorithm are shown in Fig. 5.8. Starting nodes are colored as pink, and ending nodes are colored as black.

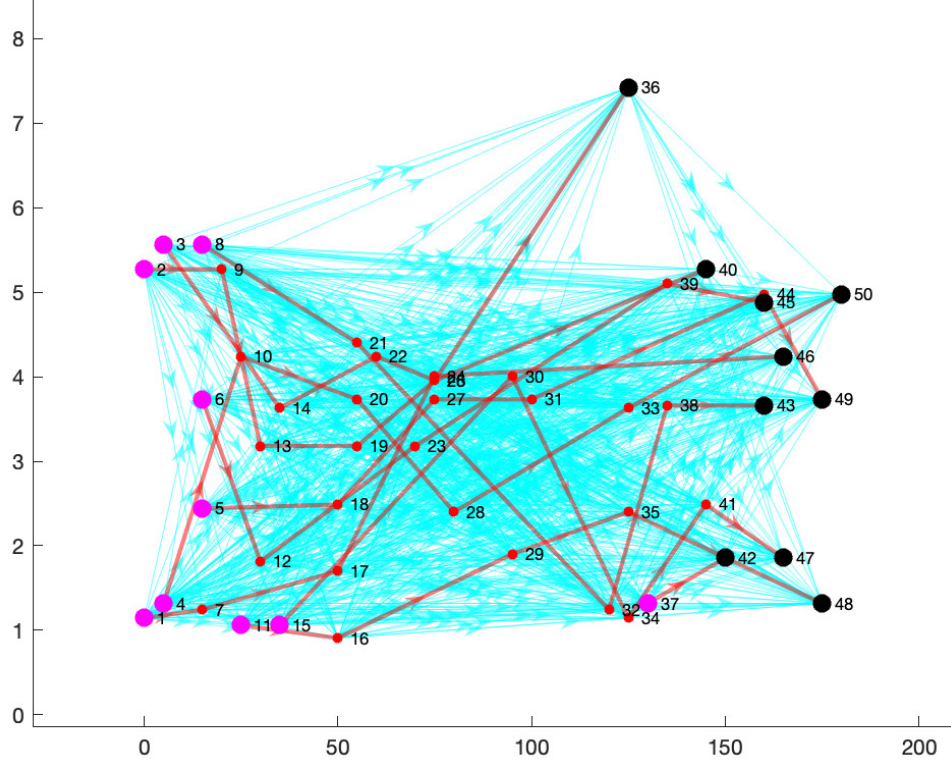


Figure 5.8: Paths obtained from greedy algorithm.

From Fig. 5.8, it is evident that the task network becomes significantly complex, even for a relatively small number of tasks. Numerical results indicate that completing every task in this network requires the deployment of 10 vehicles. The resulting paths for each vehicle are presented in Table 5.2. Notably, nine out of the ten vehicles are assigned at least five tasks, while the last vehicle is assigned only two tasks. The computation time for this analysis is 0.54 seconds.

To further explore the system's performance, 100 sets of tasks with a similar pattern are randomly generated (the total number of tasks is 50; the starting time range for tasks is [0, 3 hr]). The average number of vehicles required to complete these tasks is found to be 11.29, with a median of 11 and a maximum of 14. Given the geographical layout of a conceptual city as depicted in Fig. 5.7, and considering the same travel demand pattern as above, deploying 11 eVTOLs as regular vehicles,

along with three eVTOLs as backup, seems reasonable. The average computational time for this scenario is 0.23 seconds. The proposed algorithm is able to determine the number of vehicles required to meet the daily air travel demands in a city.

## Chapter 6

### CONCLUSIONS

This chapter underscores the threefold contributions of this dissertation while also outlining potential future research directions.

First, a comprehensive study of trajectory optimization algorithms for All-Electric Aircraft (AEA) is conducted. Various optimal control problems, integrating flight dynamics and battery dynamics, are formulated and analyzed using the minimum principle. The numerical results indicate that different battery models affect the overall direct operating cost of the flight. However, the optimal control input profiles slightly vary for distinct battery models. This observation provides valuable insights for the design of optimal control strategies for AEA. One practical approach involves obtaining offline optimal control profiles using simplified battery dynamics and then implementing these profiles in real time using online estimation algorithms to monitor the battery pack states. A Simulink model with configurable battery blocks is developed to verify the proposed algorithms and observe the battery dynamics, enabling a more accurate estimation of the operating cost of the flight.

For future research in this direction, several promising topics are worth exploring. Firstly, the optimal control profiles obtained in this dissertation for AEA are open-loop control solutions. A potential avenue for future investigation is developing closed-loop online algorithms that incorporate battery state of charge (SOC) estimation. This would enhance the real-time adaptability of the optimal control strategies to changing flight conditions and battery performance. Another intriguing area of exploration involves studying the thermal behavior estimation and thermal management of the battery pack during flight conditions. We have tried to solve an optimal control problem with the integration of flight dynamics and the single particle model; however, the problem is too complicated to be solved using commercial solvers. A feasible solution to tackle this challenge is to apply a model predictive control strategy. This approach would involve solving a simplified optimal control problem in a short horizon and implementing only the first step of the optimal

solution. Subsequently, the real-time flight states and battery states information would be used as feedback to iteratively solve the optimal control problem during flight, allowing for an adaptive and efficient battery thermal management system. These future directions hold significant promise and can contribute to advancing the field of All-Electric Aircraft trajectory optimization and battery management in the context of Urban Air Mobility.

Second, for Hybrid-Electric Aircraft (HEA), a power allocation algorithm is developed to optimize the distribution of power demand in the propulsion system for fuel savings. An optimal control problem is formulated and applied to a single-seat aircraft, and the minimum principle is utilized to analyze the necessary optimality conditions. The numerical results demonstrate that charging the battery pack using the engine during flight yields only a negligible amount of fuel savings. This observation leads to an investigation to understand the reasons behind this limited fuel-saving effect. The algorithm is then applied to a conceptual 19-seat aircraft, confirming that the fuel-saving achieved by charging the battery during flight remains minimal. Consequently, research is conducted on different hybrid electric configurations. Two parallel hybrid electric configurations (the connected configuration allows the engine to charge the battery during flight while the independent configuration does not have a mechanical connection between the engine and the electric path) are compared in the context of fuel minimization. The original optimal control problem is transformed into a finite-dimension optimization problem in order to conduct sensitivity analysis. The numerical results in the 19-seat aircraft indicate that compared to charging the battery during flight, increasing battery capacity onboard is more fuel-efficient. A Simulink model is developed to verify the proposed algorithms.

Regarding future research on energy management for HEA, the integration of battery dynamics is a worthwhile direction. The power allocation problem in this dissertation only considers fuel consumption and fuel rate maps while assuming that the output voltage of the battery pack remains constant. Integrating battery dynamics into the analysis will provide a more comprehensive overview of the energy management problem for HEA, leading to more accurate and realistic results. Another important direction is to consider battery degradation when comparing different hybrid electric configurations. Battery degradation over time can significantly impact the overall performance and efficiency of the aircraft's power system. Including battery degradation in the analysis will provide more practical insights into the long-term implications of different hybrid electric configurations.

Furthermore, an interesting research topic involves incorporating real-time SOC estimation of the battery into the fuel minimization problem. Real-time SOC estimation would enable the power allocation algorithm to adapt to changing battery conditions during flight, leading to more effective and dynamic power distribution, which can further enhance fuel efficiency for HEA.

In the final part of this dissertation, two network-level topics related to Urban Air Mobility (UAM) are explored. The first topic addresses the vertiport selection problem, where a mixed-integer linear program is introduced and applied to the city of Anaheim, California. Unlike conventional traffic networks, the hybrid ground-air network incorporates node capacity for static traffic equilibria. This approach enables the assessment of vertiport locations and capacities in the context of UAM, considering both ground and air transportation aspects. The second topic focuses on the assignment of travel demands to vehicles in the UAM system, referred to as the task assignment problem. This problem is transformed into the identification of multiple paths that maximize the overall profit. To demonstrate the effectiveness of the proposed algorithm, a conceptual geographic network is used, and a set of randomly generated tasks is employed as a test case. Through this demonstration, fundamental questions related to UAM, such as the required number of vehicles for a city, are addressed, providing valuable insights into the efficient operation of UAM systems.

In the context of implementing the task assignment algorithm, the current assumption of a linear relationship between battery charge consumption and traveling distance simplifies the analysis. However, a promising future direction involves investigating and understanding the precise relationship between battery charge consumption and flight conditions. This investigation would lead to a more accurate and realistic representation of battery usage in UAM operations, enabling better optimization of task assignments and resource management. Another crucial topic worth exploring is the impact of different charging patterns on the overall performance of UAM systems. Evaluating the trade-offs between charging patterns, including factors like charging time, battery lifespan, and operational efficiency, can provide insights into the most effective and sustainable strategies for managing battery resources in UAM. Additionally, it is essential to address variations and uncertainties in the task assignment problem. In real-world scenarios, UAM operations may face unpredictable factors, such as changing weather conditions, traffic congestion, or sudden changes in travel demand. Incorporating uncertainty into the task assignment algorithm can enhance the robustness and adaptability of the UAM system. This could involve using probabilistic models, scenario-based

optimization, or other uncertainty quantification techniques to develop more resilient and flexible task assignment strategies.

## BIBLIOGRAPHY

- [1] N. Thapa, S. Ram, S. Kumar, and J. Mehta, “All Electric Aircraft: A Reality on Its Way,” *Materials Today: Proceedings*, vol. 43, pp. 175–182, 2021.
- [2] E. Alvarado, “The Vision of Advanced Air Mobility: eVTOLs, Drone Delivery, Vertiports and UTM,” 2023.
- [3] M. Wang and M. Mesbahi, “Energy Management for Electric Aircraft via Optimal Control: Cruise Phase,” in *2020 AIAA/IEEE Electric Aircraft Technologies Symposium (EATS)*, pp. 1–15, IEEE, 2020.
- [4] M. Wang, M. Mesbahi, S. Kolluri, K. A. Shah, and V. R. Subramanian, “Energy Management for an All-Electric Aircraft via Optimal Control,” *IEEE Transactions on Aerospace and Electronic Systems*, 2022.
- [5] M. Wang and M. Mesbahi, “Power Allocation for Hybrid Electric Aircraft via Optimal Control during Climb, Cruise, and Descent,” in *AIAA Scitech 2021 Forum*, p. 0640, 2021.
- [6] M. Wang and M. Mesbahi, “To Charge In-Flight or Not: A Comparison of Two Parallel-Hybrid Electric Aircraft Configurations via Optimal Control,” *IEEE Transactions on Transportation Electrification*, 2023.
- [7] Y. Yu, M. Wang, M. Mesbahi, and U. Topcu, “Vertiport Selection in Hybrid Air-Ground Transportation Networks via Mathematical Programs with Equilibrium Constraints,” *IEEE Transactions on Control of Network Systems*, 2023.
- [8] L. Juvé, J. du Fosse, E. Joubert, and N. Fouquet, “Airbus Group Electrical Aircraft Program, the E-Fan Project,” 2016.
- [9] D. Erzen, M. Andrejasic, and T. Kosel, “An Optimal Propeller Design for In-Flight Power Recovery on an Electric Aircraft,” in *2018 Aviation Technology, Integration, and Operations Conference*, p. 3206, 2018.
- [10] J. W. Langelaan, A. Chakrabarty, A. Deng, K. Miles, V. Plevnik, J. Tomazic, T. Tomazic, and G. Veble, “Green Flight Challenge: Aircraft Design and Flight Planning for Extreme Fuel Efficiency,” *Journal of Aircraft*, vol. 50, no. 3, pp. 832–846, 2013.
- [11] M. Anderson, “U.S. Airline Orders First Passenger Electric Plane: The Battery-Powered Nine-Seater Aircraft Will Enter Service in 2022-[News],” *IEEE Spectrum*, vol. 56, no. 09, pp. 10–11, 2019.

- [12] F. Martini, “World’s First Serial Hybrid Electric Aircraft to Fly at Le Bourget,” *AXX20110666e, Siemens, Munich*, 2011.
- [13] W. Wittmann, “Flying with Siemens Integrated Drive System,” *IDT2013064084e, Siemens, Nuremberg, Germany*, 2013.
- [14] D. Majumdar, “Pipistrel Rolls out First Prototype Panthera,” *Flight International*, vol. 183, no. 5385, pp. 29–29, 2013.
- [15] M. Caujolle and R. Gage, “Airbus, Rolls-Royce, and Siemens Team up for Electric Future Partnership Launches E-Fan X Hybrid-Electric Flight Demonstrator,” 2017.
- [16] R. Jaggi, “The Electric Airplane Revolution May Come Sooner Than You Think,”
- [17] C. Friedrich and P. Robertson, “Hybrid-Electric Propulsion for Aircraft,” *Journal of Aircraft*, vol. 52, pp. 176–189, Jan. 2015.
- [18] D. F. Finger, R. de Vries, R. Vos, C. Braun, and C. Bil, “A Comparison of Hybrid-Electric Aircraft Sizing Methods,” in *AIAA Scitech 2020 Forum*, p. 1006, 2020.
- [19] A. T. Stamps, C. E. Holland, R. E. White, and E. P. Gatzke, “Analysis of Capacity Fade in a Lithium Ion Battery,” *Journal of Power Sources*, vol. 150, pp. 229–239, 2005.
- [20] V. Ramadesigan, P. W. Northrop, S. De, S. Santhanagopalan, R. D. Braatz, and V. R. Subramanian, “Modeling and Simulation of Lithium-ion Batteries from a Systems Engineering Perspective,” *Journal of the Electrochemical Society*, vol. 159, no. 3, p. R31, 2012.
- [21] L. S. Pontryagin, *Mathematical Theory of Optimal Processes*. CRC press, 1987.
- [22] D. Liberzon, *Calculus of Variations and Optimal Control Theory: a Concise Introduction*. Princeton University Press, 2011.
- [23] M. Kaptsov and L. Rodrigues, “Flight Management Systems for All-electric Aircraft,” in *2017 IEEE Conference on Control Technology and Applications (CCTA)*, pp. 2126–2131, 2017.
- [24] M. Kaptsov and L. Rodrigues, “Electric Aircraft Flight Management Systems: Economy Mode and Maximum Endurance,” *Journal of Guidance, Control, and Dynamics*, vol. 41, no. 1, pp. 288–293, 2017.
- [25] J. T. Betts, “Survey of Numerical Methods for Trajectory Optimization,” *Journal of Guidance, Control, and Dynamics*, vol. 21, no. 2, pp. 193–207, 1998.
- [26] G. Chen, Y. Fu, and J.-F. Guo, “Survey of Aircraft Trajectory Optimization Methods,” *Flight Dynamics*, vol. 29, no. 4, pp. 1–5, 2011.

- [27] G. Huang, Y. Lu, and Y. Nan, “A Survey of Numerical Algorithms for Trajectory Optimization of Flight Vehicles,” *Science China Technological Sciences*, vol. 55, pp. 2538–2560, 2012.
- [28] A. V. Rao, “Trajectory Optimization: a Survey,” *Optimization and Optimal Control in Automotive Systems*, pp. 3–21, 2014.
- [29] O. Von Stryk and R. Bulirsch, “Direct and Indirect Methods for Trajectory Optimization,” *Annals of Operations Research*, vol. 37, pp. 357–373, 1992.
- [30] C. R. Hargraves and S. W. Paris, “Direct Trajectory Optimization Using Nonlinear Programming and Collocation,” *Journal of Guidance, Control, and Dynamics*, vol. 10, no. 4, pp. 338–342, 1987.
- [31] A. L. Herman and B. A. Conway, “Direct Optimization Using Collocation Based on High-order Gauss-lobatto Quadrature Rules,” *Journal of Guidance, Control, and Dynamics*, vol. 19, no. 3, pp. 592–599, 1996.
- [32] G. T. Huntington and A. V. Rao, “Comparison of Global and Local Collocation Methods for Optimal Control,” *Journal of Guidance, Control, and Dynamics*, vol. 31, no. 2, pp. 432–436, 2008.
- [33] D. M. Pargett and M. D. Ardema, “Flight Path Optimization At Constant Altitude,” *Journal of Guidance, Control, and Dynamics*, vol. 30, no. 4, pp. 1197–1201, 2007.
- [34] A. Franco, D. Rivas, and A. Valenzuela, “Minimum-Fuel Cruise At Constant Altitude with Fixed Arrival Time,” *Journal of Guidance, Control, and Dynamics*, vol. 33, no. 1, pp. 280–285, 2010.
- [35] J. Villarroel and L. Rodrigues, “Optimal Control Framework for Cruise Economy Mode of Flight Management Systems,” *Journal of Guidance, Control, and Dynamics*, vol. 39, no. 5, pp. 1022–1033, 2016.
- [36] D. Rivas and A. Valenzuela, “Compressibility Effects on Maximum Range Cruise At Constant Altitude,” *Journal of Guidance, Control, and Dynamics*, vol. 32, no. 5, pp. 1654–1658, 2009.
- [37] O. Cots, J. Gergaud, and D. Goubinat, “Time-Optimal Aircraft Trajectories in Climbing Phase and Singular Perturbations,” *IFAC-PapersOnline*, vol. 50, no. 1, pp. 1625–1630, 2017.
- [38] Y. Diaz-Mercado, S. G. Lee, M. Egerstedt, and S. Y. Young, “Optimal Trajectory Generation for Next Generation Flight Management Systems,” in *2013 IEEE/AIAA 32nd Digital Avionics Systems Conference (DASC)*, pp. 3C5–1, 2013.
- [39] P. Bonami, A. Olivares, M. Soler, and E. Staffetti, “Multiphase Mixed-integer Optimal Control Approach to Aircraft Trajectory Optimization,” *Journal of Guidance, Control, and Dynamics*, vol. 36, no. 5, pp. 1267–1277, 2013.

- [40] G. Barufaldi, M. Morales, and R. G. Silva, “Energy Optimal Climb Performance of Electric Aircraft,” in *AIAA Scitech 2019 Forum*, p. 0830, 2019.
- [41] R. D. Falck, J. Chin, S. L. Schnulo, J. M. Burt, and J. S. Gray, “Trajectory Optimization of Electric Aircraft Subject to Subsystem Thermal Constraints,” in *18th AIAA/ISSMO Multi-disciplinary Analysis and Optimization Conference*, p. 4002, 2017.
- [42] F. Settele, F. Holzapfel, and A. Knoll, “The Impact of Peukert-effect on Optimal Control of a Battery-electrically Driven Airplane,” *Aerospace*, vol. 7, no. 2, p. 13, 2020.
- [43] S. W. Paek, S. Kim, and R. V. Raj, “Optimal Endurance and Range of Electric Aircraft with Battery Degradation,” *Transactions of the Japan Society for Aeronautical and Space Sciences*, vol. 63, no. 2, pp. 62–65, 2020.
- [44] S. W. Paek, S. Kim, and C. V. R. Rayappan, “Impact of Battery Degradation on Lifetime Ranges of Electric Aircraft and Unmanned Underwater Vehicles,” in *2019 IEEE Conference on Control Technology and Applications (CCTA)*, pp. 79–85, 2019.
- [45] P. E. Rutquist and M. M. Edvall, “Propt-matlab Optimal Control Software,” *Tomlab Optimization Inc*, vol. 260, no. 1, p. 12, 2010.
- [46] M. Soler, A. Olivares, and E. Staffetti, “Hybrid Optimal Control Approach to Commercial Aircraft Trajectory Planning,” *Journal of Guidance, Control, and Dynamics*, vol. 33, no. 3, pp. 985–991, 2010.
- [47] M. A. Hannan, F. Azidin, and A. Mohamed, “Hybrid Electric Vehicles and Their Challenges: A Review,” *Renewable and Sustainable Energy Reviews*, vol. 29, pp. 135–150, 2014.
- [48] M. Sabri, K. A. Danapalasingam, and M. F. Rahmat, “A Review on Hybrid Electric Vehicles Architecture and Energy Management Strategies,” *Renewable and Sustainable Energy Reviews*, vol. 53, pp. 1433–1442, 2016.
- [49] E. Silvas, T. Hofman, N. Murgovski, L. P. Etman, and M. Steinbuch, “Review of Optimization Strategies for System-Level Design in Hybrid Electric Vehicles,” *IEEE Transactions on Vehicular Technology*, vol. 66, no. 1, pp. 57–70, 2016.
- [50] W. Enang and C. Bannister, “Modelling and Control of Hybrid Electric Vehicles (a Comprehensive Review),” *Renewable and Sustainable Energy Reviews*, vol. 74, pp. 1210–1239, 2017.
- [51] K. V. Singh, H. O. Bansal, and D. Singh, “A Comprehensive Review on Hybrid Electric Vehicles: Architectures and Components,” *Journal of Modern Transportation*, vol. 27, pp. 77–107, 2019.

- [52] M. Ehsani, K. V. Singh, H. O. Bansal, and R. T. Mehrjardi, "State of the Art and Trends in Electric and Hybrid Electric Vehicles," *Proceedings of the IEEE*, vol. 109, no. 6, pp. 967–984, 2021.
- [53] A. Sciarretta and L. Guzzella, "Control of Hybrid Electric Vehicles," *IEEE Control Systems Magazine*, vol. 27, no. 2, pp. 60–70, 2007.
- [54] A. Khajepour, M. S. Fallah, and A. Goodarzi, *Electric and Hybrid Vehicles: Technologies, Modeling and Control-A Mechatronic Approach*. John Wiley & Sons, 2014.
- [55] X. Ye, A. Savvarisal, A. Tsourdos, D. Zhang, and G. Jason, "Review of Hybrid Electric Powered Aircraft, Its Conceptual Design and Energy Management Methodologies," *Chinese Journal of Aeronautics*, vol. 34, no. 4, pp. 432–450, 2021.
- [56] T. J. Wall and R. Meyer, "A Survey of Hybrid Electric Propulsion for Aircraft," in *53rd AIAA/SAE/ASEE Joint Propulsion Conference*, p. 4700, 2017.
- [57] C. Friedrich and P. Robertson, "Hybrid-electric Propulsion for Automotive and Aviation Applications," *CEAS Aeronautical Journal*, vol. 6, pp. 279–290, 2015.
- [58] B. J. Brelje and J. R. Martins, "Electric, Hybrid, and Turboelectric Fixed-Wing Aircraft: A Review of Concepts, Models, and Design Approaches," *Progress in Aerospace Sciences*, vol. 104, pp. 1–19, 2019.
- [59] C. Pisanti, G. Rizzo, and V. Marano, "Energy Management of Through-the-Road Parallel Hybrid Vehicles," *IFAC Proceedings Volumes*, vol. 47, no. 3, pp. 2118–2124, 2014.
- [60] A. Panday and H. O. Bansal, "A Review of Optimal Energy Management Strategies for Hybrid Electric Vehicle," *International Journal of Vehicular Technology*, vol. 2014, pp. 1–19, 2014.
- [61] F. R. Salmasi, "Control Strategies for Hybrid Electric Vehicles: Evolution, Classification, Comparison, and Future Trends," *IEEE Transactions on Vehicular Technology*, vol. 56, no. 5, pp. 2393–2404, 2007.
- [62] A. Poursamad and M. Montazeri, "Design of Genetic-fuzzy Control Strategy for Parallel Hybrid Electric Vehicles," *Control Engineering Practice*, vol. 16, no. 7, pp. 861–873, 2008.
- [63] S. G. Li, S. M. Sharkh, F. C. Walsh, and C. N. Zhang, "Energy and Battery Management of a Plug-in Series Hybrid Electric Vehicle Using Fuzzy Logic," *IEEE Transactions on Vehicular Technology*, vol. 60, no. 8, pp. 3571–3585, 2011.
- [64] P. Pisu and G. Rizzoni, "A Comparative Study of Supervisory Control Strategies for Hybrid Electric Vehicles," *IEEE Transactions on Control Systems Technology*, vol. 15, no. 3, pp. 506–518, 2007.

- [65] J. Peng, H. He, and R. Xiong, “Rule Based Energy Management Strategy for a Series-parallel Plug-in Hybrid Electric Bus Optimized by Dynamic Programming,” *Applied Energy*, vol. 185, pp. 1633–1643, 2017.
- [66] E. D. Tate and S. P. Boyd, “Finding Ultimate Limits of Performance for Hybrid Electric Vehicles,” *SAE Transactions*, pp. 2437–2448, 2000.
- [67] R. Wang and S. M. Lukic, “Dynamic Programming Technique in Hybrid Electric Vehicle Optimization,” in *2012 IEEE International Electric Vehicle Conference*, pp. 1–8, 2012.
- [68] L. V. Pérez, G. R. Bossio, D. Moitre, and G. O. García, “Optimization of Power Management in an Hybrid Electric Vehicle Using Dynamic Programming,” *Mathematics and Computers in Simulation*, vol. 73, no. 1-4, pp. 244–254, 2006.
- [69] O. Sundström, L. Guzzella, and P. Soltic, “Optimal Hybridization in Two Parallel Hybrid Electric Vehicles Using Dynamic Programming,” *IFAC Proceedings Volumes*, vol. 41, no. 2, pp. 4642–4647, 2008.
- [70] S. Zhang and R. Xiong, “Adaptive Energy Management of a Plug-in Hybrid Electric Vehicle Based on Driving Pattern Recognition and Dynamic Programming,” *Applied Energy*, vol. 155, pp. 68–78, 2015.
- [71] Z. Yuan, L. Teng, S. Fengchun, and H. Peng, “Comparative Study of Dynamic Programming and Pontryagin’s Minimum Principle on Energy Management for a Parallel Hybrid Electric Vehicle,” *Energies*, vol. 6, no. 4, pp. 2305–2318, 2013.
- [72] N. Kim, S. Cha, and H. Peng, “Optimal Control of Hybrid Electric Vehicles Based on Pontryagin’s Minimum Principle,” *IEEE Transactions on Control Systems Technology*, vol. 19, no. 5, pp. 1279–1287, 2010.
- [73] C. C. Lin, H. Peng, and J. Grizzle, “A Stochastic Control Strategy for Hybrid Electric Vehicles,” in *Proceedings of the 2004 American Control Conference*, vol. 5, pp. 4710–4715, 2004.
- [74] X. Lü, Y. Wu, J. Lian, Y. Zhang, C. Chen, P. Wang, and L. Meng, “Energy Management of Hybrid Electric Vehicles: A Review of Energy Optimization of Fuel Cell Hybrid Power System Based on Genetic Algorithm,” *Energy Conversion and Management*, vol. 205, p. 112474, 2020.
- [75] M. Montazeri-Gh, A. Poursamad, and B. Ghalichi, “Application of Genetic Algorithm for Optimization of Control Strategy in Parallel Hybrid Electric Vehicles,” *Journal of the Franklin Institute*, vol. 343, no. 4-5, pp. 420–435, 2006.
- [76] A. Piccolo, L. Ippolito, V. Zo Galdi, and A. Vaccaro, “Optimisation of Energy Flow Management in Hybrid Electric Vehicles via Genetic Algorithms,” in *2001 IEEE/ASME International Conference on Advanced Intelligent Mechatronics. Proceedings (Cat. No. 01TH8556)*, vol. 1, pp. 434–439, 2001.

- [77] N. Kim, S. W. Cha, and H. Peng, “Optimal Equivalent Fuel Consumption for Hybrid Electric Vehicles,” *IEEE Transactions on Control Systems Technology*, vol. 20, no. 3, pp. 817–825, 2011.
- [78] J. Gao, G. G. Zhu, E. G. Strangas, and F. Sun, “Equivalent Fuel Consumption Optimal Control of a Series Hybrid Electric Vehicle,” *Proceedings of the Institution of Mechanical Engineers, Part D: Journal of Automobile Engineering*, vol. 223, no. 8, pp. 1003–1018, 2009.
- [79] F. Yan, J. Wang, and K. Huang, “Hybrid Electric Vehicle Model Predictive Control Torque-split Strategy Incorporating Engine Transient Characteristics,” *IEEE Transactions on Vehicular Technology*, vol. 61, no. 6, pp. 2458–2467, 2012.
- [80] G. Ripaccioli, D. Bernardini, S. Di Cairano, A. Bemporad, and I. Kolmanovsky, “A Stochastic Model Predictive Control Approach for Series Hybrid Electric Vehicle Power Management,” in *Proceedings of the 2010 American Control Conference*, pp. 5844–5849, 2010.
- [81] S. Zhang, R. Xiong, and F. Sun, “Model Predictive Control for Power Management in a Plug-in Hybrid Electric Vehicle with a Hybrid Energy Storage System,” *Applied Energy*, vol. 185, pp. 1654–1662, 2017.
- [82] X. Qi, G. Wu, K. Boriboonsomsin, and M. J. Barth, “A Novel Blended Real-time Energy Management Strategy for Plug-in Hybrid Electric Vehicle Commute Trips,” in *2015 IEEE 18th International Conference on Intelligent Transportation Systems*, pp. 1002–1007, 2015.
- [83] X. Lin, Y. Wang, P. Bogdan, N. Chang, and M. Pedram, “Reinforcement Learning Based Power Management for Hybrid Electric Vehicles,” in *2014 IEEE/ACM International Conference on Computer-aided Design (ICCAD)*, pp. 33–38, 2014.
- [84] C. Song, H. Lee, K. Kim, and S. W. Cha, “A Power Management Strategy for Parallel PHEV Using Deep Q-networks,” in *2018 IEEE Vehicle Power and Propulsion Conference (VPPC)*, pp. 1–5, 2018.
- [85] C. Dextreit and I. V. Kolmanovsky, “Game Theory Controller for Hybrid Electric Vehicles,” *IEEE Transactions on Control Systems Technology*, vol. 22, no. 2, pp. 652–663, 2013.
- [86] C. Hou, M. Ouyang, L. Xu, and H. Wang, “Approximate Pontryagin’s Minimum Principle Applied to the Energy Management of Plug-in Hybrid Electric Vehicles,” *Applied Energy*, vol. 115, pp. 174–189, 2014.
- [87] J. P. S. Pinto Leite and M. Voskuijl, “Optimal Energy Management for Hybrid-electric Aircraft,” *Aircraft Engineering and Aerospace Technology*, vol. 92, no. 6, pp. 851–861, 2020.
- [88] M. Doff-Sotta, M. Cannon, and M. Bacic, “Optimal Energy Management for Hybrid Electric Aircraft,” *IFAC-PapersOnLine*, vol. 53, no. 2, pp. 6043–6049, 2020.

- [89] J. Zhang, I. Roumeliotis, and A. Zolotas, “Nonlinear Model Predictive Control-based Optimal Energy Management for Hybrid Electric Aircraft Considering Aerodynamics-propulsion Coupling Effects,” *IEEE Transactions on Transportation Electrification*, vol. 8, no. 2, pp. 2640–2653, 2021.
- [90] S. Li, C. Gu, P. Zhao, and S. Cheng, “A Novel Hybrid Propulsion System Configuration and Power Distribution Strategy for Light Electric Aircraft,” *Energy Conversion and Management*, vol. 238, p. 114171, 2021.
- [91] T. Donateo, A. Ficarella, and L. Spedicato, “Applying Dynamic Programming Algorithms to the Energy Management of Hybrid Electric Aircraft,” in *Turbo Expo: Power for Land, Sea, and Air*, vol. 51043, p. V003T06A015, 2018.
- [92] T. Donateo, C. L. De Pascalis, L. Strafella, and A. Ficarella, “Off-line and On-line Optimization of the Energy Management Strategy in a Hybrid Electric Helicopter for Urban Air-Mobility,” *Aerospace Science and Technology*, vol. 113, p. 106677, 2021.
- [93] T. J. Wall and R. Meyer, “A Survey of Hybrid Electric Propulsion for Aircraft,” in *53rd AIAA/SAE/ASEE Joint Propulsion Conference*, 2017.
- [94] J. Zamboni, R. Vos, M. Emeneth, and A. Schneegans, “A Method for the Conceptual Design of Hybrid Electric Aircraft,” in *AIAA Scitech 2019 Forum*, (San Diego, California), AIAA, Jan. 2019.
- [95] D. F. Finger, C. Braun, and C. Bil, “Comparative Assessment of Parallel-hybrid-electric Propulsion Systems for Four Different Aircraft,” *Journal of Aircraft*, vol. 57, no. 5, pp. 843–853, 2020.
- [96] D. F. Finger, C. Bil, and C. Braun, “Initial Sizing Methodology for Hybrid-electric General Aviation Aircraft,” *Journal of Aircraft*, vol. 57, no. 2, pp. 245–255, 2020.
- [97] R. De Vries, M. Brown, and R. Vos, “Preliminary Sizing Method for Hybrid-electric Distributed-propulsion Aircraft,” *Journal of Aircraft*, vol. 56, no. 6, pp. 2172–2188, 2019.
- [98] C. Pornet and A. Isikveren, “Conceptual Design of Hybrid-electric Transport Aircraft,” *Progress in Aerospace Sciences*, vol. 79, pp. 114–135, 2015.
- [99] R. Ravishankar and S. R. Chakravarthy, “Range Equation for a Series Hybrid Electric Aircraft,” in *2018 Aviation Technology, Integration, and Operations Conference*, p. 3208, 2018.
- [100] A. T. Isikveren, S. Kaiser, C. Pornet, and P. C. Vratny, “Pre-design Strategies and Sizing Techniques for Dual-energy Aircraft,” *Aircraft Engineering and Aerospace Technology: An International Journal*, vol. 86, no. 6, pp. 525–542, 2014.

- [101] R. F. Hartl, S. P. Sethi, and R. G. Vickson, “A Survey of the Maximum Principles for Optimal Control Problems with State Constraints,” *SIAM Review*, vol. 37, pp. 181–218, June 1995.
- [102] H. Maurer, “On Optimal Control Problems with Bounded State Variables and Control Appearing Linearly,” *SIAM Journal on Control and Optimization*, vol. 15, no. 3, pp. 345–362, 1977.
- [103] C. Y. Kaya and J. L. Noakes, “Computational Method for Time-optimal Switching Control,” *Journal of Optimization Theory and Applications*, vol. 117, pp. 69–92, 2003.
- [104] J. A. Andersson, J. Gillis, G. Horn, J. B. Rawlings, and M. Diehl, “Casadi: a Software Framework for Nonlinear Optimization and Optimal Control,” *Mathematical Programming Computation*, vol. 11, pp. 1–36, 2019.
- [105] J.-H. R. Kim and H. Maurer, “Sensitivity Analysis of Optimal Control Problems with Bang-bang Controls,” in *42nd IEEE International Conference on Decision and Control (IEEE Cat. No. 03CH37475)*, vol. 4, pp. 3281–3286, 2003.
- [106] H. Yang and M. G. H. Bell, “Models and Algorithms for Road Network Design: a Review and Some New Developments,” *Transport Reviews*, vol. 18, no. 3, pp. 257–278, 1998.
- [107] A. Migdalas, “Bilevel Programming in Traffic Planning: Models, Methods and Challenge,” *Journal of Global Optimization*, vol. 7, no. 4, pp. 381–405, 1995.
- [108] R. Z. Farahani, E. Miandoabchi, W. Y. Szeto, and H. Rashidi, “A Review of Urban Transportation Network Design Problems,” *European Journal of Operational Research*, vol. 229, no. 2, pp. 281–302, 2013.
- [109] M. Patriksson, *The Traffic Assignment Problem: Models and Methods*. Courier Dover Publications, 2015.
- [110] M. Beckmann, C. B. McGuire, and C. B. Winsten, “Studies in the Economics of Transportation,” 1956.
- [111] Y. Nesterov, “Stable Traffic Equilibria: Properties and Applications,” *Optimization and Engineering*, vol. 1, no. 1, pp. 29–50, 2000.
- [112] Y. Nesterov and A. de Palma, “Stationary Dynamic Solutions in Congested Transportation Networks: Summary and Perspectives,” *Networks and Spatial Economics*, vol. 3, no. 3, pp. 371–395, 2003.
- [113] F. A. Chudak, V. Dos Santos Eleuterio, and Y. Nesterov, “Static Traffic Assignment Problem: A Comparison Between Beckmann (1956) and Nesterov & de Palma (1998) models,” in *7th Swiss Transport Research Conference*, 2007.

- [114] W. Wei, L. Wu, J. Wang, and S. Mei, “Expansion Planning of Urban Electrified Transportation Networks: A Mixed-integer Convex Programming Approach,” *IEEE Transactions on Transportation Electrification*, vol. 3, no. 1, pp. 210–224, 2017.
- [115] X. Wang, M. Shahidehpour, C. Jiang, and Z. Li, “Coordinated Planning Strategy for Electric Vehicle Charging Stations and Coupled Traffic-electric Networks,” *IEEE Transactions on Power Systems*, vol. 34, no. 1, pp. 268–279, 2018.
- [116] F. Xia, H. Chen, M. Shahidehpour, W. Gan, M. Yan, and L. Chen, “Distributed Expansion Planning of Electric Vehicle Dynamic Wireless Charging System in Coupled Power-traffic Networks,” *IEEE Transactions on Smart Grid*, 2021.
- [117] M. Patriksson and R. T. Rockafellar, “A Mathematical Model and Descent Algorithm for Bilevel Traffic Management,” *Transportation Science*, vol. 36, no. 3, pp. 271–291, 2002.
- [118] D. Hearn, “Bounding Flows in Traffic Assignment Models,” *Res. Rep.*, pp. 80–4, 1980.
- [119] T. Larsson and M. Patriksson, “Side Constrained Traffic Equilibrium Models—analysis, Computation and Applications,” *Transportation Research Part B: Methodological*, vol. 33, no. 4, pp. 233–264, 1999.
- [120] D. Bertsekas, *Network Optimization: Continuous and Discrete Models*, vol. 8. Athena Scientific, 1998.
- [121] A. Ben-Tal and A. Nemirovski, *Lectures on Modern Convex Optimization: Analysis, Algorithms, and Engineering Applications*. SIAM, 2001.
- [122] J. G. Wardrop, “Some Theoretical Aspects of Road Traffic Research,” *Proceedings of the institution of civil engineers*, vol. 1, no. 3, pp. 325–362, 1952.
- [123] J. F. Bard, *Practical Bilevel Optimization: Algorithms and Applications*, vol. 30. Springer Science & Business Media, 2013.
- [124] Gurobi Optimization, LLC, “Gurobi Optimizer Reference Manual,” 2021.
- [125] E. Klotz and A. M. Newman, “Practical Guidelines for Solving Difficult Mixed Integer Linear Programs,” *Surveys in Operations Research and Management Science*, vol. 18, no. 1-2, pp. 18–32, 2013.
- [126] Transportation Networks for Research Core Team, “Transportation Networks for Research.” <https://github.com/bstabler/TransportationNetworks>, 2016. Accessed: 2022-01-01.
- [127] A. Khamis, A. Hussein, and A. Elmogy, “Multi-robot Task Allocation: A Review of the State-of-the-Art,” *Cooperative Robots and Sensor Networks*, pp. 31–51, 2015.

- [128] G. A. Korsah, A. Stentz, and M. B. Dias, “A Comprehensive Taxonomy for Multi-robot Task Allocation,” *The International Journal of Robotics Research*, vol. 32, no. 12, pp. 1495–1512, 2013.
- [129] C. A. Floudas and X. Lin, “Mixed Integer Linear Programming in Process Scheduling: Modeling, Algorithms, and Applications,” *Annals of Operations Research*, vol. 139, pp. 131–162, 2005.
- [130] C. Schumacher, P. Chandler, M. Pachter, and L. Pachter, “UAV Task Assignment with Timing Constraints via Mixed-integer Linear Programming,” in *AIAA 3rd “Unmanned Unlimited” Technical Conference, Workshop and Exhibit*, p. 6410, 2004.
- [131] S. Chopra, G. Notarstefano, M. Rice, and M. Egerstedt, “A Distributed Version of the Hungarian Method for Multirobot Assignment,” *IEEE Transactions on Robotics*, vol. 33, no. 4, pp. 932–947, 2017.
- [132] S. Ismail and L. Sun, “Decentralized Hungarian-based Approach for Fast and Scalable Task Allocation,” in *2017 International Conference on Unmanned Aircraft Systems (ICUAS)*, pp. 23–28, 2017.
- [133] G. Qu, D. Brown, and N. Li, “Distributed Greedy Algorithm for Multi-agent Task Assignment Problem with Submodular Utility Functions,” *Automatica*, vol. 105, pp. 206–215, 2019.
- [134] H. L. Choi, L. Brunet, and J. P. How, “Consensus-based Decentralized Auctions for Robust Task Allocation,” *IEEE Transactions on Robotics*, vol. 25, no. 4, pp. 912–926, 2009.
- [135] M. M. Zavlanos, L. Spesivtsev, and G. J. Pappas, “A Distributed Auction Algorithm for the Assignment Problem,” in *2008 47th IEEE Conference on Decision and Control*, pp. 1212–1217, 2008.
- [136] G. Arslan, J. R. Marden, and J. S. Shamma, “Autonomous Vehicle-target Assignment: A Game-theoretical Formulation,” 2007.
- [137] P. Vansteenwegen, W. Souffriau, and D. Van Oudheusden, “The Orienteering Problem: A Survey,” *European Journal of Operational Research*, vol. 209, no. 1, pp. 1–10, 2011.
- [138] M. Fischetti, J. J. S. Gonzalez, and P. Toth, “Solving the Orienteering Problem Through Branch-and-cut,” *INFORMS Journal on Computing*, vol. 10, no. 2, pp. 133–148, 1998.
- [139] D. Feillet, P. Dejax, and M. Gendreau, “Traveling Salesman Problems with Profits,” *Transportation Science*, vol. 39, no. 2, pp. 188–205, 2005.
- [140] G. Righini and M. Salani, “New Dynamic Programming Algorithms for the Resource Constrained Elementary Shortest Path Problem,” *Networks: An International Journal*, vol. 51, no. 3, pp. 155–170, 2008.

- [141] D. Feillet, P. Dejax, M. Gendreau, and C. Gueguen, “An Exact Algorithm for the Elementary Shortest Path Problem with Resource Constraints: Application to Some Vehicle Routing Problems,” *Networks: An International Journal*, vol. 44, no. 3, pp. 216–229, 2004.
- [142] R. Montemanni, D. Weyland, and L. Gambardella, “An Enhanced Ant Colony System for the Team Orienteering Problem with Time Windows,” in *2011 International Symposium on Computer Science and Society*, pp. 381–384, 2011.
- [143] L. Ke, C. Archetti, and Z. Feng, “Ants Can Solve the Team Orienteering Problem,” *Computers & Industrial Engineering*, vol. 54, no. 3, pp. 648–665, 2008.
- [144] H. Tang and E. Miller-Hooks, “A Tabu Search Heuristic for the Team Orienteering Problem,” *Computers & Operations Research*, vol. 32, no. 6, pp. 1379–1407, 2005.
- [145] C. Archetti, A. Hertz, and M. G. Speranza, “Metaheuristics for the Team Orienteering Problem,” *Journal of Heuristics*, vol. 13, pp. 49–76, 2007.
- [146] P. Vansteenwegen, W. Souffriau, G. V. Berghe, and D. Van Oudheusden, “A Guided Local Search Metaheuristic for the Team Orienteering Problem,” *European Journal of Operational Research*, vol. 196, no. 1, pp. 118–127, 2009.
- [147] M. Desrochers, *An Algorithm for the Shortest Path Problem with Resource Constraints*. École des hautes études commerciales, Groupe d'études et de recherche en analyse des décisions, 1988.
- [148] G. L. Nemhauser, L. A. Wolsey, and M. L. Fisher, “An Analysis of Approximations for Maximizing Submodular Set Functions—I,” *Mathematical programming*, vol. 14, pp. 265–294, 1978.
- [149] M. L. Fisher, G. L. Nemhauser, and L. A. Wolsey, *An Analysis of Approximations for Maximizing Submodular Set Functions—II*. Springer, 1978.
- [150] S. Fujishige, *Submodular Functions and Optimization*. Elsevier, 2005.
- [151] A. Krause and D. Golovin, “Submodular Function Maximization,” *Tractability*, vol. 3, no. 71–104, p. 3, 2014.
- [152] W. Xu, Z. Xu, J. Peng, W. Liang, T. Liu, X. Jia, and S. K. Das, “Approximation Algorithms for the Team Orienteering Problem,” in *IEEE INFOCOM 2020-IEEE Conference on Computer Communications*, pp. 1389–1398, 2020.
- [153] W. Xu, W. Liang, Z. Xu, J. Peng, D. Peng, T. Liu, X. Jia, and S. K. Das, “Approximation Algorithms for the Generalized Team Orienteering Problem and Its Applications,” *IEEE/ACM Transactions on Networking*, vol. 29, no. 1, pp. 176–189, 2020.

- [154] N. Boland, J. Dethridge, and I. Dumitrescu, “Accelerated Label Setting Algorithms for the Elementary Resource Constrained Shortest Path Problem,” *Operations Research Letters*, vol. 34, no. 1, pp. 58–68, 2006.
- [155] H. Maurer, I. Altrogge, and N. Goris, “Optimization Methods for Solving Bang-bang Control Problems with State Constraints and the Verification of Sufficient Conditions,” in *Proceedings of the 44th IEEE Conference on Decision and Control*, pp. 923–928, IEEE, 2005.

## Appendix A

### HEA OPTIMIZATION PROBLEM TRANSFORMATION

This chapter provides a detailed presentation of the analytical steps implemented in Section 4.3.

#### A.1 Transformation to a finite-dimensional optimization problem

In Problem 6, the explicit functions of the optimal control on each arc are as follows:

1. On  $\hat{t} \in [0, \hat{t}_1]$ , the optimal control is  $\tau^* = \tau_{\max} = 1$ . Hence, the dynamics of states can be written as,

$$\dot{\hat{m}} = k_{11} + k_{10}, \quad (\text{A.1a})$$

$$\dot{\hat{q}} = k_{21} + k_{20} + k_{22}\hat{m}^2 + k_{23}\hat{m}, \quad (\text{A.1b})$$

resulting in the explicit expressions for states as a function of time,

$$\hat{m}(\hat{t}) = m_0 + (k_{11} + k_{10})\hat{t}, \quad (\text{A.2a})$$

$$\hat{q}(\hat{t}) = h_{13}\hat{t}^3 + h_{12}\hat{t}^2 + h_{11}\hat{t} + h_{10}, \quad (\text{A.2b})$$

where,  $h_{13} = \frac{1}{3}k_{22}(k_{11} + k_{10})^2$ ,  $h_{12} = (k_{22}m_0 + \frac{1}{2}k_{23})(k_{11} + k_{10})$ ,  $h_{11} = k_{21} + k_{20} + k_{22}m_0^2 + k_{23}m_0$ , and  $h_{10} = \hat{q}_0$  is computed from  $\hat{q}(\hat{t} = 0) = \hat{q}_0$ .

2. On  $\hat{t} \in [\hat{t}_1, \hat{t}_2]$ ,  $\hat{q}(\hat{t}) = 0$  holds for all  $\hat{t}$ , and the optimal control is  $\tau_b = -\frac{1}{k_{21}}(k_{20} + k_{22}\hat{m}^2 + k_{23}\hat{m})$ . Hence, the dynamics of the aircraft mass can be written as,

$$\dot{\hat{m}} = -\frac{k_{11}}{k_{21}}(k_{20} + k_{22}\hat{m}^2 + k_{23}\hat{m}) + k_{10}. \quad (\text{A.3})$$

The initial condition for this interval is  $\hat{m}(\hat{t}_1) = m_0 + (k_{11} + k_{10})\hat{t}_1$ . Thereby, by separation

of variables, we obtain the explicit function of the aircraft's mass on the boundary arc as,

$$\hat{m}(\hat{t}) = \frac{1}{2k_{32}}[r_0 \tan\left(-\frac{r_0(\hat{t} - \hat{t}_1)}{2} + C_0\right) - k_{31}], \quad (\text{A.4})$$

where  $k_{30} = \frac{k_{11}k_{20}}{k_{21}} - k_{10}$ ,  $k_{31} = \frac{k_{11}k_{23}}{k_{21}}$ ,  $k_{32} = \frac{k_{11}k_{22}}{k_{21}}$ , and

$$C_0 = \frac{-2 \arctan\left(\frac{2k_{32}m(\hat{t}_1) + k_{31}}{r_0}\right)}{r_0}, \quad r_0 = \sqrt{4k_{32}k_{30} - k_{31}^2}.$$

We denote  $\hat{m}(\hat{t}_2)$  as  $z$ , which is the third constraint in Problem 7.

3. On  $\hat{t} \in [\hat{t}_2, 1]$ , the optimal control is  $\tau^* = \tau_{min} = 0$ ; thus, the dynamics of states can be written as

$$\dot{\hat{m}} = k_{10}, \quad (\text{A.5a})$$

$$\dot{\hat{q}} = k_{20} + k_{22}\hat{m}^2 + k_{23}\hat{m}, \quad (\text{A.5b})$$

where the initial states on this arc are  $[z, 1]^\top$ ; the explicit functions of the states are,

$$\hat{m}(\hat{t}) = \hat{m}(\hat{t}_2) + k_{10}(\hat{t} - \hat{t}_2), \quad (\text{A.6a})$$

$$\begin{aligned} \hat{q}(\hat{t}) &= g_{13}(\hat{t} - \hat{t}_2)^3 + g_{12}z(\hat{t} - \hat{t}_2)^2 + g_{11}(\hat{t} - \hat{t}_2)^2 \\ &\quad + k_{20}(\hat{t} - \hat{t}_2) + k_{22}z^2(\hat{t} - \hat{t}_2) + k_{23}z(\hat{t} - \hat{t}_2) + 1, \end{aligned} \quad (\text{A.6b})$$

where  $g_{13} = \frac{1}{3}k_{22}k_{10}^2$ ,  $g_{12} = k_{22}k_{10}$ , and  $g_{11} = \frac{1}{2}k_{23}k_{10}$ .

The first constraint for Problem 7 is when  $q$  hits the boundary at the junction time  $\hat{t} = \hat{t}_1$ , given as

$$\Phi_1 := \hat{q}(\hat{t}_1) = 1. \quad (\text{A.7})$$

When we substitute this constraint into Eq. (A.2b), we obtain,

$$h_{13}\xi_1^3 + h_{12}\xi_1^2 + h_{11}\xi_1 + h_{10} = 1. \quad (\text{A.8})$$

The second constraint for the optimization problem is the terminal condition for  $\hat{q}$ , i.e.,  $\hat{q}(1) = \hat{q}_f$ ; after substituting this constraint into Eq. (A.6b), we obtain

$$g_{13}\xi_3^3 + g_{12}z\xi_3^2 + g_{11}\xi_3^2 + k_{20}\xi_3 + k_{22}z^2\xi_3 + k_{23}z\xi_3 + 1 - \hat{q}_f = 0. \quad (\text{A.9})$$

## A.2 Verification of the second-order sufficient condition and sensitivity analysis

We refer to Theorem 3.1 in [155] pertaining to the second-order sufficient condition for Problem 7. Let  $\mathbf{x}$  be a feasible solution of Problem 7. Suppose the following conditions hold:

1.  $L_{\mathbf{x}} = 0$  (first order necessary condition).
2.  $\text{rank}[\Phi_{\mathbf{x}}] = r$ , where  $r$  is the number of constraints.
3.  $v^\top L_{\mathbf{x}\mathbf{x}}v > 0, \forall v \in \mathbb{R}^n, v \neq 0. \Phi_{\mathbf{x}}v = 0$ , where  $n$  is the number of variables in Problem 6.

Then  $\mathbf{x}$  is a strict minimizer of Problem 7.

Let  $\Delta = 1 + \tan(\frac{r_0}{2}\xi_2)(f_1x_{10} + f_2\xi_1 + f_3)$  and  $f_4 = f_1x_{10} + f_2\xi_1 + f_3$ .

The expression for  $L_{\mathbf{x}}$  are now computed as,

$$L_{\xi_1} = \rho_1(3h_{13}\xi_1^2 + 2h_{12}\xi_1 + h_{11}) + \rho_4 + \frac{-\rho_3 f_2}{f_1} \frac{(1 + \tan^2(\frac{r_0}{2}\xi_2))}{\Delta^2}, \quad (\text{A.10a})$$

$$L_{\xi_2} = \frac{\rho_3 r_0}{2f_1} \frac{(1 + f_4^2) \sec^2(\frac{r_0}{2}\xi_2)}{\Delta^2} + \rho_4, \quad (\text{A.10b})$$

$$L_{\xi_3} = -k_{10} + \rho_4 + \rho_2(3g_{13}\xi_3^2 + 2g_{12}z\xi_3 + 2g_{11}\xi_3 + k_{20} + k_{22}z^2 + k_{23}z), \quad (\text{A.10c})$$

$$L_z = -1 + \rho_3 + \rho_2(g_{12}\xi_3^2 + 2k_{22}\xi_3z + k_{23}\xi_3). \quad (\text{A.10d})$$

The matrix  $L_{\mathbf{x}\mathbf{x}}$  is now represented as,

$$L_{\mathbf{x}\mathbf{x}} = \begin{bmatrix} \frac{\partial L_{\xi_1}}{\partial \xi_1} & \frac{\partial L_{\xi_1}}{\partial \xi_2} & \frac{\partial L_{\xi_1}}{\partial \xi_3} & \frac{\partial L_{\xi_1}}{\partial z} \\ \frac{\partial L_{\xi_2}}{\partial \xi_1} & \frac{\partial L_{\xi_2}}{\partial \xi_2} & \frac{\partial L_{\xi_2}}{\partial \xi_3} & \frac{\partial L_{\xi_2}}{\partial z} \\ \frac{\partial L_{\xi_3}}{\partial \xi_1} & \frac{\partial L_{\xi_3}}{\partial \xi_2} & \frac{\partial L_{\xi_3}}{\partial \xi_3} & \frac{\partial L_{\xi_3}}{\partial z} \\ \frac{\partial L_z}{\partial \xi_1} & \frac{\partial L_z}{\partial \xi_2} & \frac{\partial L_z}{\partial \xi_3} & \frac{\partial L_z}{\partial z} \end{bmatrix} = \begin{bmatrix} L_{11} & L_{12} & 0 & 0 \\ L_{21} & L_{22} & 0 & 0 \\ 0 & 0 & L_{33} & L_{34} \\ 0 & 0 & L_{43} & L_{44} \end{bmatrix}, \quad (\text{A.11})$$

where

$$L_{11} = \rho_1(6h_{13}\xi_1 + 2h_{12}) + \frac{2\rho_3 f_2^2}{f_1} \frac{(\tan(\frac{r_0}{2}\xi_2) + \tan^3(\frac{r_0}{2}\xi_2))}{\Delta^3}, \quad (\text{A.12a})$$

$$L_{12} = \frac{-\rho_3 r_0 f_2}{f_1} \frac{\sec^2(\frac{r_0}{2}\xi_2)(\tan(\frac{r_0}{2}\xi_2) - f_4)}{\Delta^3}, \quad (\text{A.12b})$$

$$L_{21} = L_{12}, \quad (\text{A.12c})$$

$$L_{22} = \frac{\rho_3 r_0^2 (1 + f_4^2) \sec^2(\frac{r_0}{2}\xi_2)}{2f_1} \frac{(\tan(\frac{r_0}{2}\xi_2)(f_4 \tan(\frac{r_0}{2}\xi_2) + 1) - f_4 \sec^2(\frac{r_0}{2}\xi_2))}{\Delta^3}. \quad (\text{A.12d})$$

Lastly, the function  $\Phi_x$  is computed as,

$$\begin{aligned} \frac{\partial \Phi_1}{\partial \xi_1} &= 3h_{13}\xi_1^2 + 2h_{12}\xi_1 + h_{11}, & \frac{\partial \Phi_1}{\partial \xi_2} &= 0, \\ \frac{\partial \Phi_1}{\partial \xi_3} &= 0, & \frac{\partial \Phi_1}{\partial z} &= 0; \end{aligned} \quad (\text{A.13a})$$

$$\frac{\partial \Phi_2}{\partial \xi_1} = 0, \quad \frac{\partial \Phi_2}{\partial \xi_2} = 0,$$

$$\frac{\partial \Phi_2}{\partial \xi_3} = 3g_{13}\xi_3^2 + 2g_{12}z\xi_3 + 2g_{11}\xi_3 + k_{20} + k_{22}z^2 + k_{23}z,$$

$$\frac{\partial \Phi_2}{\partial z} = g_{12}\xi_3^2 + 2k_{22}\xi_3z + k_{23}\xi_3; \quad (\text{A.13b})$$

$$\frac{\partial \Phi_3}{\partial \xi_1} = \frac{-f_2(1 + \tan^2(\frac{r_0}{2}\xi_2))}{f_1\Delta^2}, \quad \frac{\partial \Phi_3}{\partial \xi_2} = \frac{r_0 \sec^2(\frac{r_0}{2}\xi_2)(1 + f_4^2)}{2f_1\Delta^2},$$

$$\frac{\partial \Phi_3}{\partial \xi_3} = 0, \quad \frac{\partial \Phi_3}{\partial z} = 1; \quad (\text{A.13c})$$

$$\frac{\partial \Phi_4}{\partial \xi_1} = 1, \quad \frac{\partial \Phi_4}{\partial \xi_2} = 1, \quad \frac{\partial \Phi_4}{\partial \xi_3} = 1, \quad \frac{\partial \Phi_4}{\partial z} = 0. \quad (\text{A.13d})$$

With  $L_x$ ,  $L_{xx}$ , and  $\Phi_x$ , one can easily verify the second order sufficient condition, and conduct sensitivity analyses.

## Appendix B

### VERTIPORT SELECTION PROOF

#### B.1 Proof of Proposition 1

We start by deriving the dual of the linear program 5.8. Let the *Lagrangian* be defined as

$$\begin{aligned} L(X, U, V, p, q) &= c^\top X \mathbf{1}_d - \text{tr}(V^\top EX) + \text{tr}(V^\top S) \\ &\quad - \text{tr}(U^\top X) + p^\top (X \mathbf{1}_d - f) + q^\top (DX \mathbf{1}_d - g). \end{aligned} \tag{B.1}$$

The dual of the linear program is given by

$$\begin{aligned} &\underset{U, V, p, q}{\text{maximize}} \quad \psi(U, V, p, q) \\ &\text{subject to} \quad U \geq 0, \quad p \geq 0, \quad q \geq 0. \end{aligned} \tag{B.2}$$

where  $\psi(U, V, p, q) = \min_X L(X, U, V, p, q)$ . Since matrix trace is invariant under cyclic permutation, we have

$$c^\top X \mathbf{1}_d = \text{tr}(\mathbf{1}_d c^\top X), \quad p^\top X \mathbf{1}_d = \text{tr}(\mathbf{1}_d p^\top X), \quad q^\top DX \mathbf{1}_d = \text{tr}(\mathbf{1}_d q^\top DX).$$

Substitute the above equalities into Eq.(B.1), we can show the following

$$\begin{aligned} \frac{\partial}{\partial X} L(X, U, V, p, q) &= \frac{\partial}{\partial X} \text{tr}((\mathbf{1}_d(c^\top + p^\top + q^\top D) - V^\top E - U^\top)X) \\ &= (c + p + D^\top q)\mathbf{1}_d - E^\top V - U. \end{aligned}$$

Since  $L(X, U, V, p, q)$  is a linear function of  $X$ , we have  $\psi(U, V, p, q) = L(X, U, V, p, q)$  if and only if  $\frac{\partial}{\partial X} L(X, U, V, p, q) = 0$ . Therefore, we can rewrite optimization Eq.(B.2) equivalently as follows

$$\begin{aligned} &\underset{U, V, p, q}{\text{maximize}} \quad \text{tr}(V^\top S) - f^\top p - g^\top q \\ &\text{subject to} \quad (c + p + D^\top q)\mathbf{1}_d^\top = E^\top V + U, \\ &\quad U \geq 0, \quad p \geq 0, \quad q \geq 0. \end{aligned} \tag{B.3}$$

Using [121, Thm. 1.3.3], we conclude that  $X$  and  $U, V, p, q$  are optimal for linear program 5.8 and Eq.(B.3), respectively, if and only if the primal and dual feasibility condition in Eq.(5.9) and the complementary slackness condition Eq.(5.10) are satisfied. Furthermore, the complementary slackness conditions in Eq.(5.10) are equivalent to the zero duality gap condition in Eq.(5.11).

## B.2 Proof of Corollary 1

Since  $u^*, u \in \mathcal{P}(i, s(j))$ , by pre-multiplying equation Eq.(5.9) with  $u^*$  and  $u$  and we can show the following:

$$(u^*)^\top \bar{c} = V_{ij} - V_{s(j),j} + \sum_{k=1}^{n_l} [u^*]_j [U]_{kj}, \quad (\text{B.4a})$$

$$u^\top \bar{c} = V_{ij} - V_{s(j),j} + \sum_{k=1}^{n_l} [u]_j [U]_{kj}. \quad (\text{B.4b})$$

In addition, the constraints in Eq.(5.9c) and Eq.(5.10) together implies that  $[U]_{kj} = 0$  for all  $k$  such that  $[X]_{kj} > 0$ . Combining this fact with the assumption that  $[X]_{kj} > 0$  for all  $k$  such that  $[u^*]_k = 1$ , we conclude that  $[U]_{kj} = 0$  for all  $k$  such that  $[u^*]_k = 1$ . Hence

$$(u^*)^\top \bar{c} = V_{ij} - V_{s(j),j} + \sum_{k=1}^{n_l} [u^*]_j [U]_{kj} = V_{ij} - V_{s(j),j}. \quad (\text{B.5})$$

By combining Eq.(B.4) and Eq.(B.5), we obtain the following

$$(u^*)^\top \bar{c} = V_{ij} - V_{s(j),j} = u^\top \bar{c} - \sum_{k=1}^{n_l} [u]_j [U]_{kj} \leq u^\top \bar{c},$$

where the last step is because  $u$  and  $U$  are both elementwise nonnegative.

## B.3 Proof of Proposition 2

First, suppose  $\delta, q, B$ , and  $g$  satisfy the constraints in Eq.(5.21). Let  $[Y]_{ij} = [g]_i [q]_i [B]_{ij}$  for all  $i = 1, 2, \dots, n_v$  and  $j = 1, 2, \dots, n_m$ , and  $\mu = \max_{i,j} [q]_i [G]_{ij}$ . Then one can verify that  $\delta, q, B$ , and  $Y$  satisfy the constraints in Eq.(5.22).

Second, suppose  $\delta, q, B$  and  $Y$  satisfy the constraints in Eq.(5.22) for some sufficiently large  $\mu \in \mathbb{R}_{++}$ . The constraints  $B \in \{0, 1\}^{n_v \times n_m}$  and  $B\mathbf{1}_{n_m} \leq \mathbf{1}_{n_v}$  implies that each row of matrix  $B$  can have at most one entry equals one. Hence, we can obtain a unique vector  $g$  by defining its  $i$ -th

entry as follows:

$$[g]_i = \begin{cases} [G]_{ij}, & \text{if } [B]_{ij} = 1, \\ 0, & \text{if } [B]_{ij} = 0 \text{ for all } j = 1, 2, \dots, n_m. \end{cases} \quad (\text{B.6})$$

Next, since  $\mu \in \mathbb{R}_{++}$  is sufficiently large, an upper bound of  $\mu$  can be treated as redundant. As a result, if  $[B]_{ij} = 0$ , then the constraints in Eq.(5.22) implies that  $[Y]_{ij} = 0$  and  $[G]_{ij}[q]_i \geq 0$ . Since  $q \geq 0$  and  $G \geq 0$ , the latter constraint is redundant. Furthermore, if  $[B]_{ij} = 1$ , then the constraints in Eq.(5.22) implies that

$$0 \leq [Y]_{ij}, \quad [G]_{ij}[q]_i = [Y]_{ij}.$$

By combining the above two cases with the definition in Eq.(B.6), we conclude that  $\sum_{i=1}^{n_v} \sum_{j=1}^{n_m} [Y]_{ij} = \sum_{i=1}^{n_v} [g]_i [q]_i$  for all  $i = 1, 2, \dots, n_v$  and  $j = 1, 2, \dots, n_m$ . Therefore,  $\delta, q, B$  and  $g$  satisfy the constraints in Eq.(5.21).